OPTICAL RESPONSE OF UNDOPED AND DOPED ZINC OXIDE THIN FILMS

By

TRES ALLAN HARRIMAN

Bachelor of Science in Mechanical Engineering
University of Missouri - Columbia
Columbia, Missouri
2003

Master of Science in Mechanical Engineering
Oklahoma State University
Stillwater, Oklahoma
2008

Submitted to the Faculty of the
Graduate College of the
Oklahoma State University
in partial fulfillment of
the requirements for
the Degree of
DOCTOR OF PHILOSOPHY
July, 2017

OPTICAL RESPONSE OF UNDOPED AND DOPED ZINC OXIDE THIN FILMS

Dissertation Approved:

Don A. Lucca

Dissertation Advisor

Sandip P. Harimkar

Matthew J. Klopfstein

Pankaj Sarin

ACKNOWLEDGMENTS

I would like to thank my advisor, Dr. D.A. Lucca, for his guidance and support throughout my time working in his lab. The opportunities and responsibilities I have been given working on this project and many others have been invaluable in my development as a scientist. I would also like to thank all those who have served on my committee for their valuable time and helpful comments, Dr. S.P. Harimkar, Dr. M.J. Klopfstein, Dr. P. Sarin, Dr. S.W.S. McKeever, and the late Dr. R. Komanduri.

The assistance and support of Dr. Q. Jia, Dr. A. Chen, and Dr. Z. Bi. of the Center for Integrated Nanotechnologies is gratefully acknowledged.

I would like to thank all of the colleagues I have worked with in the Ultraprecision Surfaces Group over the years, in particular Mr. D.S. Hildebrand, Dr. S.A. Shojaee, Dr. Y. Qi, and Ms. A. Zare.

This work was performed, in part, at the Center for Integrated Nanotechnologies, an Office of Science User Facility operated for the U.S. Department of Energy (DOE) Office of Science by Los Alamos National Laboratory (Contract DE-AC52-06NA25396) and Sandia National Laboratories (Contract DE-NA-0003525).

This material is based upon work supported by the National Science Foundation under Grant No. CMMI-0529085. Any opinions, findings, and conclusions or recommendations expressed in this material are those of the author and do not necessarily reflect the views of the National Science Foundation.

Finally, I would like to thank my family, friends, and especially Lisa Overall for their continuing support and encouragement.

Acknowledgments reflect the views of the author and are not endorsed by committee members or Oklahoma State University.

Name: Tres A. Harriman

Date of Degree: July, 2017

Title of Study: OPTICAL RESPONSE OF UNDOPED AND DOPED ZINC OXIDE THIN FILMS

Major Field: Mechanical and Aerospace Engineering

Abstract:

The optical response of undoped and doped ZnO thin films was investigated. Epitaxial films were deposited on c-plane and r-plane sapphire using pulsed laser deposition and were characterized with a combination of photoluminescence (PL) spectroscopy, Raman spectroscopy, high resolution transmission electron microscopy (HR-TEM), x-ray diffraction (XRD), and Hall effect measurements. To investigate the effect of residual stress, undoped ZnO was used and the magnitude of residual stress was changed by varying the nominal film thickness from 5 nm to 200 nm. X-ray diffraction was used to measure the out of plane strain, which was used to estimate the residual stress. The residual stress and ZnO E_2^{high} Raman mode frequency were found to be related linearly by a factor of approximately -170 MPa/cm^{-1}, which is in agreement with high pressure investigations of bulk ZnO. PL experiments were performed at temperatures from 4.2 K to 300 K. Films created with a lower laser energy were found to have strong near band edge (NBE) emission, compared to those created with a higher laser energy that had poor emission intensity. For films on c-plane sapphire, fine PL structure including emission related to free-excitons, neutral-donor-bound-excitons, defects, a donor acceptor pair, and also phonon replicas of emissions were observed and identified. For films on r-plane sapphire the biggest difference in the PL emission compared to those on c-plane sapphire was the appearance of a free-electron to bound-acceptor emission that was attributed to acceptor states created by basal plane stacking faults. Doped films containing between 0 wt. % and 50 wt. % ReO_2 were also investigated. Low doping concentrations (5 and 10 wt. %) were found to improve the overall crystal quality and increase the conductivity. Films with higher concentrations of ReO_2 were found to have separate ReO_2 phases present. It remains unclear where the Re atoms are incorporated into the films at lower doping concentrations.

TABLE OF CONTENTS

1 INTRODUCTION **1**

1.1 Motivation for the Present Study 1

1.2 Objectives 2

2 BACKGROUND **3**

2.1 Effect of Strain on Semiconductors 3

2.2 Properties of ZnO 4

2.3 Transition Metal Doped ZnO and Re doped Semiconductors 5

2.4 Synthesis of Thin Films 7

2.5 Optical Spectroscopy 7

2.5.1 Photoluminescence Spectroscopy 7

2.5.2 Raman Spectroscopy 11

2.6 Confocal Microscopy 13

3 EXPERIMENTAL APPROACH **16**

3.1 Synthesis of Specimens 16

3.2 Instrumentation 16

3.2.1 Excitation Sources 17

3.2.2 Microscope Objectives 17

3.2.3 Confocal Pin-Hole 19

3.2.4 Monochromator/Detector 19

3.3 Probing Depth 20

4 RESULTS AND DISCUSSION **21**

4.1 Undoped ZnO 21

4.1.1 Frequency Shifts of the E_2^{high} Raman Mode Due to Residual Stress in Epitaxial ZnO Thin Films 21

4.1.2 Photoluminescence Response of Films on c-plane Sapphire 27

4.1.3 Photoluminescence Response of Films on r-plane Sapphire 44
4.1.4 Debye Temperature 52
4.2 Doped ZnO Thin Films 56

5 CONCLUSIONS AND FUTURE WORK **67**
5.1 Conclusions 67
5.2 Potential Future Work 70

Bibliography **71**

LIST OF TABLES

2.1 Room temperature wurtzite ZnO properties. 6

2.2 Raman active modes and their approximate positions for ZnO. 14

3.1 Absorption coefficient and approximate probing depth of ZnO using 325 nm and 532 nm excitation sources. 20

4.1 Substrates used for deposition of ZnO and the ZnO thin film thicknesses. 33

4.2 Summary of curve fitting results from PL spectra collected at 4.2 K for both c-plane ZnO (c-plane sapphire substrates) and a-plane ZnO (r-plane sapphire substrates) thin films, along with those of bulk single crystal ZnO. Energy values are in eV and FWHM values are in meV. 52

4.3 Debye temperatures reported in the literature for different types of ZnO with a variety of methods. 65

4.4 Fitting PL data as a function of temperature from Hamby et al. with the MW model using several different methods. 66

LIST OF FIGURES

2.1 Schematic showing the c-plane, a-plane, and r-plane in a hexagonal crystal structure. 5

2.2 Diagram of the excitation and recombination processes that can result in photoluminescence. 8

2.3 Energy level diagram of common NBE emissions from wurtzite ZnO including donor-bound excitons (D^0X), acceptor-bound excitons (A^0X), and free-excitons (FX_A,FX_B, FX_C). The energy levels are not to scale and details of the valence band splitting are shown in Fig. 2.4. 9

2.4 Band structure diagram showing valence band splitting of wurtzite ZnO (after Birman). 10

2.5 Interaction between light and matter. 11

2.6 Energy model of the Raman effect. 13

2.7 Diagram showing a confocal setup where rays from the focal plane pass through the pinhole and rays from other planes are blocked. 14

3.1 Schematic showing the components and beam path of the WITec Alpha SNOM configured in a reflection confocal mode, and the monochromator and CCD. (1) white light source, (2) 50:50 beamsplitter, (3) dichroic beamsplitter, (4) Raman edge filter and bandpass filter, (5) rotating turret holding three gratings, and (6) fiber coupler and a single mode fiber. 18

3.2 Integrated intensity of the 520 cm^{-1} Si peak as a function of focus distance with respect to the surface (positive value is above the surface) for different diameter fibers. System z-resolution is given by the FWHM. Other than fiber diameter, experimental parameters remained constant implying the decrease in the integrated intensity is the result of decreased signal throughput. 19

4.1 HR-TEM image of a 100 nm thick ZnO film showing a sharp interface between the film and substrate. The inset shows the electron diffraction pattern of the ZnO film on the c-plane sapphire substrate. 23

4.2 Out-of-plane lattice constant and corresponding estimate of biaxial stress in the ZnO films as a function of film thickness. The dashed line represents the reported lattice constant for bulk ZnO (5.2066 Å). The inset is a typical XRD 2Θ-scan pattern obtained from the 100 nm thick film, where the (0002)ZnO peak is used to calculate the out-of-plane lattice constant. 23

4.3 Raman spectra of the ZnO thin films on c-plane sapphire substrates. The markers are collected data points and the solid line is the cumulative fit of the fit peaks shown as dashed lines. For clarity the spectra have been offset vertically and the vertical line represents the stress-free position of the E_2^{high} peak. 25

4.4 Raman spectrum of bulk single crystal ZnO. 25

4.5 Biaxial stress of the ZnO films as a function of the shift in the E_2^{high} peak position from its stress-free position. 26

4.6 PL spectra for the 100 nm thick ZnO film on c-plane sapphire collected at temperatures from 4.2 K to 300 K. 28

4.7 PL spectra for the 50 nm thick ZnO film on c-plane sapphire collected at temperatures from 4.2 K to 300 K. 29

4.8 PL spectra for the 20 nm thick ZnO film on c-plane sapphire collected at temperatures from 4.2 K to 300 K. The discontinuity near 3.4 eV is an artificat of the monochromator. 30

4.9 PL spectra for 100, 50, 20, 10 and 5 nm thick ZnO films collected at 4.2 K. Left plot is on an absolute intensity scale and the right plot has been normalized to show peak locations. 31

4.10 PL spectra collected at 4.2 K from chemomechanically polished bulk single crystal ZnO, the 100 nm thick ZnO film in the thickness dependence study, and the 100 nm thick 0% ReO_2 ZnO film grown on c-plane sapphire in the ReO_2 study. 32

4.11 PL spectra for a 100 nm thick ZnO film on c-plane sapphire substrate for temperatures ranging from 4.2 K to 300 K (the intensity decreases with increasing temperature). . 34

4.12 Temperature dependent energy of several NBE emissions from the 100 nm thick ZnO film on c-plane sapphire. The 300 K FX_A energy for single crystal bulk ZnO was calculated using the band gap energy of bulk ZnO minus the exciton binding energy of 60 meV and is represented by the open square symbol. 37

4.13 Natural logarithm of the total intensity (product of the peak intensity and FWHM) of the D_3^0X peak as a function of inverse temperature. 38

4.14 PL spectra for a 50 nm thick ZnO film on c-plane sapphire substrate for temperatures ranging from 4.2 K to 300 K (the intensity decreases with increasing temperature). The slight discontinuity near 3.25 eV at the higher temperatures is not a real peak but is an artifact of the spectrometer. 40
4.15 Temperature dependent energy of several NBE emissions from the 50 nm thick ZnO film on c-plane sapphire. The 300 K FX_A energy for single crystal bulk ZnO was calculated using the band gap energy of bulk ZnO minus the exciton binding energy of 60 meV and is represented by the open square symbol. 41
4.16 PL spectra for a 30 nm thick ZnO film on c-plane sapphire substrate for temperatures ranging from 4.2 K to 300 K (the intensity decreases with increasing temperature). The slight discontinuity near 3.25 eV at the higher temperatures is not a real peak but is an artifact of the monochromator. 42
4.17 PL spectra for a 15 nm thick ZnO film on c-plane sapphire substrate for temperatures ranging from 4.2 K to 100 K (the intensity decreases with increasing temperature). The slight discontinuity near 3.25 eV at the higher temperatures is not a real peak but is an artifact of the monochromator. 43
4.18 Comparison between the PL spectrum of the 200 nm thick film on r-plane sapphire at 4.2 K to that of the 100 nm thick film on c-plane sapphire. The narrow peaks centered < 2.8 eV are not from the specimens but are instead laser lines. 45
4.19 PL spectra for a 200 nm thick ZnO film on r-plane sapphire substrate for temperatures ranging from 4.2 K to 300 K (the intensity decreases with increasing temperature). . 46
4.20 Temperature dependent energy of several NBE emissions from the 200 nm thick ZnO film on r-plane sapphire. 48
4.21 PL spectra for a 100 nm thick ZnO film on r-plane sapphire substrate for temperatures ranging from 4.2 K to 300 K (the intensity decreases with increasing temperature). . 49
4.22 Temperature dependent energy of several NBE emissions from the 100 nm thick ZnO film on r-plane sapphire. 50
4.23 PL spectra for a 50 nm thick ZnO film on r-plane sapphire substrate for temperatures ranging from 4.2 K to 300 K (the intensity decreases with increasing temperature). . 51
4.24 PL spectra for all the ZnO films on c-plane sapphire (top) and r-plane sapphire (bottom) collected at 4.2 K. 53
4.25 MW fittings of the temperature dependent free-exciton peak position for the 100 nm and 50 nm thick films. 54

4.26 HR-TEM image and SAED pattern of the ZnO films with 20 wt. % ReO_2. The figures on top correspond to the film on c-plane sapphire and those on the bottom are from the film on r-plane sapphire. 58
4.27 XRD patterns and FWHM of rocking curves for ZnO thin films on both c-plane and r-plane sapphire with various concentrations of ReO_2. 59
4.28 PL spectra for the ReO_2 doped ZnO films at 4.2 K. 61
4.29 Carrier concentration and carrier mobility as measured by Hall effect experiments for ReO_2 doped ZnO films. The lines are guides for the eye. 63

NOMENCLATURE

AFM ..... Atomic force microscopy

BP ..... Band pass

CCD ..... Charge-coupled device

CINT ..... Center for Integrated Nanotechnologies

d ..... Distance between grates

d_z ..... Depth resolution

DAP ..... Donor acceptor pair

D^0X ..... Exciton bound to a neutral donor

$e - A_0$ ..... Free-electron to bound-acceptor

E ..... Energy

E_{bulk} ..... Bulk band-gap

f ..... Focal length of monochromator

FWHM ..... Full width at half maximum

FX ..... Free-exciton

HR-TEM ..... High-resolution transmission electron microscopy

IR ..... Infrared

LANL ..... Los Alamos National Laboratory

LO ..... Longitudinal optical

MW ..... Manoogian-Woolley

n ..... Index of refraction

n ..... Carrier concentration

NA ..... Numerical aperture

NBE ..... Near-band edge

PL ..... Photoluminescence

PLD ..... Pulsed laser deposition

SAED ..... Selected area electron diffraction

SNOM ..... Scanning near-field optical microscopy

TES ..... Two-electron satellite

TO ..... Transverse optical

UV ..... Ultraviolet

W ..... Larger of the monochromator entrance width or CCD pixel size

XRD ..... X-ray diffraction

α ..... Absorption coefficient

ϵ ..... True strain

λ ..... Wavelength

μ_H ..... Carrier mobility (Hall mobility)

ω ..... Frequency

ρ ..... Density

σ ..... Stress

σ_{xx} ..... Biaxial stress

θ_o ..... Half angle of the objective

Chapter 1

INTRODUCTION

1.1 Motivation for the Present Study

Thin film ZnO has been widely investigated for potential use in optoelectronic devices that include solar cells, gas and chemical sensors, UV light sensors, and light emitting diodes. As a result, the optical and electrical properties of ZnO thin films have been widely reported. The properties of undoped films vary widely and are often dependent upon intrinsic defects and overall crystal quality achieved with the particular synthesis method being utilized. Intentionally doping ZnO with other elements is a common approach to tailor specific material properties, with the most common goal being to achieve p-type doping. There have been interesting results in other material properties, for example, increases in carrier mobility have been observed with In doping in ZnO, which would be beneficial for transparent conducting oxides [1]. Doping with group III and transition metal ions has also been investigated, typically with the goal of modifying the electrical, optical, or magnetic properties of ZnO. In this study, our goal in the doping of ZnO films with Re is to improve the electrical conductivity of the thin films without adversely affecting their optical properties. Changes in the optical response of the doped thin films will be a convolution of the effects of the presence of the dopant, and the effects of residual stress caused by the lattice mismatch between the ZnO and substrate, differences in thermal expansion between the ZnO and substrate, and the presence of the dopant and/or secondary phases that result. Although the electrical properties of some ZnO based films are measured in this study, the primary focus is on their optical properties.

1.2 Objectives

The overall objective of this study is to enhance the electrical conductivity of ZnO thin films by means of doping without substantially reducing optical transmittance. Improvement in the electrical conductivity would have a dramatic impact on the pursuit of using ZnO as an optically transparent conductive material in applications such as solar cells and displays. Changes in the optical response of the thin films will be a convolution of the effects of the presence of the dopant, and the effects of the resulting residual stress caused by both the lattice mismatch between the ZnO and the substrate and by the presence of the dopant. A better understanding of the effect of stress alone on the optical response of undoped ZnO thin films may have an immediate impact on the use of thin film ZnO in a variety of optoelectronic devices. An understanding of how stress and dopants have a combined effect on the optical and electrical response of ZnO may open avenues to tailor the optical properties of the films for specific applications by means of band-gap engineering.

Specifically, the objectives are to:

1. Evaluate the residual stress state of undoped ZnO as a function of film thickness. This is achieved by measuring the out-of-plane lattice strain with x-ray diffraction (XRD) and also measuring the variation in the Raman peak position as a result of the residual stress in the film.

2. Study the optical response of the undoped ZnO films as a function of temperature using photoluminescence (PL) spectroscopy. The quality of the films are investigated as a function of film thickness and compared to bulk single crystal ZnO. Effects of residual stress and crystal quality on the optical properties of the undoped films are studied.

3. The optical response of ReO_2 doped ZnO films are investigated with PL spectroscopy as a function of temperature and the results are compared to the measured electrical response of the films.

Chapter 2

BACKGROUND

2.1 Effect of Strain on Semiconductors

General effects of strain on bulk semiconductors have been widely reported and a number of books and reviews on the topic can be found [2, 3]. In some materials, the piezoelectric effect can lead to a voltage across the material as the result of an applied strain (or when subjected to an applied voltage the material will expand or contract). One practical implementation of strained semiconductors has been in recent complementary metal oxide semiconductor (CMOS) devices that take advantage of the fact that strain can improve the mobility of carriers (electrons and holes).

Strain is also known to modify the electronic band structure, which can affect the optical properties. Since the crystal symmetry is not changed under hydrostatic stress, the shape of the energy bands are unaffected by applied hydrostatic stress. There are however changes in the magnitude of the band-gap, with tensile stresses typically narrowing the band-gap and compressive stresses typically widening the band-gap. Under deviatoric stress (shearing) the crystal symmetry is no longer maintained, which can lead to splitting and/or warping of the energy bands. Often this leads to a splitting between the heavy hole valence band and the light hole valence band, which can lead to splitting of the photoluminescence (PL) peaks under applied stress, as has been reported for ZnSe [4]. The effect of shear stress on the conduction band is more complicated and varies with material. This variation is dependent upon the location of the conduction band edge within the Brillouin zone and the direction of the applied strain; in some cases splitting of the conduction band is observed and in some cases there is no splitting [3].

There have been several recent reports on the effect of intrinsic stress on the band-gap of ZnO thin films, ZnO quantum wells, and weakly confined ZnO nanoparticles. Kumar et al. [5] created

400 nm thick films with intrinsic stress that ranged from -0.172 to -8.4 GPa by varying the growth temperature. PL spectroscopy results indicated that the band-gap blue-shifted with increasing compressive stress such that $\Delta E_{stress}(meV) = -8.8\sigma(GPa)$. Li et al. [6] have also shown a linear relationship between the band-gap of ZnO thin films and biaxial stress. The effect of stress on ZnO nanocrystals resulting from the incorporation of Mg has been investigated both experimentally and theoretically. With increasing Mg concentration for 10 to 12 nm diameter $Zn_{1-x}Mg_xO$ nanocrystals, both the a- and c-lattice constants decreased and the band-gap continually blue-shifted [7]. Li-Bin et al. [8] investigated the theoretical effect of strain on $Mg_{0.25}Zn_{0.75}O$ for strains ranging from -0.2 to 0.3. Under both applied compressive and tensile strain on the a-axis, the bottom of the conduction band shifts to lower energy leading to a smaller band-gap. Under applied tensile strain on the c-axis the bottom of the conduction band again shifts to lower energy resulting in a smaller band-gap. However for compressive strain on the c-axis, the conduction band shifts to higher energy leading to an increased band-gap.

He et al. [9] investigated the effects of strain on the optical properties of Al-N co-doped ZnO films. By varying the concentration of the Al from 0 to 1 at. %, the compressive strain within the film could be varied from 0.2 to 2.2%. Absorption spectra were used to determine the band-gap of each film and it was found that the approximate relationship between band-gap energy and strain was $E_g(eV) = 3.237 + 0.025\epsilon$. Li et al. [10] measured the biaxial stress of ZnO films that had been grown on quartz and annealed at temperatures ranging from 240 to 800 °C. Due to increasing thermal mismatch stress, the biaxial tensile stress increased from 1.45 to 2.01 GPa as the temperature increased. The band-gap of the films was found to blue shift with increasing temperature and was related to the biaxial stress by $E_g(eV) = 3.160 + 0.048\sigma_{xx}(GPa)$, where σ_{xx} is the biaxial stress.

2.2 Properties of ZnO

ZnO has been the subject of extensive investigations for use in a broad range of potential devices including lasers and light emitting diodes [11,12], photodiodes [13], surface acoustic wave devices [14], gas sensors [15], and as a transparent conductor in photovoltaic cells and displays [16]. Much of this attention is the result of its wide direct bandgap (3.37 eV), large exciton binding energy (60 meV), low absorption in the visible wavelengths, and a number of other favorable optical, electrical, and piezoelectrical properties. The biggest hurdles facing the widespread integration of ZnO into many devices has been the difficulty in reliably achieving p-type doping, since it intrinsically exhibits n-type conductivity [17] and in producing good electrical contacts [18].

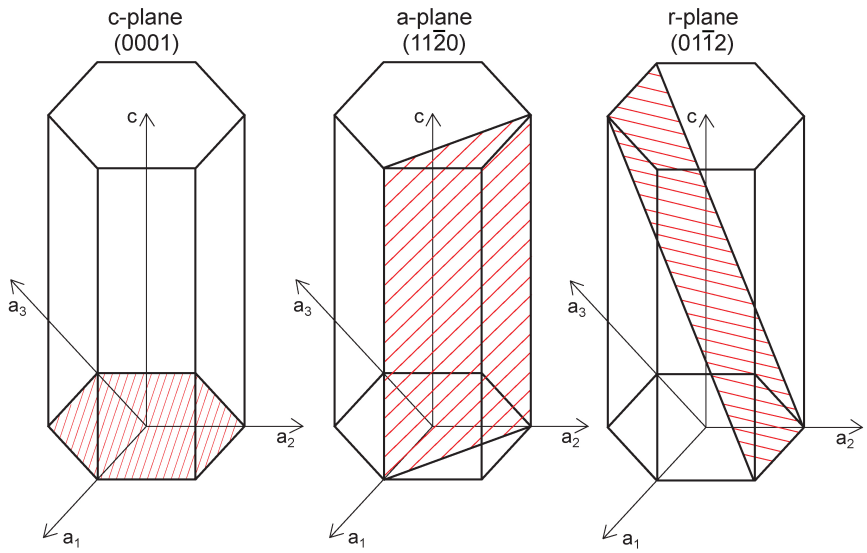

Figure 2.1: Schematic showing the c-plane, a-plane, and r-plane in a hexagonal crystal structure.

The most common crystal structure of ZnO is hexagonal wurtzite corresponding to the space group No. 186 ($P6_3mc$). Figure 2.1 shows the c-plane, a-plane, and r-plane in a hexagonal crystal. Some commonly reported material properties of wurtzite ZnO at room temperature are given in Table 2.1. Phase transformations to a rock salt structure (Fm3m) have been reported at high pressures [19] and zinc-blende crystal structures have been observed with growth on cubic substrates [20].

2.3 Transition Metal Doped ZnO and Re doped Semiconductors

To date, no reports related to the doping of ZnO with Re have been found. However, a limited number of studies on other semiconductors (often chalcogenides) doped with Re have been conducted. In this section an overview of the state of ZnO doped with transition metals will be given, followed by an overview of various semiconductors that have been doped with Re.

Doping ZnO with transition metals has attracted considerable attention, particularly with regard to creating dilute magnetic semiconductors (DMS). The solubility limit of Mn in ZnO under equilibrium conditions has been reported at $\sim 13\%$ [29]. Since many thin film growth techniques are non-equilibrium, Mn concentrations of more than 35% have been achieved while still maintaining a wurtzite crystal structure [30, 31].

The thermal solubility limit of Co in ZnO is 10 at.% [29]. Films grown by pulsed laser deposition

Table 2.1: Room temperature wurtzite ZnO properties.

Property	Symbol	Value	Source
Lattice parameters	a	3.2498 Å	[21]
	c	5.2066 Å	[21]
	c/a	1.6021	
Thermal expansion coeff.	α_a	4.31×10^{-6} K^{-1}	[22]
	α_c	2.49×10^{-6} K^{-1}	[22]
Carrier concentration	n	2×10^{16} to 5×10^{17} cm^{-3}	[23, 24]
Carrier mobility	μ_H	120 to 155 cm^{2}V^{-1}s^{-1}	[23, 25]
Melting temperature	T_m	2242 K	[26]
Density	ρ	5.676 g cm^{-3}	[27]
LO phonon energy	$\hbar\omega_{LO}$	72 meV	[28]
TO phonon energy	$\hbar\omega_{TO}$	54 meV	[28]

(PLD) have shown an increase in the c-lattice spacing of the ZnO with increasing Co content, which then plateaus when the Co content is 10% or higher [32]. Nanoclusters of Co have been observed in specimens having a Co content $\geq$ 12% [33]. Concentrations above 25% Co have resulted in the presence of Co_3O_4 peaks in XRD patterns indicating the segregation of a secondary phase [34].

Other transition metals including Ni [30, 31, 35], Cr [30, 31, 35], Fe [31, 35], and V [31, 35], have also been investigated for their potential as DMSs.

Since no studies have been found on the doping of ZnO with Re, the effect of doping other semiconductor materials may provide some insight into what could be expected in the case of ZnO.

Zhang et al. [36] investigated Re doped TiO_2 nano-powders for use as a photocatalyst for the treatment of water containing organophosphorous pesticides. Re concentrations as large as 6% were investigated and XRD measurements did not indicate the presence of any new phases as compared to undoped TiO_2. The photocatalytic performance of the Re-doped TiO_2 was much higher than that of the undoped material. It was suggested that a decrease in the bandgap and an increase in absorption of light in the visible spectrum as a result of the Re doping may be responsible for the increased efficiency.

2.4 Synthesis of Thin Films

Sapphire substrates have been most commonly used for the deposition of ZnO through techniques such as RF sputtering [37], molecular beam epitaxy [38], chemical vapor deposition [39], and pulsed laser deposition [40, 41]. Despite a lattice mismatch of 32% between ZnO and c-plane sapphire (hexagonal-on-hexagonal), it is possible to achieve epitaxial growth of ZnO on sapphire. This large mismatch is reduced to 18.4% by means of a 30° in-plane rotation of the ZnO relative to the c-plane sapphire [38]. Nevertheless, lattice mismatch can still lead to significant residual stresses, particularly in films having thicknesses less than 500 nm [42]. Recently a variety of cubic materials including $SrTiO_3$ (STO) [43] and MgO [44] have also been investigated as potential substrate materials for epitaxial ZnO thin films.

Pulsed laser deposition (PLD) is a form of physical vapor deposition. A target composed of the material that is to be deposited is placed in a vacuum chamber, along with the substrate that is to be coated. Depending upon the material that is to be deposited, reactant gases may be introduced back into the chamber. A high energy pulsed laser (usually an excimer laser) is directed at the target and each pulse ablates material and creates a plasma plume of target material. Some of the material in the plume will condense on the substrate, thus resulting in film growth. The rate of film growth is dependent upon many factors including the laser energy, chamber pressure, and geometry of the target/substrate/laser system, but a growth rate of 1 Å/pulse is typical [45].

2.5 Optical Spectroscopy

2.5.1 Photoluminescence Spectroscopy

Photoluminescence spectroscopy (PL) is a nondestructive technique that is useful in probing energy states and allowed electronic transitions in a material. In materials that are photoluminescence active, an incident photon with energy greater than the band-gap of the material is absorbed causing an electron to move from the valence band to the conduction band. This excited electron and its now empty location in the valence band (hole) is known as an electron-hole pair, or if they are bound, an exciton. When the excited electron returns to a lower energy state, a photon with less energy than the excitation source can be emitted. These processes are illustrated as a diagram in Fig. 2.2.

A near-band edge (NBE) emission occurs when an electron radiatively recombines with a hole, and the electron is originally located at a state near the edge of the conduction band and hole is located near the edge of the valence band. The energy of the NBE emission is quite close to that

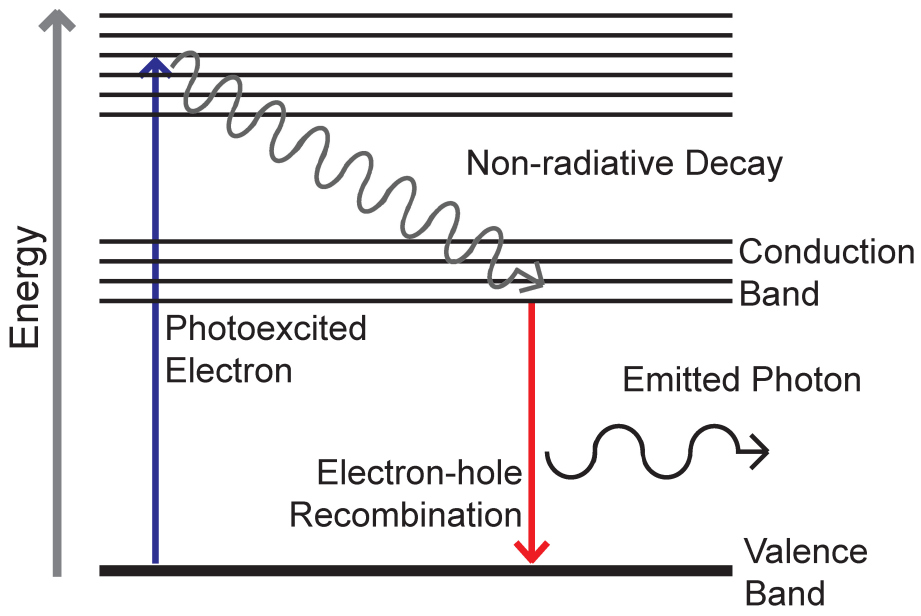

Figure 2.2: Diagram of the excitation and recombination processes that can result in photoluminescence [46].

of the energy of the material's band-gap. A defect emission occurs when the electron recombination involves a defect state whose energy lies in the mid-band-gap. PL emission related to defect states will vary depending upon the energy level of the defect and the overall concentration of the defects. By analyzing the energy of the re-emitted light, insight into the band-gap, defect levels, defect types, and defect concentrations can be obtained.

The investigation of ZnO luminescence is typically focused on either the utraviolet NBE emission or visible defect emission. More details of the various defect emissions can be found elsewhere [17], but they result in a recombination involving a defect state within the bandgap. These defects can be either intrinsic (e.g., vacancies, interstitials, anti-sites, dislocations, grain boundaries, or surfaces) or extrinsic (e.g., dopants or impurities). The most commonly observed defect emission is the so-called green defect emission, named for its energy of 2.5 eV. The most widely accepted source of the green defect emission involves a singly charged oxygen recombining with a photoexcited hole [47]. However this continues to be widely debated and has more recently also been attributed to zinc vacancies [48], oxygen anti-sites [49], zinc interstitials [50], and even a complex defect located in the near surface region [51, 52].

The NBE emission of ZnO primarily arises from luminescence involving states within the band gap that are close in energy to either the conduction band or valence band. Examples of such

emissions include free-excitons (FX), donor-bound-excitons (D^0X), and acceptor-bound-exciton as illustrated in the energy diagram in Fig.2.3. Further details of the various NBE emissions in ZnO follow.

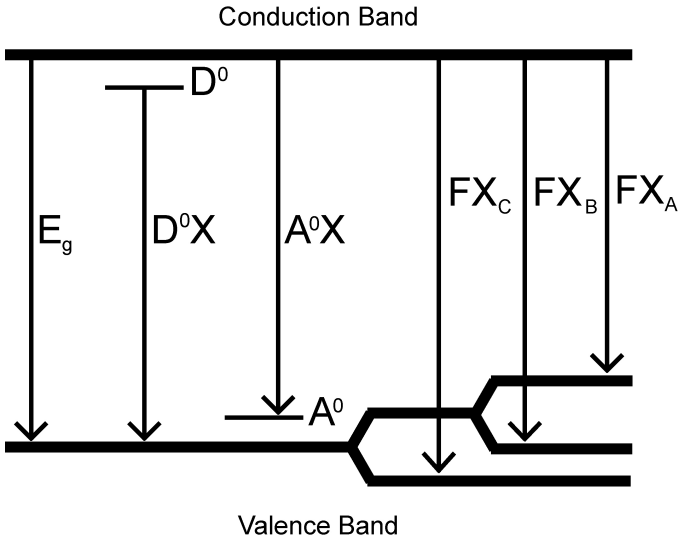

Figure 2.3: Energy level diagram of common NBE emissions from wurtzite ZnO including donor-bound excitons (D^0X), acceptor-bound excitons (A^0X), and free-excitons (FX_A,FX_B, FX_C). The energy levels are not to scale and details of the valence band splitting are shown in Fig. 2.4.

For wurtzite ZnO the conduction band is s-like with Γ_7^c symmetry, while the valence band is p-like and split into three distinct bands (one with Γ_9 symmetry and the other two with Γ_7 symmetry) as a result of crystal-field splitting and spin-orbit interactions [53]. Free-exciton transitions involving each of the three valence bands are denoted by A (heavy hole), B (light hole), and C (crystal-field split band), as shown in Fig. 2.4. The first observation and identification of A, B, and C peaks in ZnO was reported by Thomas [54] and at 4.2 K were centered at 3.377 eV, 3.3845 eV, and 3.4225 eV, respectively.

Bound-exciton luminescence occurs from the recombination of an exciton that is trapped or bound to a defect within the crystal. At lower temperatures it is often energetically favorable for free excitons to bind to defects or impurities within the material [56]. The photon emitted during bound-exciton luminescence has an energy that is lower than the free-exciton emission energy by an amount equal to the binding energy of the exciton to the particular defect. This binding energy is typically in the the range of 5 meV to 20 meV. At low temperatures, the luminescence emission from ZnO is usually dominated by very narrow neutral-donor-bound-exciton emission in the spectral range of

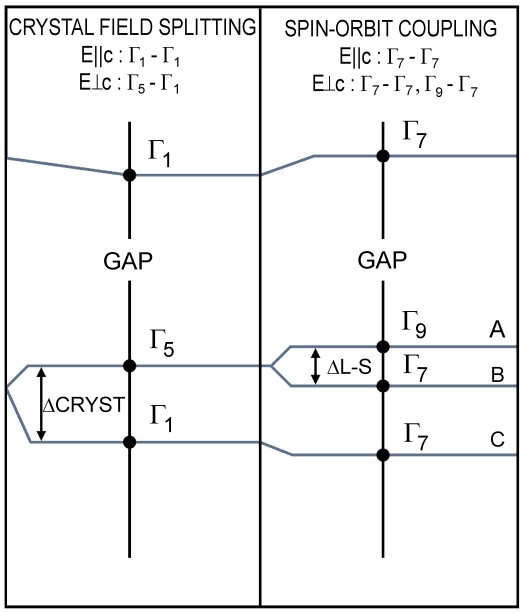

Figure 2.4: Band structure diagram showing valence band splitting of wurtzite ZnO (after Birman [55]).

3.348 eV to 3.374 eV. The exact number, energy, and relative intensity of the bound-exciton emissions in ZnO varies dramatically [57–60]. As many as eight neutral-donor-bound-exciton emissions have been observed from a single ZnO specimen, with nearly all related to the A exciton. The subscript nomenclature used by Teke et al. (e.g., D_1^0X) will be used when there is agreement with the energy of the observed emission in this study and their reported values. At a slightly lower energy than the neutral-donor-bound-excitons (3.3481 eV to 3.3564 eV), the appearance of as many as three neutral-acceptor-bound-excitons have also been reported.

In the spectral range of 3.32 eV to 3.34 eV, two-electron satellite (TES) transitions are common in ZnO. These transitions are the result of a bound-exciton recombining and leaving the neutral donor in an excited state [61]. The TES emission has an energy that is less than the donor-bound-exciton emission by the energy difference between the excited and ground state of the donor. In the spectral range less than ~ 3.3 eV the most common emissions are LO-phonon replicas of the higher energy emissions (the LO phonon energy for ZnO is 72 meV) and in some cases emission from donor acceptor pairs (DAP) [57].

2.5.2 Raman Spectroscopy

Raman spectroscopy is another nondestructive technique that is useful in probing the chemical bonding nature of materials. Although the effect was discovered in 1928 by Sir C.V. Raman [62], Raman spectroscopy did not see widespread use until the mid-1960s with the arrival of commercially available, reliable, continuous wave lasers [63]. The Raman effect is the result of a photon being inelastically scattered, where either the creation or annihilation of a phonon results in a net energy change of the incident photon [64]. As seen in Fig. 2.5, when incident light interacts with an object surface there are a variety of paths that the photon can take. At the surface of the material the light is either reflected or transmitted. Once inside the material, the light can take part in the PL process as described earlier, or it can be scattered either elastically or inelastically.

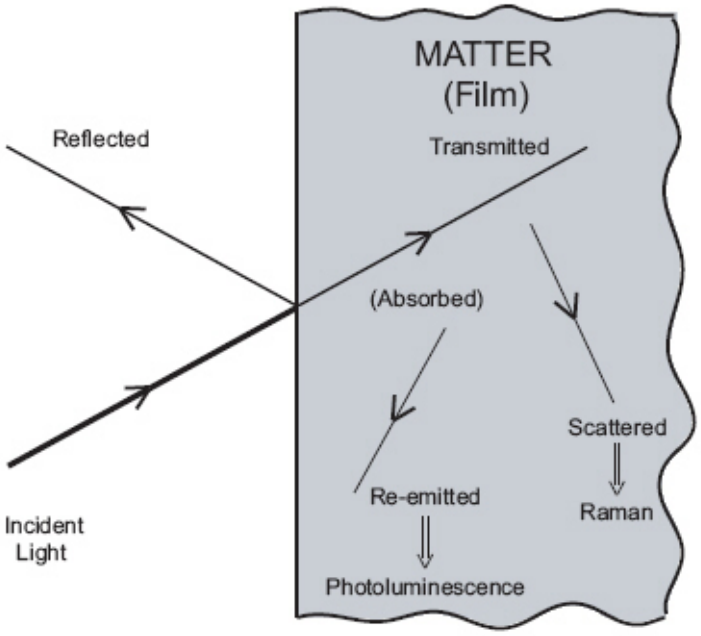

Figure 2.5: Interaction between light and matter.

If we consider the energy diagram shown in Fig. 2.6, for an elastically scattered photon, referred to as Rayleigh scattering, the incident and resulting radiation have the same energy. In the case of an inelastically scattered photon (Raman scattering), there is a net energy difference between the incident and resulting radiation. If the net change of energy is positive, then the resulting photon has a higher frequency than the incident light and the shift is known as an anti-Stokes shift. If however, the net change is negative, then the resulting photon has a lower frequency than the incident light

and the shift is termed a Stokes shift.

Rayleigh scattering is the most intense of these processes and results in re-emitted light that is about three orders of magnitude less in intensity than the incident excitation. In comparison, Raman scattered light is usually eight to twelve orders of magnitude less in intensity than that of the incident excitation. Comparing the Raman Stokes and anti-Stokes shifts, the Stokes shift results in more intense emission at room temperature since more initial states are at the ground state rather than at a vibrationally excited state. With changes in temperature, the overall system experiences a change in the population of vibrationally excited states; lower temperatures lead to fewer phonons in the lattice and more intense Stokes Raman lines. In fact, it is possible to measure the temperature of the specimen to within 5 K by measuring the intensities of both the Stokes and anti-Stokes Raman lines [65].

A disadvantage of Raman spectroscopy is the low signal strength of Raman scattering. Fluorescence emission is six to eight orders of magnitude stronger than that of Raman scattering [63]. If a Raman shift occurs in the same region of the spectrum as a fluorescence emission, the Raman signal will not be detectable. This can be overcome by changing the wavelength of the excitation source to either a UV or near-IR excitation. Changing the excitation wavelength can also be useful to probe different depths of material since the absorption coefficient of a material is dependent upon the wavelength of light. Another approach to avoid problems associated with fluorescence is to take advantage of the photobleaching effect. Some fluorescing materials will breakdown with a sufficiently long time under excitation causing a decrease in the fluorescence intensity. By allowing the material to photobleach, Raman scattering that would otherwise be undetectable can be observed.

Although Raman shifts are occasionally reported in units of energy (eV) or frequency (Hz), the most commonly used units are wavenumbers (cm^{-1}). Typically, relative wavenumbers are used; the relative wavenumber of a Raman mode is the difference in absolute wavenumbers of the Raman scattered photons and the excitation source. In order to find the absolute wavenumber of a quanta, one simply takes the inverse of its wavelength.

For a Raman spectroscopy system there are a few key components required, a monochromatic light source (e.g., a laser), a set of collection optics, a means for dispersing the scattered light (e.g., a monochromator), and a light detector (e.g., a charge-coupled device (CCD) camera). The light source is typically a continuous wave laser in the visible region of the spectrum. Care should be taken when choosing the specific wavelength of the excitation laser. Both PL emission and the fact that the Raman scattering cross section varies as the fourth power of the excitation frequency must be considered [66]. This implies that for a constant laser power, a given Raman peak will increase

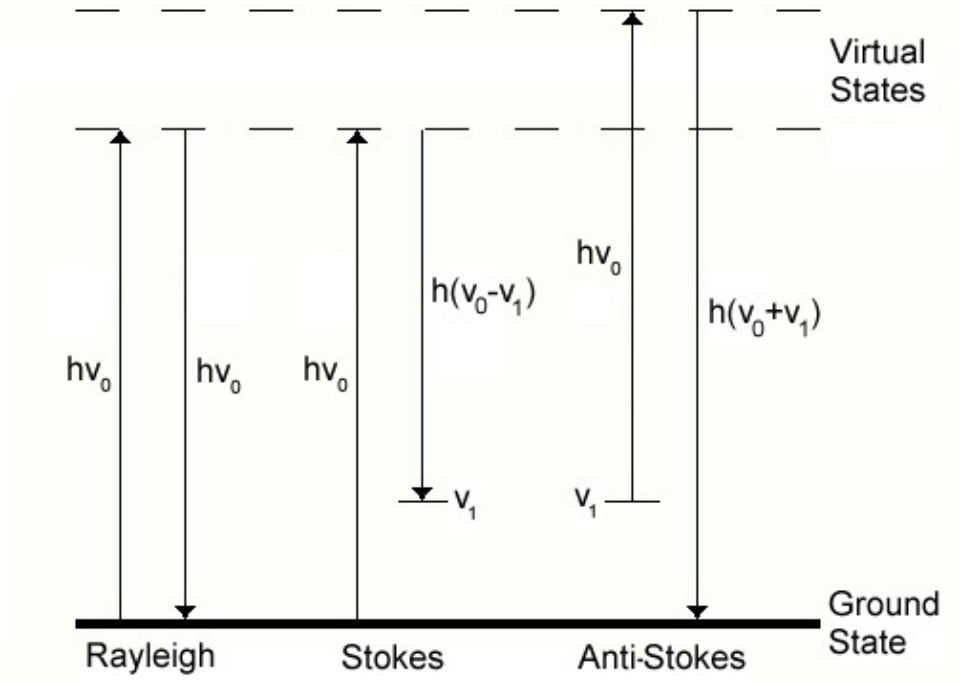

Figure 2.6: Energy model of the Raman effect.

in intensity as the wavelength of the excitation source becomes shorter.

A method of eliminating the high intensity Rayleigh scattering is also desirable, in order to achieve a high signal to noise ratio. This can be accomplished with the use of multiple monochromators or optical filters, such as notch type (transmits both Stokes and anti-Stokes scattering), longpass edge type (transmits only Stokes scattering), or shortpass edge type (transmits only anti-Stokes scattering).

Under ambient conditions, wurtzite ZnO has six Raman active vibration modes. These modes and their approximate position are summarized in Table 2.2. The E_2 modes are the most intense peaks relative to the other modes, particularly in a backscattered experimental setup, and are non-polar [67]. The A_1(TO), E_1(TO), and E_1(LO) are polarized in the xy-plane, and the A_1(LO) mode is polarized along the z-axis.

2.6 Confocal Microscopy

The confocal microscope, invented in 1957, requires two key components in order to produce an image [69]. First, a diffraction limited excitation spot that can be scanned across the specimen; second, a way to collect the re-emitted light from the specimen and focus it onto a pinhole aperture. Light that passes through the pinhole can then be sent to a photosensitive device for analysis. As

Table 2.2: Raman active modes and their approximate positions for ZnO [68]

Raman Active Mode	Rel. Wavenumber (cm^{-1})
$A_1(TO)$	380
$A_1(LO)$	574
$E_1(TO)$	407
$E_1(LO)$	583
E_2^{low}	101
E_2^{high}	437

seen in Fig. 2.7, the advantage of using a confocal pinhole, as opposed to a conventional far-field microscope, is that light emitting from positions outside of the focal plane is rejected, thus achieving a small depth of field. In addition to the vast improvement in depth resolution as compared to a standard microscope, there is some improvement in the lateral resolution as well.

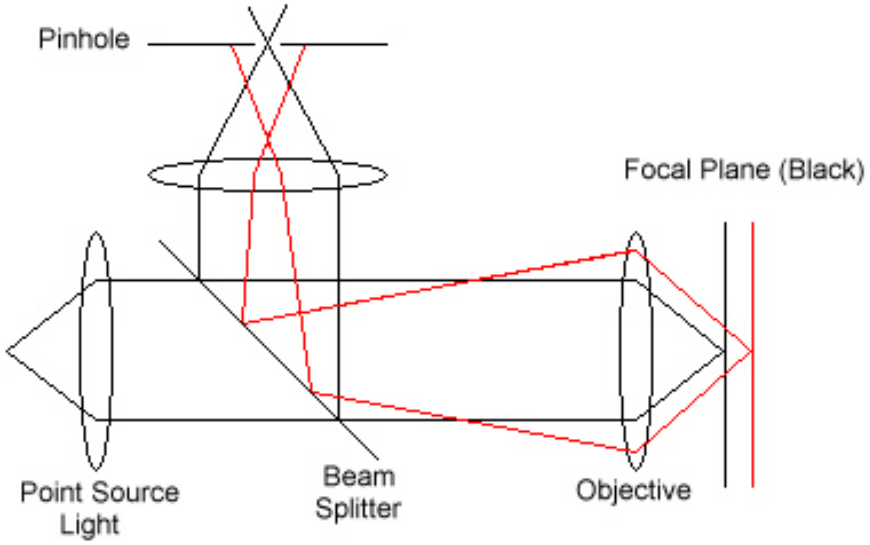

Figure 2.7: Diagram showing a confocal setup where rays from the focal plane pass through the pinhole and rays from other planes are blocked.

The theoretical depth resolution for an infinitely small aperture is given by

$$d_z = \frac{0.45\lambda}{n(1 - cos\theta_o)} \approx \frac{0.90\lambda}{NA^2}, \tag{2.1}$$

where λ is the excitation wavelength, n is the index of refraction of the medium between the objective and sample (assumed to have a value of 1 for air), θ_o is the half angle of the objective, and NA is the numerical aperture of the objective. The actual system resolution will be limited by the finite pinhole size as well as the incoherent Raman or fluorescent signal.

To find the actual resolution of a complete confocal Raman system, a technique is used that measures the intensity of the 520 cm^{-1} Si peak as a function of z focal location [70, 71]. Starting with the focal point 10 μm above the Si surface, the microscope is incrementally moved to a focal point 10 μm below the surface, recording Raman spectra along the way. The full width at half maximum (FWHM) of the intensity vs. focal point z distance gives a good approximation of the depth resolution.

In a conventional microscope in air, the maximum lateral resolution is $2\lambda/3$, while the maximum lateral resolution for a confocal microscope is $\lambda/2$.

Chapter 3

EXPERIMENTAL APPROACH

3.1 Synthesis of Specimens

Synthesis of the films was performed at the Center for Integrated Nanotechnologies (CINT) at Los Alamos National Laboratory (LANL). ZnO thin films were deposited on c-plane sapphire substrates using pulsed laser deposition (PLD). A KrF excimer laser (λ=248 nm) with a pulse frequency of 2 Hz was directed at a ceramic ZnO (or ZnO/ReO_2) target at a 45° angle of incidence. The deposition conditions were initially optimized for the narrowest x-ray rocking curve and then maintained throughout the experiments. Briefly, the depositions were performed with an O_2 pressure of 350 mTorr and a substrate temperature of 650 °C. By varying the deposition time, the thickness of the resulting films could be controlled. Undoped ZnO films had nominal thicknesses between 5 nm and 100 nm and doped films all had a nominal thickness of 100 nm.

3.2 Instrumentation

There were two different instruments available to conduct the optical spectroscopy investigations. The first was a conventional far-field photoluminescence (PL) spectroscopy setup using the 3.82 eV (325 nm) line from a HeCd laser as the excitation source. Emitted light was dispersed by a 0.5 m monochromator using a 2400 groove/mm grating and detected by a LN_2-cooled charge coupled device (CCD) camera. With the use of a continuous flow cryostat, the specimen temperature was varied between 4.2 K and 300 K. Additional details and specifications of this particular system follow and can also be found elsewhere [72].

The second system is a commercially available combination confocal microscope and scanning

near-field optical microscope (SNOM) (WITec, GmbH). For the purposes of this study, the confocal microscopy mode of the system was employed for the Raman spectroscopy experiments. The 2.33 eV (532 nm) line from a frequency doubled Nd:YAG laser was used to perform Raman spectroscopy. A schematic of the system components and beam path is shown in Fig. 3.1. Additional details and specifications of key components of the system follow.

3.2.1 Excitation Sources

For the PL experiments a continuous wave Kimmon IK3151R-E helium cadmium (HeCd) laser operating at an energy of 3.82 eV (325 nm) was used. The beam output (TEM00) is rated at a maximum power of 17 mW. For the far-field PL configuration the laser was focused directly onto the specimen with a spot size of approximately 3 mm.

For the confocal Raman experiments a continuous wave frequency doubled Nd:YAG laser operating at an energy of 2.33 eV (532 nm) was used. The laser was coupled with the microscope with a polarization maintaining optical fiber having a core diameter of 3.5 μm. At the output end of the fiber the maximum laser power was measured to be about 8 mW. Power output from the fiber can be varied by adjusting a micrometer screw integrated into the fiber coupler. Experiments were conducted with the same laser power, which was set to a minimum value to achieve a strong enough signal to noise ratio, but to avoid heating of the specimen. The incident laser light was linearly polarized and aligned with the x-axis of the microscope stage. All polarizations were collected and allowed to be focused onto the confocal pin-hole.

3.2.2 Microscope Objectives

In the WITec system, standard microscope objectives are mounted on an upright objective turret. One of the objective positions has the mounting armature for either an atomic force microscopy (AFM) cantilever or a scanning near-field optical microscopy (SNOM) cantilever, as well as the inertial drive to control its movement. This allows different types of measurements to be made, either confocal microscopy, AFM, and/or SNOM, on the same region of the specimen. The instrument also has the ability to collect light in transmission using an objective that is mounted in an inverted position beneath the specimen stage. For Raman experiments where the Nd:YAG laser was used with a 100x/0.9NA Nikon objective, the approximate spot size on the specimen was 0.4 μm. The scattered light was collected with the same objective (a back-scattering arrangement).

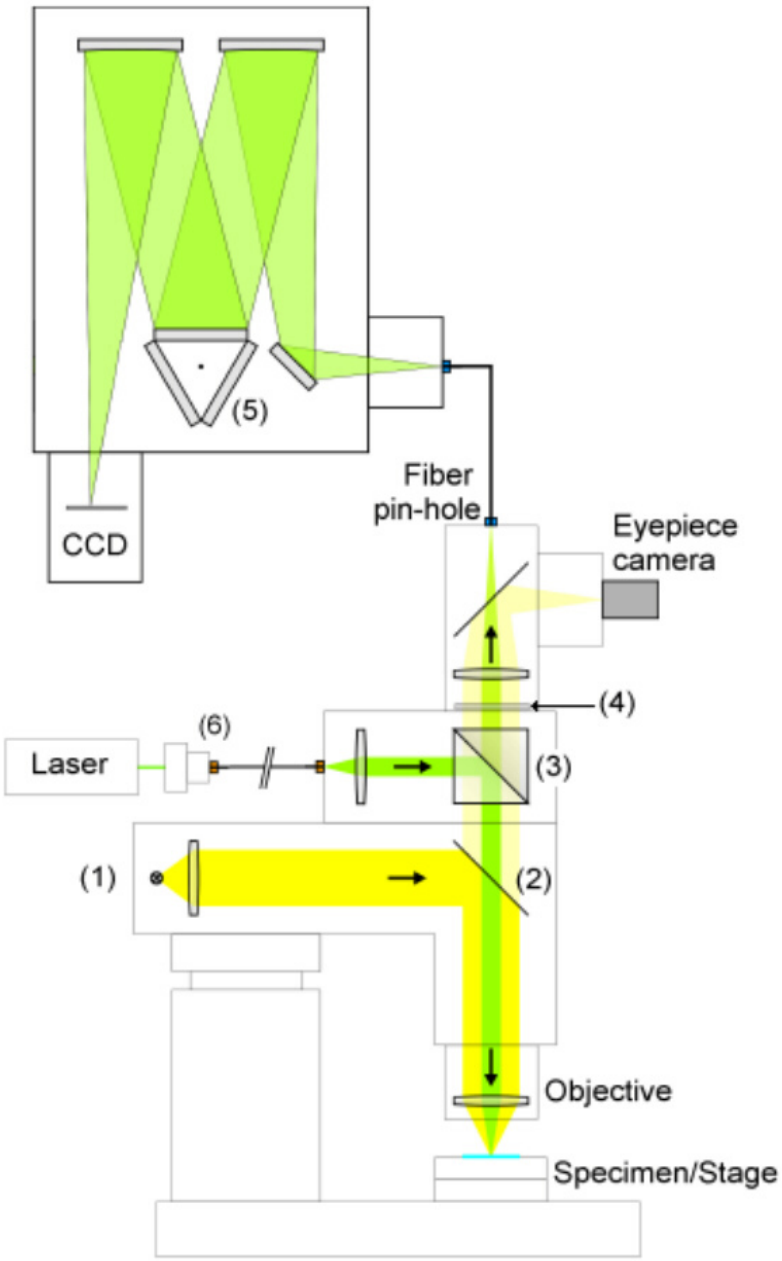

Figure 3.1: Schematic showing the components and beam path of the WITec Alpha SNOM configured in a reflection confocal mode, and the monochromator and CCD. (1) is a white light source, (2) is a 50:50 beamsplitter, (3) is a dichroic beamsplitter, (4) is a Raman edge filter and bandpass filter, (5) is a rotating turret holding three gratings, and (6) is the fiber coupler and a single mode fiber. (Modified from the Alpha SNOM Operating Manual.)

3.2.3 Confocal Pin-Hole

In the WITec system, scattered or re-emitted light that is collected by the objective is focused onto the end of a UV-visible multimode optical fiber, which acts as the confocal pin-hole. A total of three different fibers are available, with core diameters measuring 100, 50, and 25 μm. Decreasing the pin-hole (core diameter) size results in an increase in z-resolution, but at the cost of signal throughput. According to Eq. (2.1) the theoretical confocal depth resolution using the 100x objective and 532 nm Nd:YAG laser is 585 nm. The actual depth resolution of our system as measured by the technique described in Section 2.6, and shown in Fig. 3.2, is 1.21, 0.82, and 0.62 μm for 100, 50, and 25 μm diameter fibers, respectively. Only the 100 μm fiber was used in this study to maximize the signal intensity.

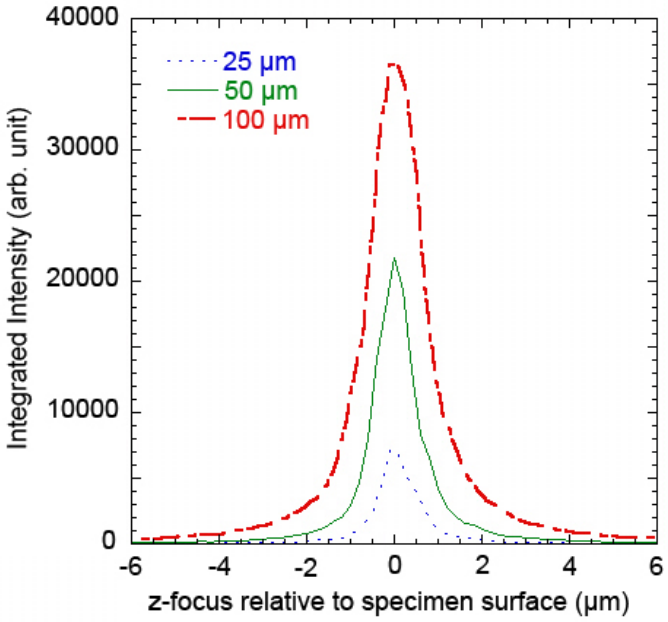

Figure 3.2: Integrated intensity of the 520 cm^{-1} Si peak as a function of focus distance with respect to the surface (positive value is above the surface) for different diameter fibers. System z-resolution is given by the FWHM. Other than fiber diameter, experimental parameters remained constant implying the decrease in the integrated intensity is the result of decreased signal throughput [46].

3.2.4 Monochromator/Detector

The far-field PL experimental setup used a 0.5 m Spex monochromator with a 2400 groove/mm diffraction grating holographically blazed at 400 nm to disperse the luminescence. The light was

detected with a liquid nitrogen cooled charge coupled device (CCD) from Jobin Yvon. The 1024 x 128 pixel detector had individual pixels that were 26 x 26 μm. The band pass of a monochromator is given by $BP = Wd/f$, where W is the larger of the entrance width or CCD pixel size, d is the distance between grooves, and f is the monochromator focal length. The band pass for the Spex monochromator and Jobin Yvon CCD was 0.0217 nm, giving a resolution of approximately 0.5 meV near the bandgap energy of ZnO.

In the WITec system, light passing through the confocal pin-hole was directed by the optical fiber to a 0.3 m Acton monochromator. Light was dispersed with either a 150, 600, or 1800 groove/mm diffraction grating, each holographically blazed at 500 nm. All gratings are attached to a rotating turret, allowing for the selection of the grating without opening the monochromator. Light was detected with a 1024 x 128 pixel, thermoelectrically cooled ($-73\,^{\circ}$C) CCD from Andor Technology. The band pass for the 0.3 m Acton monochromator using the 150, 600, and 1800 groove/mm gratings is 0.578, 0.144, and 0.0481 nm, respectively (giving resolutions of 23, 5.8, and 1.9 cm^{-1} for Raman spectroscopy).

3.3 Probing Depth

From the Beer-Lambert-Bouguer law, the ratio of light intensity at depth z under the surface to the incident light intensity is given as $I(z)/I_o = exp(-\alpha z)$, where α is the absorption coefficient for the particular wavelength of interest. The absorption depth is given by the distance in the material in which 63.2 % of the incident light is absorbed (i.e., $I(z)/I_o = 1/e$) [73]. This gives the absorption depth as the inverse of the coefficient of absorption. Since a back-scattered arrangement is used, scattered or re-emitted light must travel to a depth of z and then back through the same distance of material to reach the surface in order to be detected. This configuration implies that the probing depth is given as $1/2\alpha$. Table 3.1 gives values for absorption coefficients of ZnO and probing depths for each laser source.

Table 3.1: Absorption coefficient and approximate probing depth of ZnO using 325 nm and 532 nm excitation sources.

	$\lambda = 325$ nm		$\lambda = 532$ nm	
	α (cm^{-1})	Depth	α (cm^{-1})	Depth
ZnO	~160,000 [41]	30 nm	~8,500 [41]	600 nm

Chapter 4

RESULTS AND DISCUSSION

4.1 Undoped ZnO

4.1.1 Frequency shifts of the E_2^{high} Raman mode due to residual stress in epitaxial ZnO thin films [74]

Many potential devices and applications for ZnO require the use of thin films, however one significant challenge has been to develop an understanding of the effect of stress on the optical properties due to the lattice strain in heteroepitaxial ZnO films on different substrates. Residual stress within epitaxial thin films usually results from a combination of differences in coefficients of thermal expansion (thermal mismatch) and differences in atomic lattice spacing (lattice mismatch) between the film and substrate materials. An understanding of the resulting residual stress and a method to easily characterize it are important for the development and optimization of devices that use ZnO thin films.

Typically the residual stress is determined by measuring the out-of-plane lattice strain using x-ray diffraction (XRD) [42, 75, 76]. Raman spectroscopy has been widely used to qualitatively determine the residual stress state of ZnO thin films, but its use in quantitative analysis has been limited to high pressure investigation of bulk ZnO using diamond anvil cells [68, 77, 78] and thin films of other material systems such as AlN [79]. In a recent study [74] the residual stress of ZnO thin films was investigated as a function of thickness for films deposited on c-plane sapphire substrates using pulsed laser deposition (PLD). The results of residual stress with film thickness are then directly compared to the observed frequency shifting of the ZnO E_2^{high} Raman mode.

ZnO thin films were deposited on c-plane sapphire substrates using PLD. A KrF excimer laser

(λ=248 nm) with a pulse frequency of 2 Hz was directed at a ceramic ZnO target at a 45° angle of incidence. The deposition conditions were initially optimized for the narrowest x-ray rocking curve and then maintained throughout our experiments. The depositions were performed with an O_2 pressure of 350 mTorr, a substrate temperature of 650 °C, and a laser energy of 3 J/cm^2. By varying the deposition time, the resulting films had nominal thicknesses between 5 and 100 nm. After growth, the films were characterized with a combination of XRD, high-resolution transmission electron microscopy (HR-TEM), and Raman spectroscopy. XRD experiments were performed at LANL with a PANalytical MRD PRO x-ray diffractometer using Cu K_α radiation (λ= 1.5418 Å). The HR-TEM measurements were also performed at LANL with a FEI Tecnai F30 transmission electron microscope operating at 300 kV with a point to point resolution of 0.21 nm. Raman spectroscopy was performed at room temperature using a confocal microscope and the 532 nm line from a frequency-doubled Nd:YAG laser. Laser light was focused on the specimen with a 100x/0.9NA microscope objective and the scattered light was re-collected with the same objective and focused onto a 100 μm optical fiber acting as a confocal pin-hole. The light was then dispersed by a 0.3 m monochromator using an 1800 groove/mm grating and detected by a thermoelectrically-cooled charge coupled device (CCD) camera.

As illustrated by the HR-TEM image shown in Fig. 4.1, the resulting films were found to have a sharp interface between the film and the substrate and were highly epitaxial with respect to the c-plane sapphire substrates as evidenced by the selected electron diffraction pattern shown in the inset of Fig. 4.1. From both the XRD analysis and the electron diffraction pattern, the epitaxial relationship between the film and the substrate can be described as $(0001)_{\mathrm{ZnO}}||(0001)_{\mathrm{sapphire}}$ and $[10\bar{1}0]_{\mathrm{ZnO}}||[2\bar{1}\bar{1}0]_{\mathrm{sapphire}}$, which is consistent with previous reports [80].

To determine the lattice strain of the ZnO films, the out-of-plane lattice parameter was calculated from the 2Θ position of the (0002)ZnO diffraction peak using Bragg's law. Figure 4.2 shows the measured out-of-plane lattice constant c, as a function of film thickness and the inset shows a typical XRD 2Θ-scan pattern that was collected from the specimens. For all but the thickest film a lattice constant smaller than that for bulk ZnO (5.2066 Å) [21] was observed, indicating a state of compressive residual out-of-plane stress. With increasing film thickness the measured lattice constant approached that of bulk ZnO, indicating the residual stress was relieved. This reduction in out-of-plane stress with increasing film thickness is consistent with reports in the literature for epitaxial films and has been attributed to a transition from 2D layer growth to 3D columnar growth in the film that leads to a relaxation of the stress [42].

To estimate the magnitude of the residual stress state of the films, a biaxial state of stress was

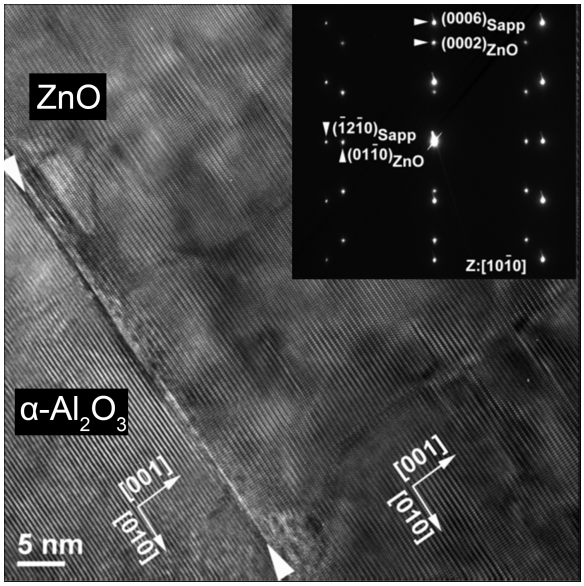

Figure 4.1: HR-TEM image of a 100 nm thick ZnO film showing a sharp interface between the film and substrate. The inset shows the electron diffraction pattern of the ZnO film on the c-plane sapphire substrate [74].

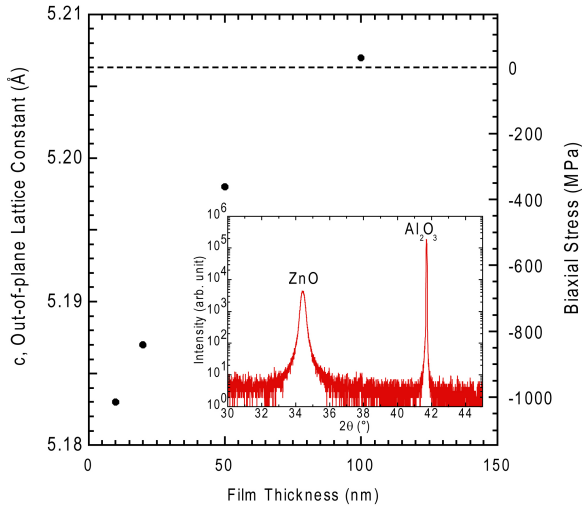

Figure 4.2: Out-of-plane lattice constant and corresponding estimate of biaxial stress in the ZnO films as a function of film thickness. The dashed line represents the reported lattice constant for bulk ZnO (5.2066 Å) [21]. The inset is a typical XRD 2Θ-scan pattern obtained from the 100 nm thick film, where the (0002)ZnO peak is used to calculate the out-of-plane lattice constant [74].

assumed in which the out-of-plane stress was zero ($\sigma_z = 0$). The stress in the film is then given as

$$\sigma_{film} = (\sigma_x + \sigma_y)/2 = [C_{13} - C_{33}(C_{11} + C_{12})/2C_{13}]\epsilon_z \tag{4.1}$$

where C_{ij} are the elastic stiffness components, and $\epsilon_z = (c - c_0)/c_0$ is the out-of-plane lattice strain. Using the reported elastic stiffness components for bulk single crystal ZnO [81], Eq. 4.1 reduces to $\sigma_{film} = -227(c - c_0)/c_0 = -227\epsilon_z$ GPa where c is the measured lattice constant and c_0 is the unstrained lattice constant, 5.2066 Å. Whereas previous measurements of ZnO films grown on c-plane sapphire by RF magnetron sputtering have resulted in different values of C_{ij} compared to that of bulk ZnO [82], the use of these thin film values in Eq. 4.1 results in a nearly identical relationship to that shown above ($\sigma_{film} = -225\epsilon_z$ GPa). The estimated biaxial stress as a function of film thickness is shown in Fig. 4.2. The biaxial stress was found to be relieved with increasing film thickness, which is expected considering that the lattice strain of thin films will be relaxed for films thicker than a critical thickness.

Raman spectroscopy was performed on the specimens and the resulting spectra in the vicinity of the ZnO E_2^{high} peak are shown in Fig. 4.3. To compare the Raman response of the thin films to that of bulk single crystal ZnO, Raman spectroscopy was also performed on bulk single crystal ZnO produced by Eagle-Picher that was grown by the seeded chemical vapor transport (SCVT) method [83]. As shown in Fig. 4.4, the Raman spectrum for the bulk crystal exhibited three distinct Raman peaks centered at 333.4, 439.4, and 1159 cm^{-1}. The peaks at 333.4 cm^{-1} and 1159 cm^{-1} are associated with overtones of multiple vibration modes, while the peak at 439.4 cm^{-1} is due to the E_2^{high} vibration mode [84]. For the 100 nm thick film, the same three ZnO peaks were also observed, in addition to multiple peaks originating from Al_2O_3 vibrational modes in the sapphire substrate. With decreasing film thickness, the ZnO Raman peaks decreased in intensity. To determine the frequency of the E_2^{high} peak from each film, fittings were performed using Gaussian line shapes. Since the E_2^{high} peak is located between two Al_2O_3 Raman peaks, it was necessary to fit three separate peaks over the spectral range from 425 to 460 cm^{-1}. Since the 5 nm thick film showed no obvious E_2^{high} peak due to its small thickness, the spectrum from this film was used to determine the frequency and width of the Al_2O_3 peaks which were then used for fitting of the spectra from the other films. These Al_2O_3 peaks were centered at 431.0 and 449.7 cm^{-1} and had full width at half maximums (FWHMs) of 9.3 and 6.8 cm^{-1}, respectively. With the frequency and width of these two peaks fixed, a least-squares routine was used to find the best fit for the ZnO E_2^{high} peak. The fit peaks and their superposition are also shown in Fig. 4.3 and were in good agreement with the collected spectra.

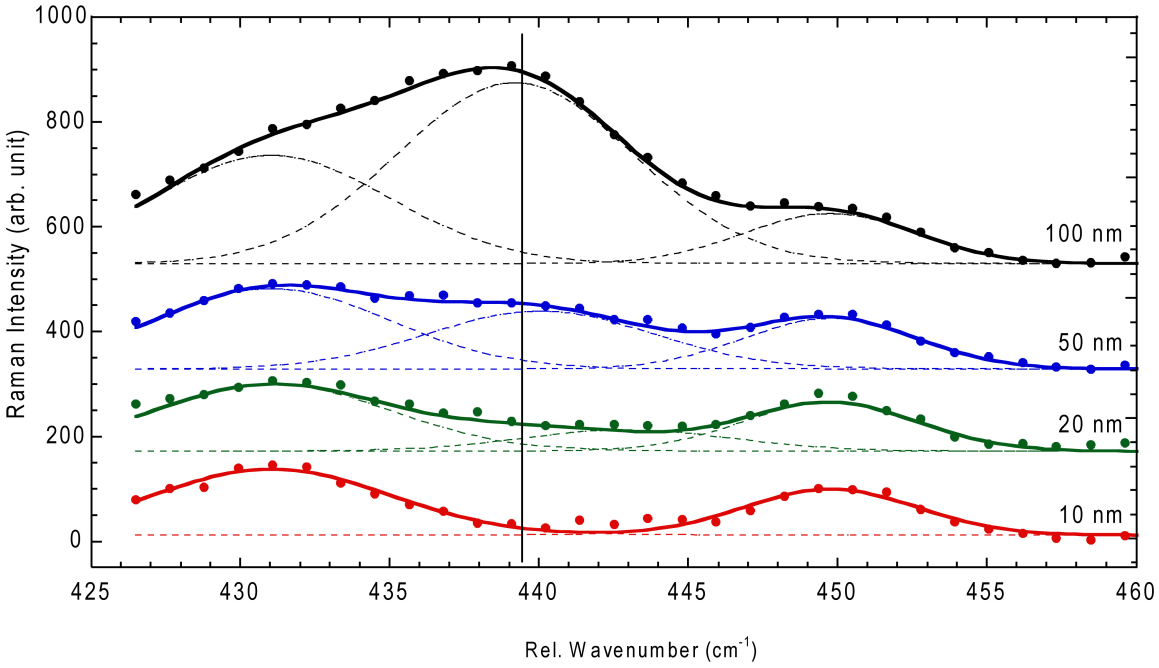

Figure 4.3: Raman spectra of the ZnO thin films on c-plane sapphire substrates. The markers are collected data points and the solid line is the cumulative fit of the fit peaks shown as dashed lines. For clarity the spectra have been offset vertically and the vertical line represents the stress-free position of the E_2^{high} peak [74].

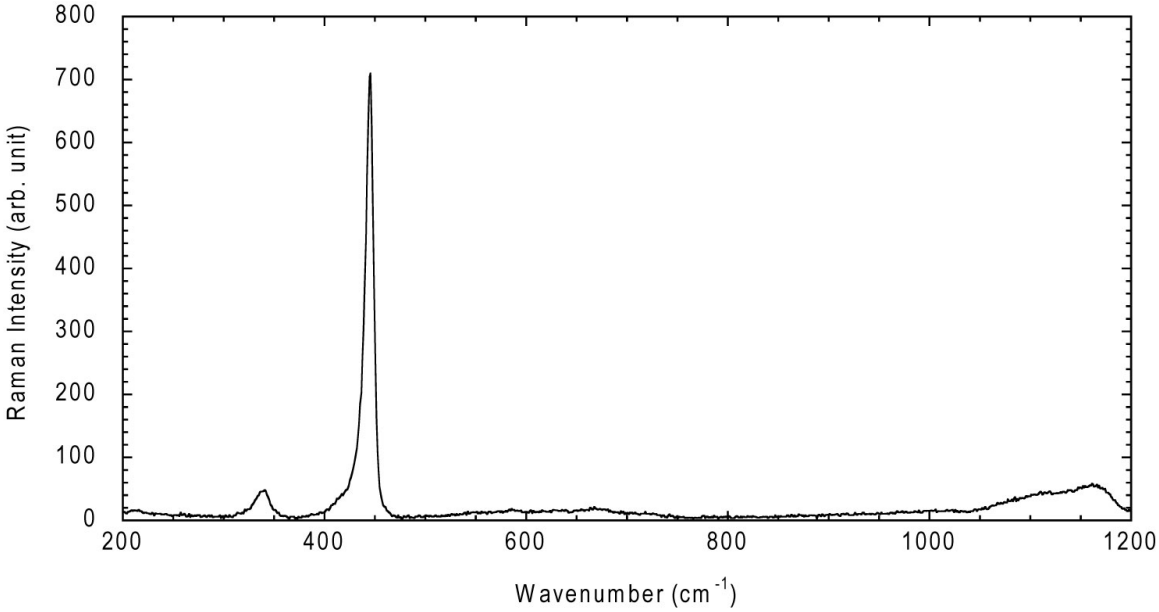

Figure 4.4: Raman spectrum of bulk single crystal ZnO.

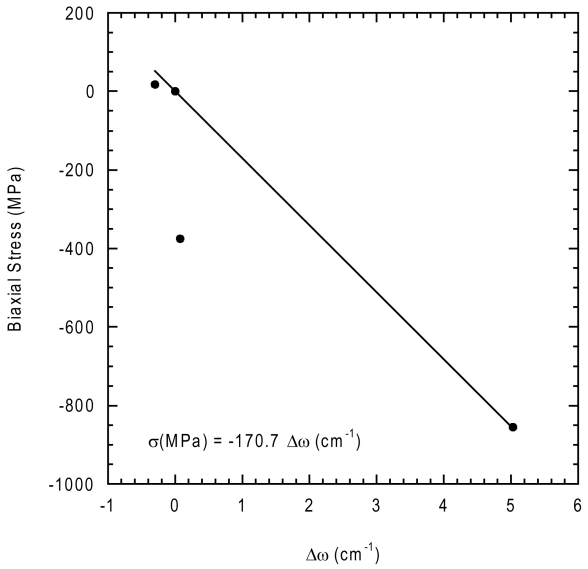

Figure 4.5: Biaxial stress of the ZnO films as a function of the shift in the E_2^{high} peak position from its stress-free position [74].

Figure 4.5 shows the biaxial stress of the films as a function of the E_2^{high} peak frequency shift from its stress-free value. Consistent with reported relationships between applied hydrostatic stress and shifting of the ZnO E_2^{high} Raman mode, a linear fit of the data was performed [68, 77]. The stress and corresponding peak shift were found to be related by $\sigma = -170.7\Delta\omega$, where σ is the stress in MPa and $\Delta\omega$ is the shift of the E_2^{high} frequency from that of the stress-free frequency in cm^{-1}. The value of the obtained slope is in agreement with previous reports from bulk ZnO where Mitra et al. [77] reported an approximate value of -200 MPa/cm^{-1} and Decremps et al. [68] reported an approximate value of -100 MPa/cm^{-1}. The maximum hydrostatic pressure used by Mitra et al. was roughly 1 GPa. Decremps et al. applied a hydrostatic pressure up to approximately 9 GPa, where the wurtzite structure transitioned to a cubic structure. These results indicate that Raman spectroscopy is a useful method for quantifying the biaxial stress of ZnO thin films.

In conclusion, epitaxial ZnO films with different thicknesses from 5 nm to 100 nm were deposited on c-plane sapphire substrates by pulsed laser deposition. XRD measurements indicated that for films $<$ 100 nm in thickness the resulting out-of-plane lattice constants were smaller than that of bulk ZnO. This compressive biaxial stress was relieved with increasing film thickness. Raman spectra from the films exhibited an E_2^{high} peak that shifted to higher frequencies with decreasing thickness or increasing compressive stress. The biaxial stress and change in the E_2^{high} Raman mode frequency are related by a factor of approximately -170 MPa/cm^{-1}, which is in agreement with reported values

in the literature of bulk ZnO under applied hydrostatic stress. These results indicate that instead of using Raman spectroscopy to only qualitatively determine whether the residual stress of ZnO thin films is compressive or tensile as previous studies have done, it can be used to provide a quantitative estimate for the magnitude of the biaxial residual stress of ZnO thin films.

4.1.2 Photoluminescence Response of Films on c-plane Sapphire

Photoluminescence spectroscopy (PL) was performed on several sets of specimens. The first set was the same as that reported for the Raman spectroscopy results in Section 4.1.1. This initial set was created using a laser energy of 3 J/cm^2, the only substrate used was c-plane sapphire, and the nominal film thicknesses ranged from 5 nm to 100 nm. PL experiments were performed at temperatures ranging from 4.2 K to 300 K. The PL response of these films was found to have a very low intensity, which led to changes in the deposition parameters used in subsequent sets. An overview of the results of this first set of specimens follows.

Figures 4.6, 4.7, and 4.8 show PL spectra for 100 nm, 50 nm, and 20 nm thick films, respectively, that were collected at temperatures ranging from 4.2 K to 300 K. There was a monotonic decrease in intensity with increasing temperature for all films. PL emission from the 10 nm and 5 nm thick films was not intense enough to be distinguished from the instrument noise, with the only exception being at temperatures very near 4.2 K. The near-band edge (NBE) emission from all three of these films at 4.2 K was dominated by a single peak located between 3.36 eV and 3.37 eV, which is consistent with the energy of a neutral-donor-bound-exciton (D^0X). With increasing temperature the dominant D^0X emission shifted to lower energies (red shifted) as would be expected [58]. Identification of the main emission peak from the 100 nm thick films as being related to D^0X is further supported by the presence of a shoulder that developed on the higher energy side of the main peak at lower temperatures. The shoulder was centered near 3.377 eV, which is consistent with the position of the free-exciton (FX_A) emission and its presence was not obvious for the films < 100 nm thick.

Figure 4.9 shows PL spectra collected at 4.2 K from all the films plotted together. The relative intensity of the PL emission can be seen in the left plot of Fig. 4.9. The right plot of Fig. 4.9 shows the relative positions of the PL emission for each film by normalizing with respect to the highest observed intensity. With decreasing film thickness the intensity of the NBE emission monotonically decreases. The main NBE emission observed for both the 100 nm and 50 nm thick films was centered near 3.362 eV, while that of the 20 nm and 10 nm thick films were both slightly blue-shifted and centered near 3.370 eV. For the 10 nm thick film a second peak centered near 3.338 eV was also

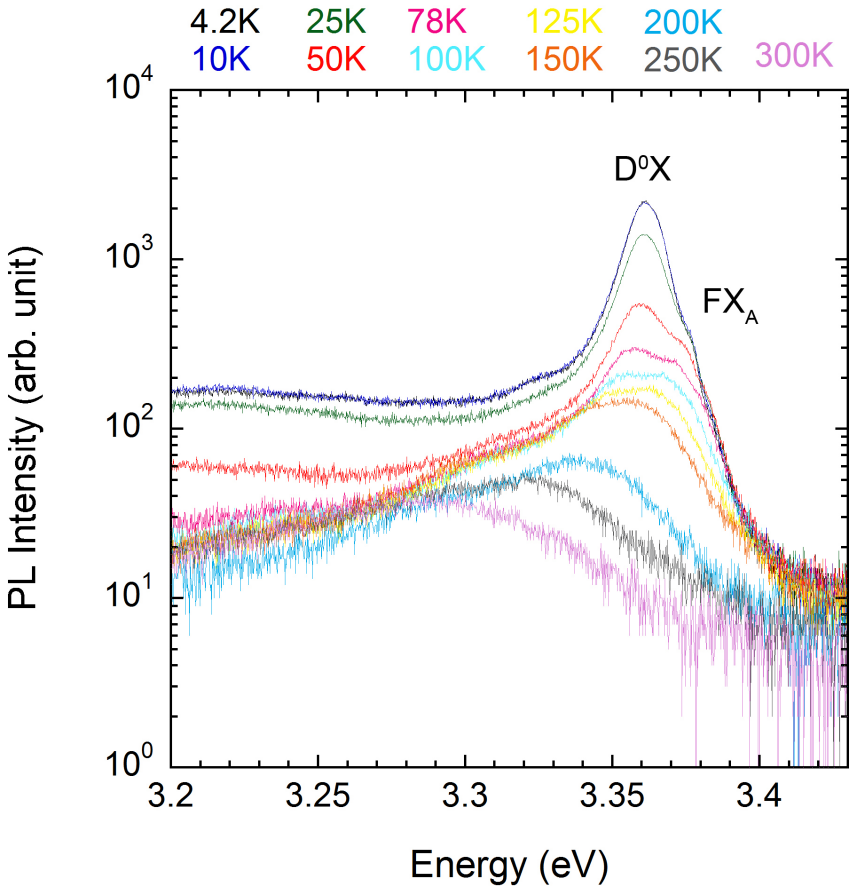

Figure 4.6: PL spectra for the 100 nm thick ZnO film on c-plane sapphire collected at temperatures from 4.2 K to 300 K.

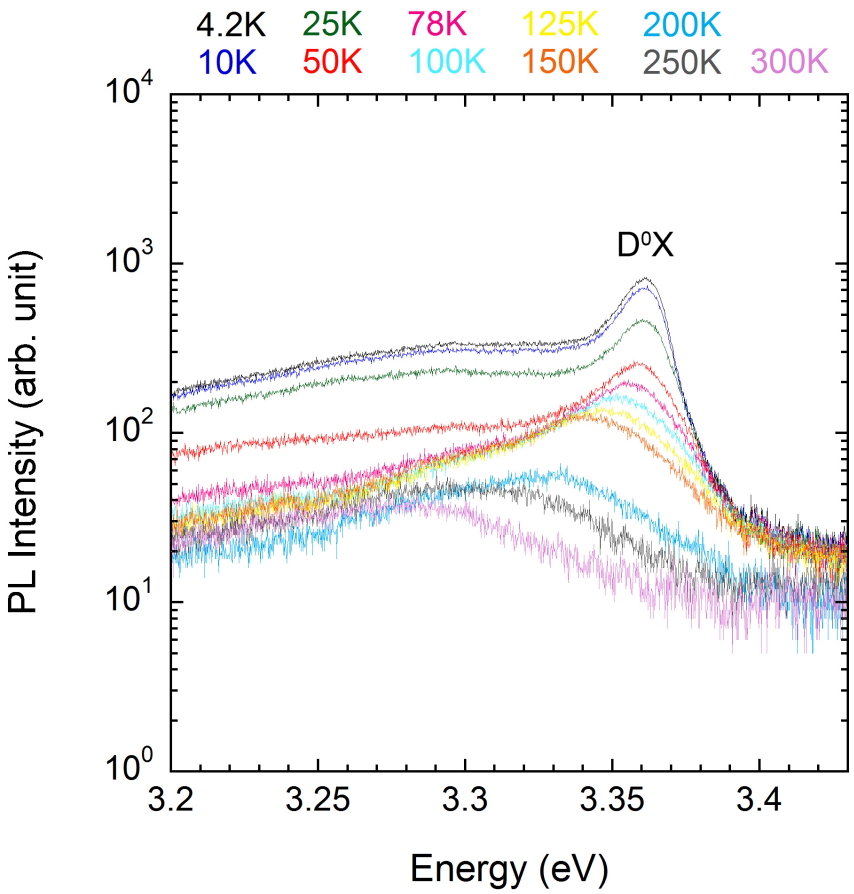

Figure 4.7: PL spectra for the 50 nm thick ZnO film on c-plane sapphire collected at temperatures from 4.2 K to 300 K.

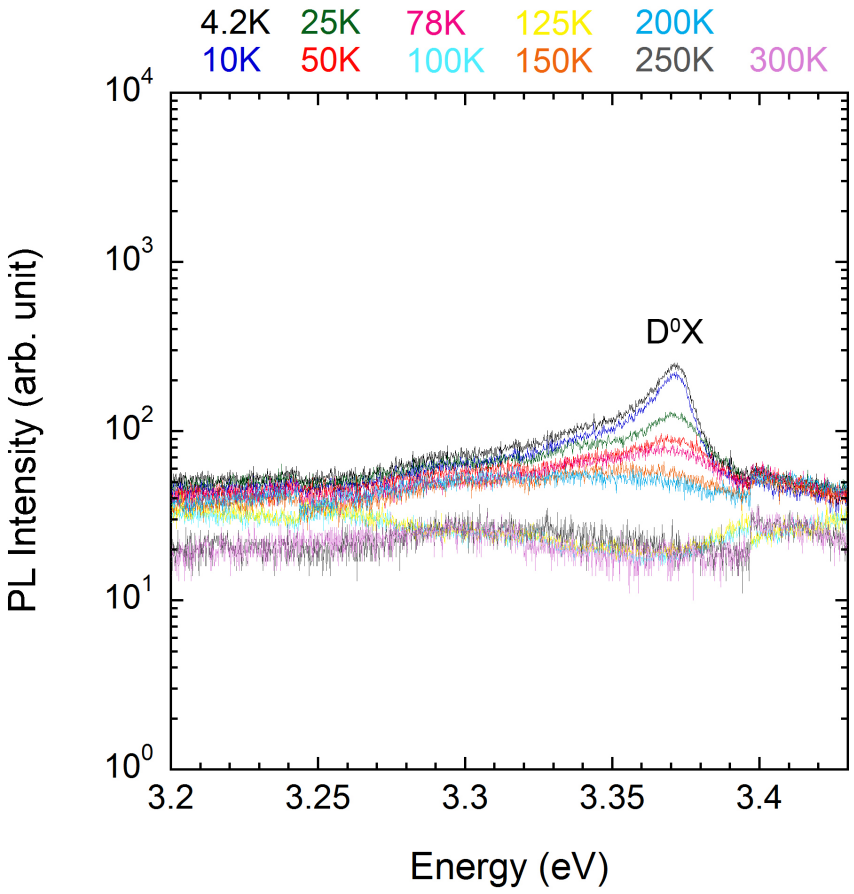

Figure 4.8: PL spectra for the 20 nm thick ZnO film on c-plane sapphire collected at temperatures from 4.2 K to 300 K. The discontinuity near 3.4 eV is an artificat of the monochromator.

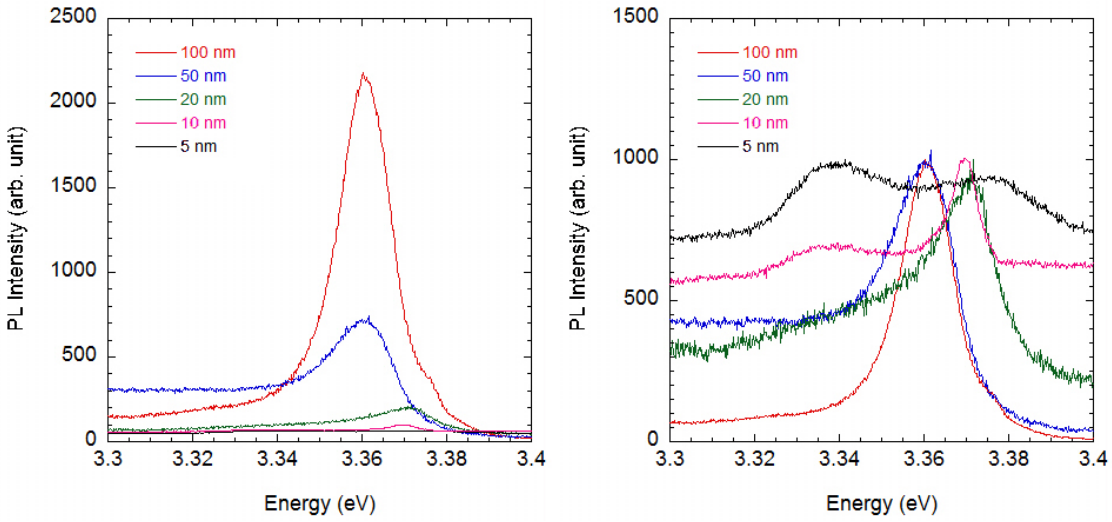

Figure 4.9: PL spectra for 100, 50, 20, 10 and 5 nm thick ZnO films collected at 4.2 K. Left plot is on an absolute intensity scale and the right plot has been normalized to show peak locations.

observed. The origin of this broad, weak peak is likely defect complexes that have been reported in other ZnO thin films and nanostructures [85, 86]. For the 5 nm thick film, the peak centered near 3.338 eV was the most intense emission and the higher energy peak was further blue shifted (near 3.376 eV). Since the position of the higher energy peak from the 5 nm thick film is near that of the FX_A, it is difficult to identify whether this is in fact a D^0X emission blue shifted due to residual strain in the film or if it originates from the FX_A.

For comparison, the PL spectrum of the 100 nm thick film is plotted in Fig. 4.10 along with the PL spectra from chemomechanically polished single crystal bulk ZnO [58] and a 100 nm thick undoped ZnO film that was prepared as part of an investigation into doping ZnO thin films with ReO_2 [87]. No comparison should be made between the absolute intensity of the bulk ZnO PL spectrum and those of the thin films. The ZnO film from the ReO_2 doping study was also deposited on c-plane sapphire by PLD using all of the same parameters, with the one exception being the laser energy. The films from the ReO_2 study used a laser energy of 2 J/cm^2, which results in a slower rate of deposition compared to the films deposited with a laser energy of 3 J/cm^2. The difference observed between the PL emission from the two different films was surprising considering their similarity (e.g., same composition, thickness, substrate, etc.).

The PL peaks from the bulk ZnO centered near 3.36 eV are associated with excitons bound to defect pair complexes that simulate neutral-donors (there were six clearly resolved D^0X peaks), while

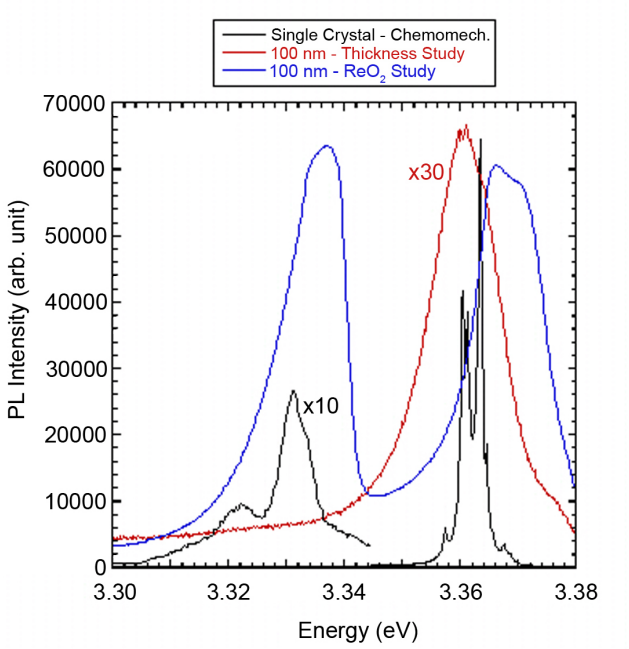

Figure 4.10: PL spectra collected at 4.2 K from chemomechanically polished bulk single crystal ZnO [58], the 100 nm thick ZnO film in the thickness dependence study, and the 100 nm thick 0% ReO_2 ZnO film grown on c-plane sapphire in the ReO_2 study.

those centered near 3.33 eV are associated with two-electron satellites (TES) transitions of neutral-donor-bound-excitons [72]. Not clearly observed from from Fig. 4.10 due to its low intensity relative to the D^0X emission is a free-exciton (FX_A) emission from bulk single crystal ZnO that was centered at 3.378 eV. The ZnO film from the ReO_2 study exhibited PL emission in the same spectral region as the bulk ZnO, but the emission lines were broad and no distinct structure was observed. In the higher energy part of the spectrum there was a broad emission that was composed of two emissions centered near 3.366 eV and 3.371 eV; both emissions were attributed to D^0X. On the higher energy side of the D^0X emissions is a weak shoulder at 3.377 eV related to the FX_A. The lower energy peak near 3.33 eV from the thin film in the ReO_2 study has been observed in a variety of ZnO thin films and nanostructures, and the origin of it has been the center of debate in the literature. Since the 3.33 eV peak has the approximately the same energy as the TES peak found in bulk single crystal ZnO, some have attributed it to a TES related emission [88, 89]. Deep donor-bound excitons [90], as well as acceptor-bound excitons [91] have also been cited as possible sources. Most recent investigations have suggested that the 3.33 eV is related to recombinations involving defects, particularly extended defects often on or near the surface or grain boundaries [85, 86, 92]. Guillemin et al. [86] found that the intensity ratio of the FX_A to the 3.33 eV peak was highly dependent upon

the ZnO particle size in their specimens, which were created by dip coating ZnO nanoparticles on a Si substrate. With decreasing particle size the 3.33 eV peak became much more intense than the FX_A peak. PL emission from the 100 nm thick film in the thickness dependence study was very weak and has been magnified in Fig. 4.10 by a factor of 30. Only a single peak was observed and its position at 3.361 eV was consistent with that of a neutral-donor-bound-exciton (D^0X) emission. The shoulder on the higher energy side of the D^0X peak centered at 3.377 eV is related to FX_A.

Based on the very low intensity of the PL emission from the films compared to that of the undoped film from the ReO_2 study, it was decided to create new films with a range of thicknesses using a lower laser energy.

PL of ZnO Thin Films Deposited with a Lower Laser Energy

Based on the poor PL results from the first set of undoped ZnO thin films deposited on c-plane sapphire, a new set of specimens were created. This set of specimens consisted of undoped ZnO thin films that were created by depositing films with a range of thicknesses on several different substrate materials. The films were deposited by pulsed laser deposition (PLD) using a laser power that was lower than what had been used to create the initial set of undoped specimens used in the Raman spectroscopic investigation in Section 4.1.1 (2 J/cm^2 instead of 3 J/cm^2). The substrates and film thicknesses are summarized in Table 4.1. The r-plane sapphire substrate was investigated to achieve a different amount of residual stress compared to films with the same thickness grown on c-plane sapphire.

Table 4.1: Substrates used for deposition of ZnO and the ZnO thin film thicknesses.

Substrate	**ZnO Film Thickness**
c-plane sapphire	100 nm, 50 nm, 30 nm, 15 nm
r-plane sapphire	200 nm, 100 nm, 50 nm, 30 nm, 15 nm

Photoluminescence experiments were performed on the films created with the lower laser power at temperatures between 4.2 K and 300 K. The PL spectra for the 100 nm film on c-plane sapphire obtained at temperatures from 4.2 K to 300 K are shown in Fig. 4.11. Note the use of a semi-log plot to be able to more easily see the spectra over the whole range of temperatures. With decreasing temperature the PL intensity continuously increased and fine structure in the form of multiple narrow peaks could be observed. Curve fittings using Lorentzian line shapes and a least

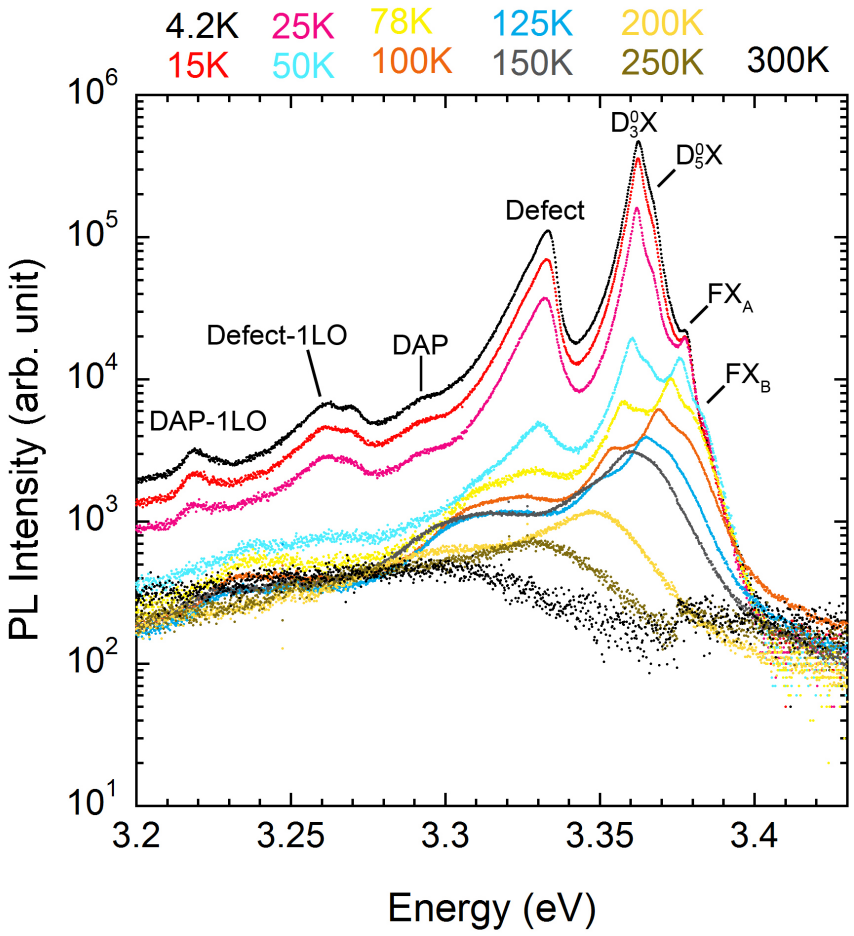

Figure 4.11: PL spectra for a 100 nm thick ZnO film on c-plane sapphire substrate for temperatures ranging from 4.2 K to 300 K (the intensity decreases with increasing temperature).

squares routine were performed on each individual spectrum. At 4.2 K the most intense peak from the 100 nm thick film was centered at 3.3620 eV, which is consistent with the D_3^0X transition [60]. On the high energy side of the D_3^0X peak was a shoulder centered at 3.3665 eV that is consistent with the energy of the D_5^0X transition [60]. The full width at half maximum (FWHM) of the D_3^0X and D_5^0X peaks were approximately 4.4 meV and 3.1 meV, respectively. These FWHWs are larger than the 1 meV that has been reported for high quality, single crystal ZnO [58], but is on the lower side of previously observed values for ZnO thin films [14]. On the high energy side of the donor bound exciton emissions was a peak centered at 3.3776 eV, which is consistent with the position of the FX_A emission. At 4.2 K there was no clear evidence of any higher energy peaks or shoulders other than the FX_A emission.

The second most intense emission from the 100 nm thick film at 4.2 K was centered at 3.3325 eV. Since this has approximately the same energy as the two-electron satellite (TES) peak found in bulk single crystal ZnO, some have attributed such a peak in thin films to a TES related emission [88,89]. Deep donor-bound excitons [90], as well as acceptor-bound excitons [91] have also been cited as possible sources of this emission in thin films. Most recent investigations of ZnO nanostructures and thin films have suggested that the 3.33 eV emission is related to recombinations involving defects, particularly extended defects often near either the surface or grain boundaries [85,86,92]. Guillemin et al. [86] found that the intensity ratio of the FX_A to the 3.33 eV peak was highly dependent upon the ZnO particle size in their specimens, which were created by dip coating ZnO nanoparticles on to a Si substrate. With decreasing particle size the 3.33 eV peak became much more intense than the FX_A peak.

On the lower energy side of the NBE emission, there were weaker peaks centered at 3.2908 eV and 3.2186 eV. The peak at 3.2908 eV is separated from the highest intensity neutral-donor-bound-exciton (D_3^0X) at 3.362 eV by 71 meV. This value is very close to the energy of the longitudinal optical (LO) phonon in ZnO (72 meV). For this reason, Thonke et al. [59] attributed this peak to a phonon replica of the neutral-donor-bound-exciton. However, Hamby [72] noted that there were no previous reports of LO phonons coupling with neutral-donor-bound-excitons and this peak from his high quality single crystal ZnO was asymmetric leading to its identification as a donor acceptor pair (DAP) emission. Due to both the relatively low intensity of this peak from the 100 nm thick film and its location on the low energy tail of the 3.3325 eV defect peak, it is difficult to say if the same asymmetry is also present. Identification of the 3.2908 eV as a DAP consistent with that of Hamby seems reasonable. The energy difference between the 3.2186 eV peak and the 3.2908 eV peak is 72 meV. Identification of this peak as the 1LO phonon assisted DAP transition is also consistent with what Hamby [72] reported for single crystal bulk ZnO.

There were also two closely spaced peaks centered at 3.2686 eV and 3.2586 eV that had similar intensities as those of the DAP emission and its phonon replica. The 3.2586 eV peak is separated by 74 meV from the 3.3325 eV defect emission. This makes the most plausible source of the peak at 3.2586 eV the 1LO phonon replica of the 3.3325 eV defect emission. The origin of the the 3.2686 eV peak has not been identified and no reports of its existence at 4.2 K in undoped ZnO thin films have been found.

With increasing temperature each of the peaks observed at 4.2 K from the 100 nm thick film generally exhibited a continuous decrease in intensity, broadened, and shifted to lower energy. One notable exception to this was the total intensity (product of the peak intensity and FWHM) of

the FX_A, which increased with increasing temperature from 4.2 K to 50 K and then decreased with further increasing temperature. This was also consistent with what Hamby [72] observed for bulk ZnO and was attributed to the thermal dissociation of donor bound excitons that resulted in the creation of a free-exciton and a neutral-donor ($D_X^0 \rightarrow FX + D^0$). The DAP, DAP-1LO, the defect-1LO, and unidentified 3.2686 eV peaks were only observed at temperatures up to 25 K and by 50 K had become indistinguishable from the background. At 50 K there was a new shoulder that developed on the high energy side of the FX_A peak that had an energy of 3.3830 eV. The energy of this shoulder is consistent with the FX_B emission and its observation at 50 K is consistent with what has been reported for bulk ZnO [58]. Analysis of peak positions for temperatures above 150 K became difficult due to the broadening of the emission lines and the thermal dissociation of the donor-bound excitons into free-excitons. Only a single broad peak was found at temperatures of 200 K and above.

Temperature dependence of the energy of selected peaks from the 100 nm thick film on c-plane sapphire is shown in Fig. 4.12. Shown are the peak positions of the FX_B, FX_A, D_5^0X, D_3^0X, and 3.3325 eV defect emission. The FX_A energy at 300 K for single crystal bulk ZnO is also shown in Fig. 4.12 using the symbol (□) and was determined by subtracting the exciton binding energy of ZnO (60 meV) from the room temperature band gap of ZnO (3.37 eV) [58].

Figure 4.13 shows the natural logarithm of the total intensity of the D_3^0X peak for the 100 nm thick film on c-plane sapphire. The thermal activation energy (E_A) of the donor-bound excitons (D_3^0X) was estimated to be 13.3 meV based on a fit of the linear portion of the data. A similar fit of the data for the D_5^0X found an E_A value of approximately 8.8 meV. Based on the energy of six different observed bound-exciton emissions, Hamby [72] concluded that the binding energy of the exciton to the defect-pair complexes ranged from 10 to 20 meV. The most intense of these peaks in chemomechanically polished ZnO was found to have an E_A of 14 meV. Both of the E_A values for the D_3^0X and D_5^0X peaks from the 100 nm thick film on c-plane sapphire are in reasonable agreement with those for single crystal bulk ZnO.

Figure 4.14 shows the PL spectra for the 50 nm thick film on c-plane sapphire. At 4.2 K the FX_A was observable as a shoulder on the most intense emission peak and was centered at 3.3794 eV. This is blue shifted from that of the 100 nm film by 1.8 meV. The most intense peak was the convolution of two emission peaks that were determined by curve fitting to be centered at 3.3641 eV and 3.3565 eV. The energy of these peaks are consistent with neutral-donor-bound-excitons, but are at different energies than the two D^0X emissions observed from the 100 nm thick film. The 3.3641 eV and 3.3565 eV energies are instead consistent with those of the D_4^0X and D_1^0X transitions in bulk

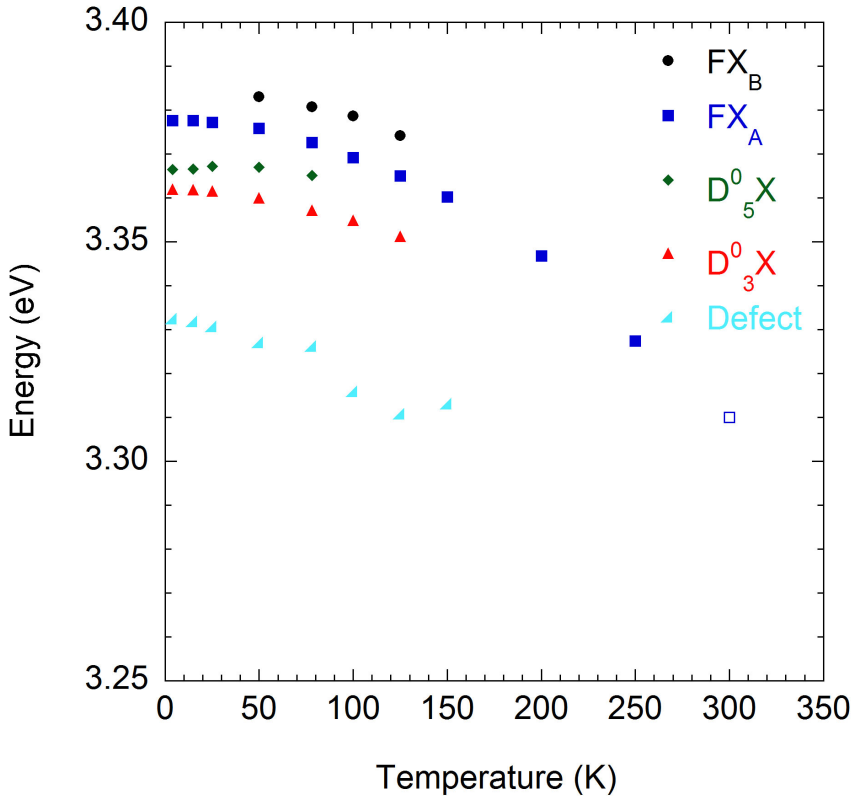

Figure 4.12: Temperature dependent energy of several NBE emissions from the 100 nm thick ZnO film on c-plane sapphire. The 300 K FX_A energy for single crystal bulk ZnO was calculated using the band gap energy of bulk ZnO minus the exciton binding energy of 60 meV and is represented by the open square symbol.

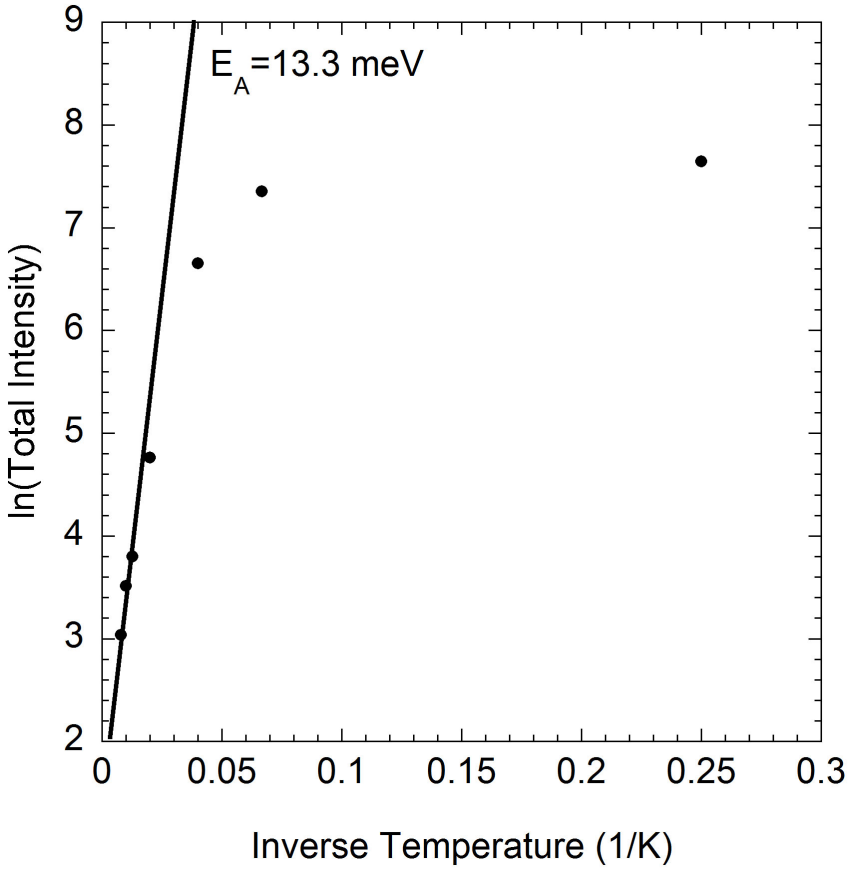

Figure 4.13: Natural logarithm of the total intensity (product of the peak intensity and FWHM) of the D_3^0X peak as a function of inverse temperature.

ZnO, respectively. The fact that the FX_A was blue shifted would be another plausible reason for seeing a shift in the energy of the D^0X emissions. However the two D^0X peaks were not blue shifted by the same 1.8 meV shift of the FX_A compared to those of the 100 nm thick film. The most likely reason for the change in the D^0X energies are the presence of different crystal defects from those in the 100 nm thick film. Additional less intense peaks were observed that were centered at 3.3264 eV, 3.3064 eV and 3.2518 eV. Consistent with the identification of the peaks from the 100 nm thick film, the most likely source of the 3.3264 eV emission is related to extended defects and the 3.2518 eV emission is its 1LO phonon replica. The peak at 3.3064 eV is likely the DAP emission.

As with the 100 nm thick film, the total intensity of the FX_A emission was found to increase with increasing temperature and reached a maximum at 25 K. With further increasing temperature the FX_A total intensity continuously decreased. Temperature dependence of the energy of selected PL peaks from the 50 nm thick film on c-plane sapphire is shown in Fig. 4.15. Shown are the peak positions of the FX_A, D_4^0X, D_1^0X, and 3.3264 eV defect emission. The FX_A energy appears to again approach that of the single crystal bulk ZnO near room temperature.

The peak widths of the D_4^0X and D_1^0X emissions at 4.2 K were 6.2 meV and 10.7 meV, respectively. These FWHM values are roughly twice those of the D^0X emission from the 100 nm thick film. This broadening of the the D^0X peaks points to an increase in damage and dislocations in the 50 nm thick film compared to the 100 nm thick film. Hamby [83] observed that the width of one D^0X peak was 1 meV for a chemomechanically polished single crystal ZnO surface compared to 2.3 meV for a mechanically polished surface.

The estimated thermal activation energy of the D_4^0X emission from the 50 nm thick film was found to be approximately 17.5 meV. This is higher than either of the two D^0X emissions from the 100 nm thick film, but still within the 10 to 20 meV range expected for the binding energy of the exciton to the defect-pair complexes in bulk ZnO. The relatively small temperature range over which the D_1^0X emission was observed made it difficult to estimate the E_A for it.

Figure 4.16 shows the PL spectra for the 30 nm thick films on c-plane sapphire. Much of the fine structure found in the thicker films is not observed; at low temperature there are three distinct broad peaks centered at 3.3562 eV, 3.3141 eV, and 3.2488 eV. The 3.3562 eV peak has approximately the same energy as the D_1^0X emission in bulk ZnO. The FWHM of the D_1^0X peak was 13.8 meV, which is broader than the D^0X emissions from the 50 nm thick film indicating additional crystal defects and disorder. The thermal activation energy of the D_3^0X was approximately 8.1 meV, which still falls within the anticipated range of binding energies of neutral-donor-bound-excitons. No evidence of FX_A emission in the form of a shoulder on the higher energy side of the D^0X emission was observed.

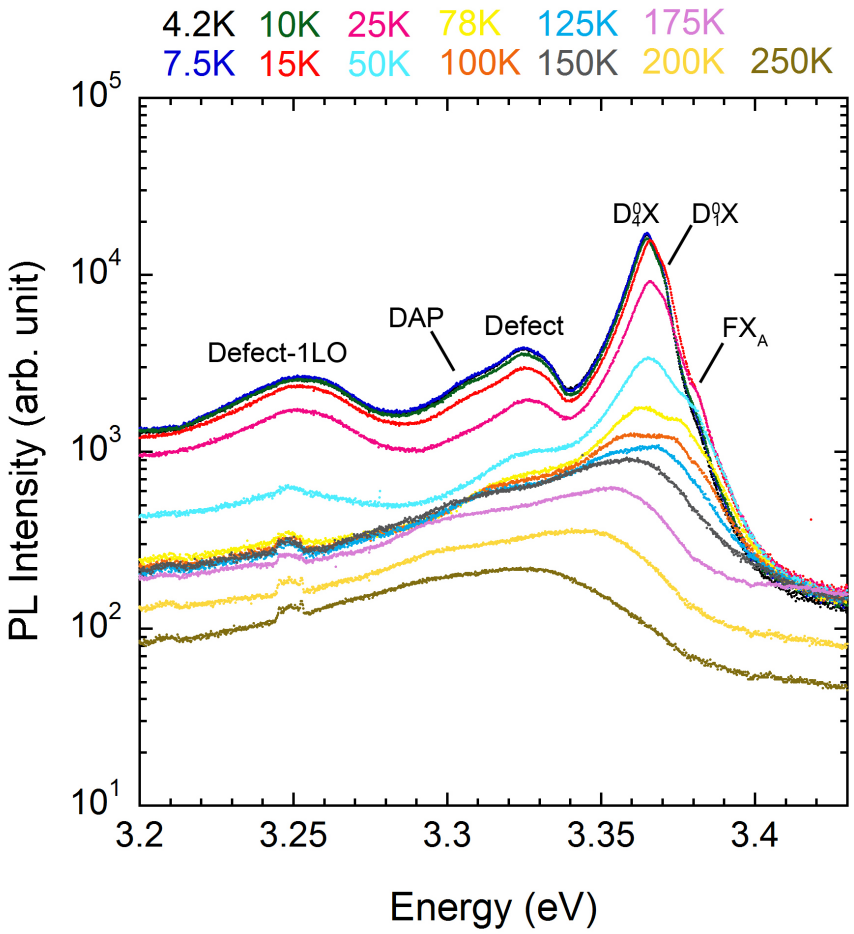

Figure 4.14: PL spectra for a 50 nm thick ZnO film on c-plane sapphire substrate for temperatures ranging from 4.2 K to 300 K (the intensity decreases with increasing temperature). The slight discontinuity near 3.25 eV at the higher temperatures is not a real peak but is an artifact of the spectrometer.

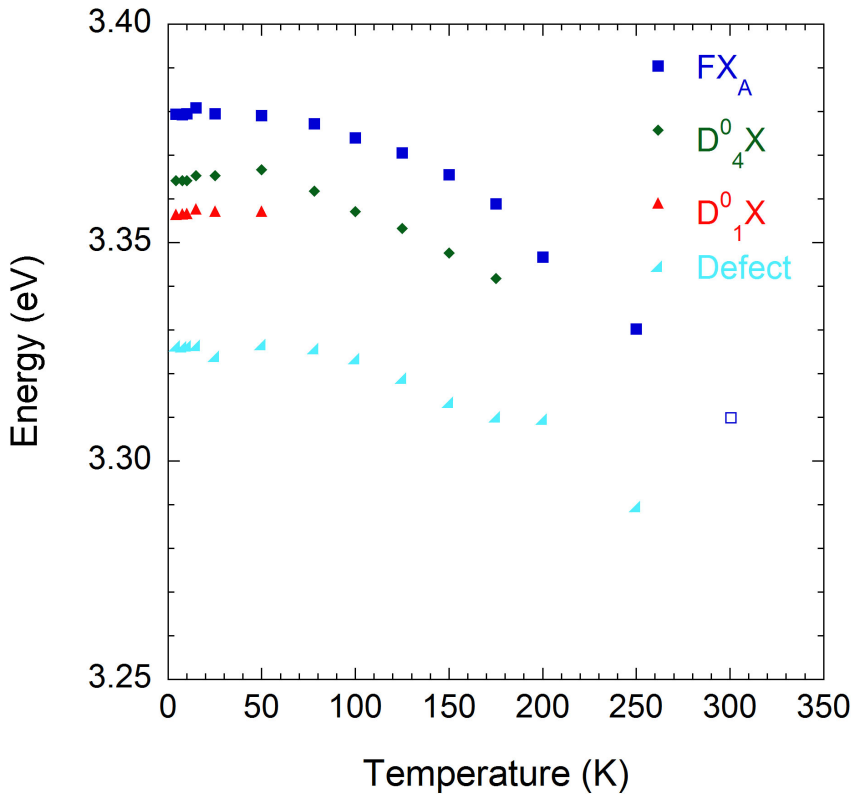

Figure 4.15: Temperature dependent energy of several NBE emissions from the 50 nm thick ZnO film on c-plane sapphire. The 300 K FX_A energy for single crystal bulk ZnO was calculated using the band gap energy of bulk ZnO minus the exciton binding energy of 60 meV and is represented by the open square symbol.

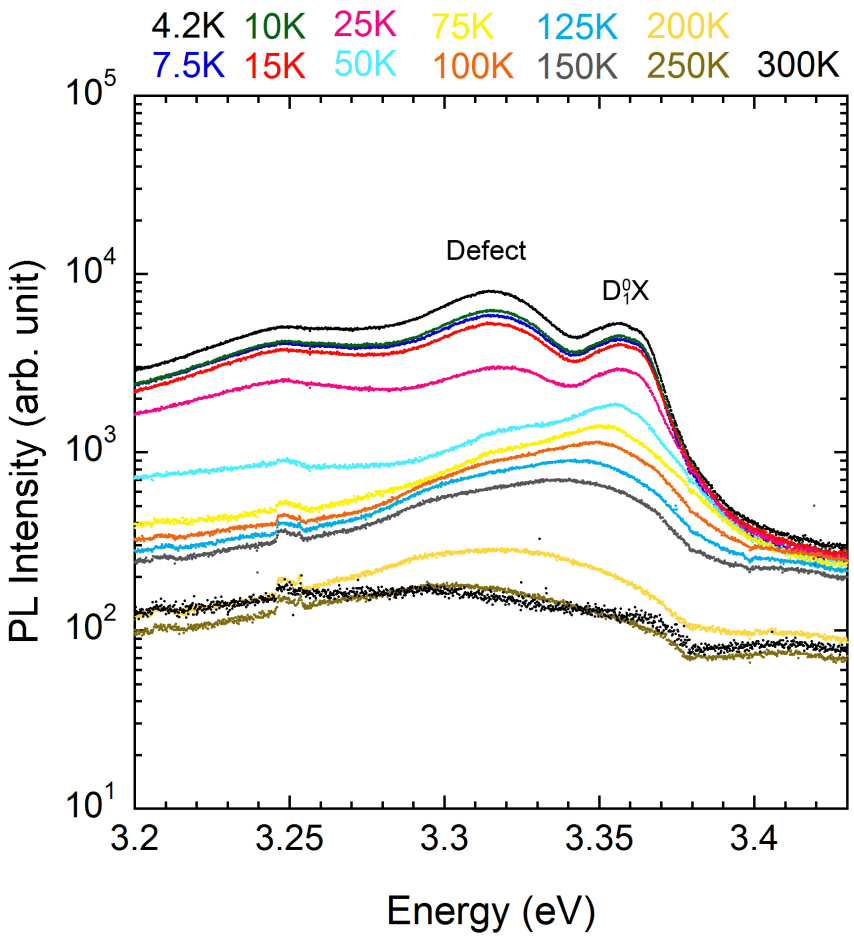

Figure 4.16: PL spectra for a 30 nm thick ZnO film on c-plane sapphire substrate for temperatures ranging from 4.2 K to 300 K (the intensity decreases with increasing temperature). The slight discontinuity near 3.25 eV at the higher temperatures is not a real peak but is an artifact of the monochromator.

The shape of the peak at 3.3141 eV appears to be consistent the extended defect peak that was centered at 3.3325 eV for the 100 nm thick film and at 3.3264 eV for the 50 nm thick film. With a 65.8 meV difference between the energy of the 3.2488 eV peak and the extended defect peak, it is unlikely this is the 1LO phonon replica of the defect emission, but may instead be a DAP related emission.

As shown in Fig. 4.17, the only distinct feature in the PL spectrum collected at 4.2 K from the 15 nm thick film was a very weak peak centered at 3.3624 eV with a FWHM of 13.7 meV. This peak width is the same as the neutral-donor-bound-exciton emission from the 30 nm thick film. There was also a broad background signal from 3.33 eV extending to lower energies, but the lack of any

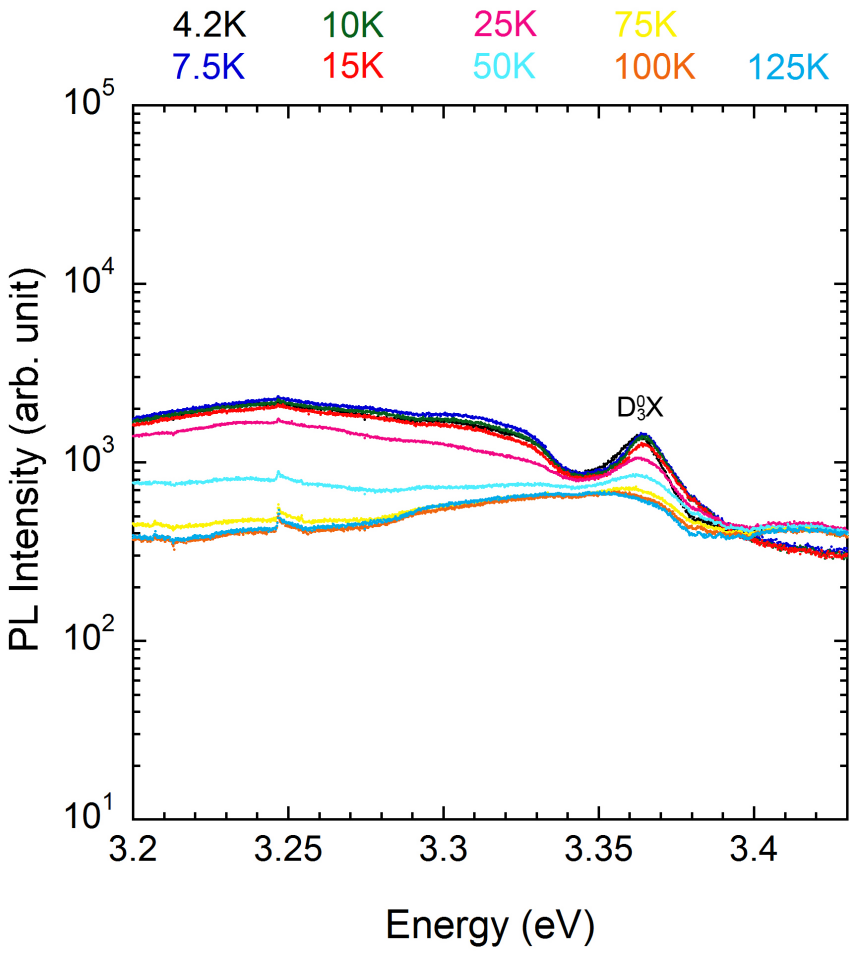

Figure 4.17: PL spectra for a 15 nm thick ZnO film on c-plane sapphire substrate for temperatures ranging from 4.2 K to 100 K (the intensity decreases with increasing temperature). The slight discontinuity near 3.25 eV at the higher temperatures is not a real peak but is an artifact of the monochromator.

distinct structure made fitting impossible. There was no clear evidence of any shoulders on the high energy side of the 3.3624 eV peak. With increasing temperature, the peak at 3.3624 eV decreased in intensity and was no longer clearly distinguishable from the background for temperatures above 100 K. The spectral position and temperature dependent behavior are consistent with a neutral-donor-bound emission. The energy of the peak is consistent with that of the D^0_3X in bulk ZnO [57].

With decreasing ZnO film thickness on c-plane sapphire the residual stress of the films as measured by XRD and Raman spectroscopy became more compressive (see Sec. 4.1.1). Based on previous reports on the effect of residual strain and stress in ZnO, the higher compressive stress should have resulted in an increase in the band gap and consequently a blue shifting of the NBE PL emis-

sion [93–95]. However, there was no consistent evidence of this blue shift. There are a number of reasons for this. The lack of an observable free-exciton emission from the 30 nm and 15 nm thick films, where the stress was the highest magnitude and the expected blue shift would be largest, made a direct measurement of changes in the magnitude of the band gap as a function of residual stress not possible. With the absence of FX_A emission from all the films, the use of D^0X energies would be another option to investigate the effect of residual stress on the band gap. The large number of D^0X related emissions reported for ZnO in a relatively small spectral region makes it difficult to know if the observed change in energy of the D^0X emission as a function of film thickness is a result of a change in the band gap, or simply a difference in the type of defects within the films.

4.1.3 Photoluminescence Response of Films on r-plane Sapphire

HR-TEM images (not shown but similar images are shown for doped films in Sec. 4.2) indicated that the resulting films had a sharp interface between the film and the substrate and were highly epitaxial with respect to the r-plane sapphire substrates as evidenced by the selected electron diffraction pattern. From both the XRD analysis and the electron diffraction pattern, the epitaxial relationship between the film and the substrate can be described as $(11\bar{2}0)_{\mathrm{ZnO}}||(01\bar{1}2)_{\mathrm{sapphire}}$ and $[0001]_{\mathrm{ZnO}}||[0\bar{1}11]_{\mathrm{sapphire}}$, which is consistent with previous reports [14]. The resulting films are non-polar, a-plane ZnO.

In comparison to the 100 nm thick film on the c-plane sapphire, the 200 nm thick film on r-plane sapphire exhibited a less intense PL emission and a much different spectrum, as shown in Fig. 4.18. The PL spectra for the 200 nm film on r-plane sapphire obtained at temperatures from 4.2 K to 300 K are shown in Fig. 4.19. At 4.2 K there was a distinct peak centered at 3.3767 eV that is attributed to the FX_A. This assignment is consistent with that of an emission of the same energy from single crystal a-plane ZnO by Hwang and Um [96] and a-plane ZnO films by Han et al. [97]. There have been several other studies [98, 99] that have assigned a similarly shaped peak with a slightly higher energy (∼3.385 eV) to a neutral-donor-bound-exciton with a localization energy of 34 meV. Additional higher energy peaks were also observed in those studies and assigned to the free-exciton transitions. In the current study, no peaks or shoulders were observed at 4.2 K with a higher energy than 3.3767 eV. Estimating the binding energy (localization energy) of the 3.3767 eV emission using a fit of the initial linear portion of the natural logarithm of the total intensity as a function inverse temperature yielded E_A =18 meV. A potential source of the difference between the current study, Han et al. [97], and Hwang and Um [96] compared to that of Koida et al. [98] and

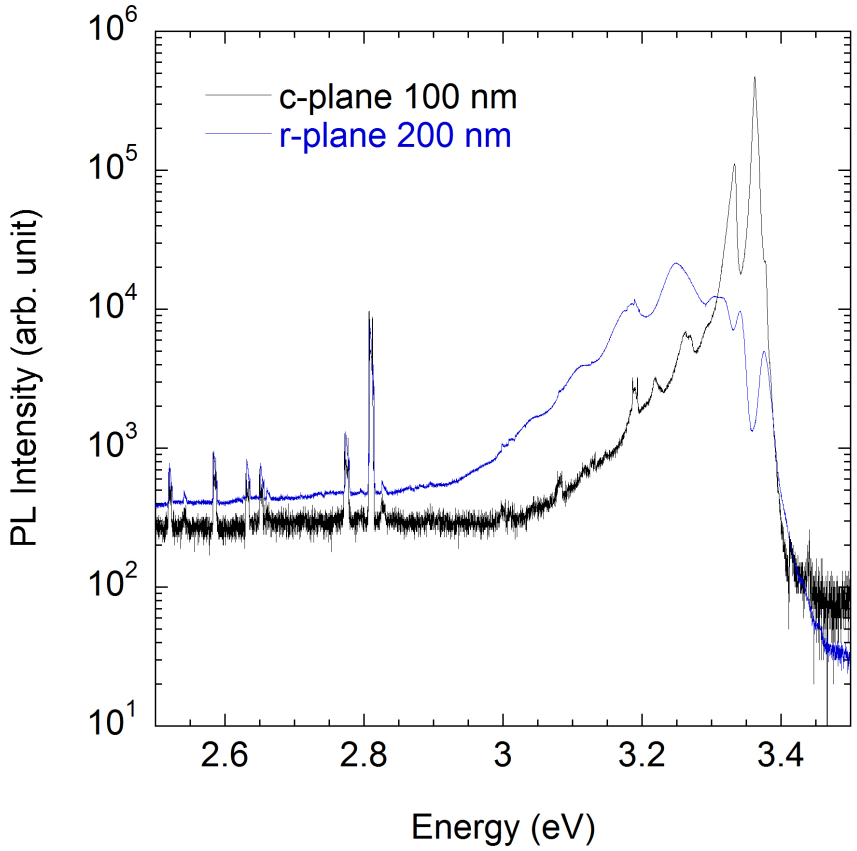

Figure 4.18: Comparison between the PL spectrum of the 200 nm thick film on r-plane sapphire at 4.2 K to that of the 100 nm thick film on c-plane sapphire. The narrow peaks centered < 2.8 eV are not from the specimens but are instead laser lines.

Nam el al. [99] is a difference in the residual stress of the a-plane ZnO. A higher magnitude residual stress would result in increasing the band gap and thus blue shifting of the PL emissions. In strain free a-plane ZnO the free-exciton emission should be in agreement with that of c-plane ZnO.

Additional PL peaks were also observed at 4.2 K centered at 3.3408 eV, 3.3199 eV, 3.3056 eV, 3.2470 eV, 3.1759 eV and 3.1098 eV. Since the peak at 3.3056 eV is 71 meV from the FX_A, it is attributed to the 1LO-replica of the FX_A. The FX_A-1LO peak was only distinguishable from other emissions in Fig. 4.19 up to 25 K. The 3.3408 eV peak is a neutral-donor-bound-exciton related emission. For a-plane ZnO, Han et al. [97] observed a D^0X emission centered 3.351 eV and Hwang and Um [96] observed a D^0X emission centered 3.360 eV. The width of the D^0X peak in the current study was $\sim$10 meV. This is about half the FWHM reported by Han et al. for the D^0X in a-plane ZnO, but was roughly two to three times larger than the D^0X emission reported above for c-plane ZnO. This broadening is expected since ZnO films on r-plane sapphire tend to have poorer quality

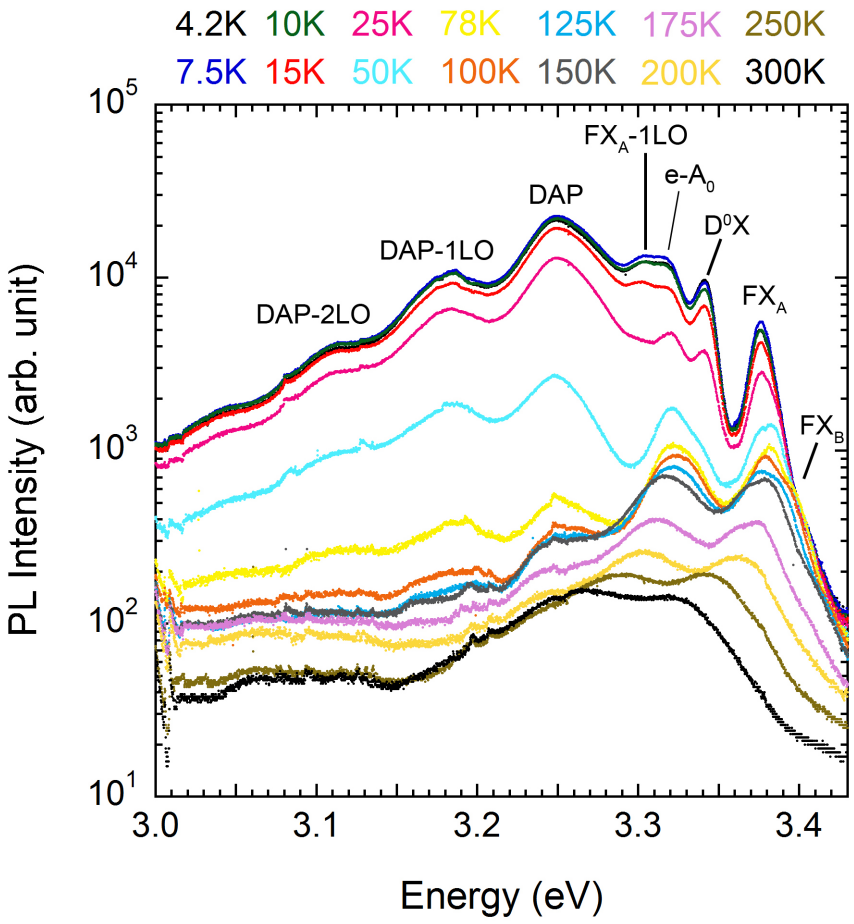

Figure 4.19: PL spectra for a 200 nm thick ZnO film on r-plane sapphire substrate for temperatures ranging from 4.2 K to 300 K (the intensity decreases with increasing temperature).

than those on c-plane sapphire.

The PL peak at 3.3199 eV shown in Fig. 4.19 is attributed to the recombination of a free-electron to bound-acceptor ($e - A_0$). Schirra et al. [100] determined this particular emission was the result of an electron in the conduction band that recombines with a hole that is bound to an acceptor state created by basal plane stacking faults. The PL peaks at 3.2470 eV and 3.1759 eV are spaced from the $e - A_0$ peak by 72 meV and 144 meV, respectively. This would justify the assignment of the first-order and second-order LO-phonon replicas of the $e - A_0$ (($e - A_0$)-1LO and ($e - A_0$)-2LO) to the peaks at 3.2470 eV and 3.1759 eV, respectively, however the intensity of the the peak at 3.2470 eV is higher than that of the $e - A_0$ emission. Therefore the peak at 3.2470 eV is attributed to a DAP emission and the peak at 3.1759 eV is its first order LO-phonon replica. The source of the PL peak at 3.1098 eV is a less clear, but might be the result of the second-order LO-phonon replica of the DAP emission (DAP-2LO). It is centered 138 meV from the DAP emission, which is close to expected value of a second-order LO-phonon replica in ZnO (144 meV).

From 78 K to 100 K there is a shoulder at about 3.3950 eV. The most plausible source of this shoulder is the FX_B emission since it has approximately the same energy and was also observed over a similar range of temperatures as the FX_B peak from the 100 nm thick film on c-plane sapphire. No sign of the FX_C emission at 3.419 eV was seen at any temperature [99].

As the temperature increased the peaks at 3.341 eV, 3.319 eV, and 3.304 eV merged into a single peak and were indistinguishable from each other at 50 K. At room temperature there was a broad emission that was clearly composed of at least two peaks centered at approximately 3.325 eV and 3.260 eV. The PL peak positions from the 200 nm thick film as a function of temperature are shown in Fig. 4.20.

Figure 4.21 shows the PL spectra for the 100 nm thick film on r-plane sapphire. Fine structure was more difficult to observe compared to the 200 nm thick film due to apparent peak broadening, but the peak positions and general behavior as a function of temperature was similar. At 4.2 K the FX_A emission had shifted to a slightly lower energy compared to the 200 nm thick film and was located at 3.3702 eV. The only emission that was not clearly observed from the 100 nm thick film was the $FX_A - 1LO$. The energy of the PL emissions as a function of temperature from the 100 nm thick film on r-plane sapphire are shown in Fig. 4.22.

Very little emission was observed from the 50 nm thick film as shown in Fig. 4.23. At the lowest temperatures there was a clear FX_A related peak centered near 3.378 eV, but no other distinct emission was observed. It is possible that there is also an $e - A_0$ emission centered at 3.318 eV, but it is hard to distinguish its presence from the background. At temperatures above 100 K it became

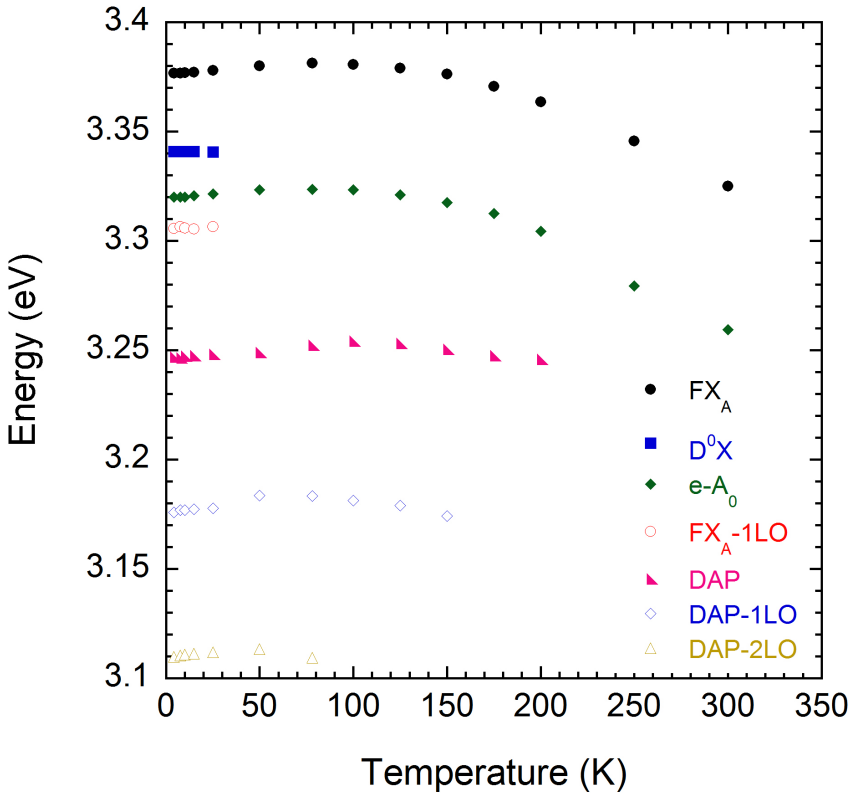

Figure 4.20: Temperature dependent energy of several NBE emissions from the 200 nm thick ZnO film on r-plane sapphire.

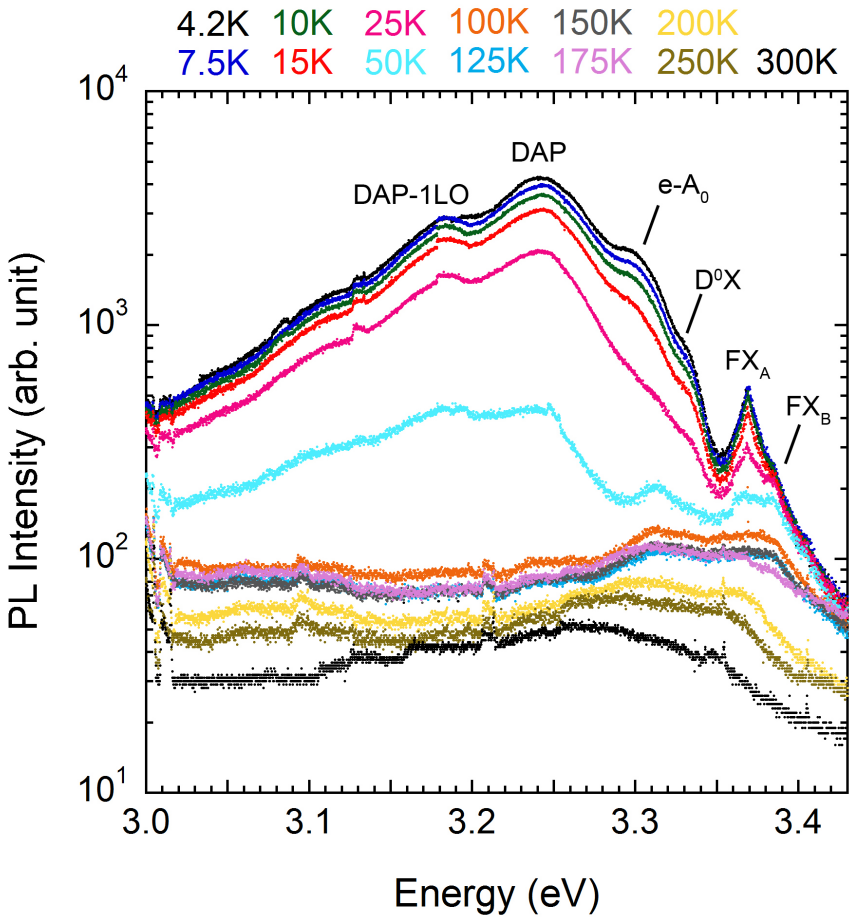

Figure 4.21: PL spectra for a 100 nm thick ZnO film on r-plane sapphire substrate for temperatures ranging from 4.2 K to 300 K (the intensity decreases with increasing temperature).

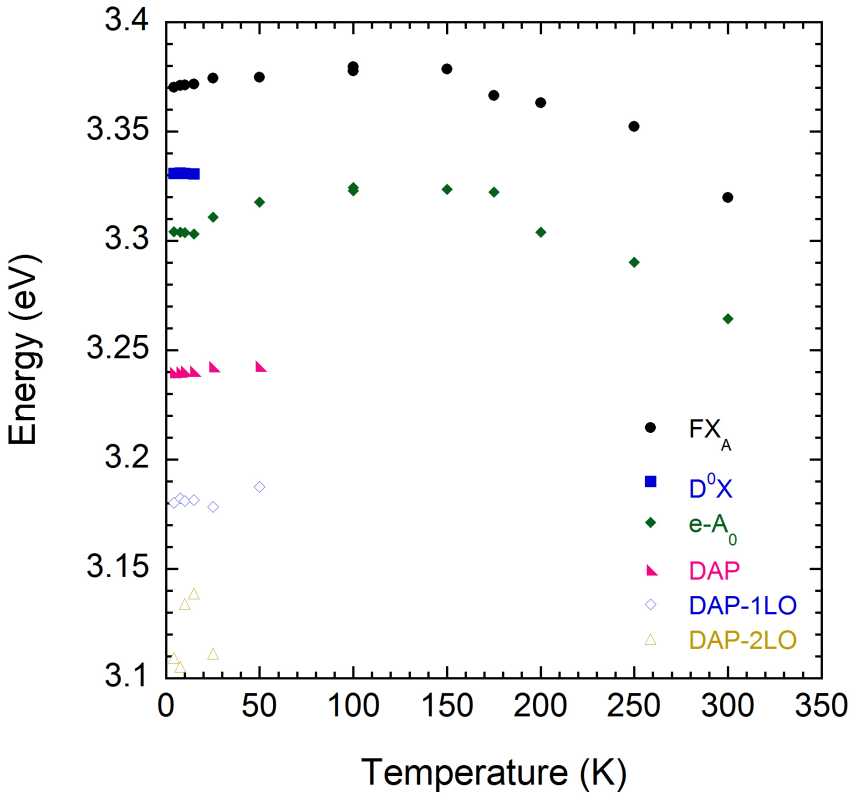

Figure 4.22: Temperature dependent energy of several NBE emissions from the 100 nm thick ZnO film on r-plane sapphire.

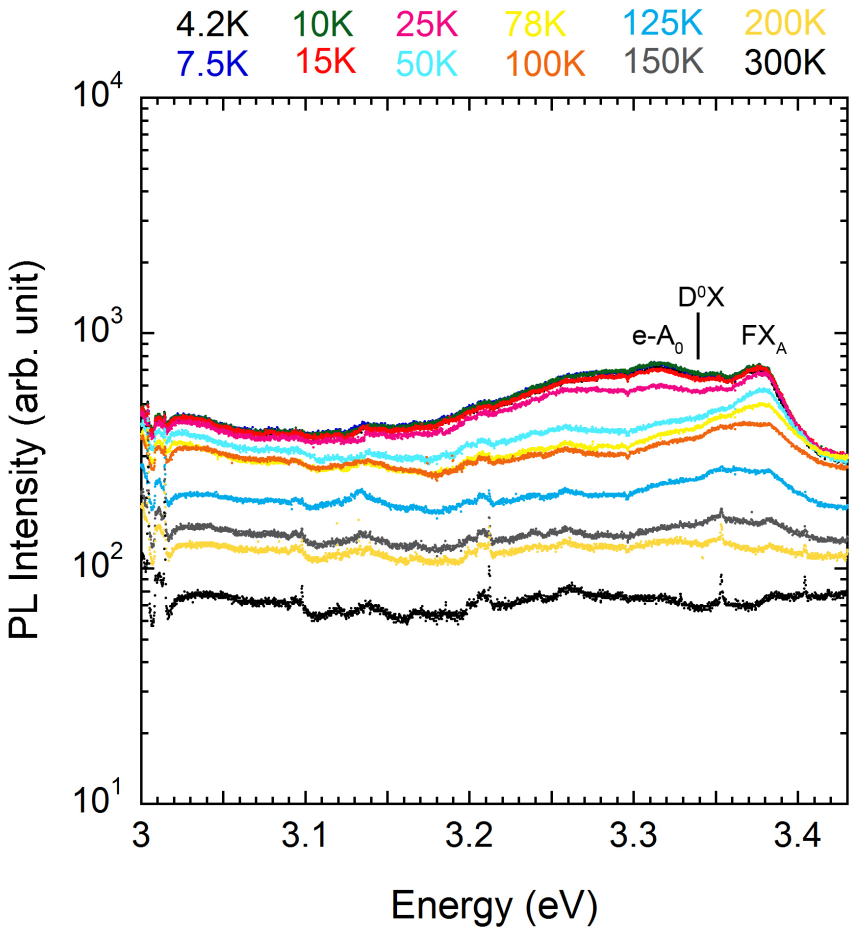

Figure 4.23: PL spectra for a 50 nm thick ZnO film on r-plane sapphire substrate for temperatures ranging from 4.2 K to 300 K (the intensity decreases with increasing temperature).

difficult to identify the presence of the FX_A peak.

A comparison of the spectra collected at 4.2 K for all the films (on both c-plane and r-plane sapphire) is shown in Fig. 4.24 and a summary of the curve fitting results are shown in Table 4.2. There was no clear evidence from the PL results that the residual stress in the films led to any significant shifting of the PL emissions. One trend that was consistent for films on both types of substrate is that the PL emission for the thickest films had the most narrow PL peak widths and they broadened with decreasing film thickness. This indicates that the overall crystal quality improves as the films become thicker. In general the a-plane ZnO films grown on the r-plane sapphire had larger PL peak widths than those of the c-plane ZnO films grown on the c-plane sapphire. This indicates that for a given film thickness, the a-plane ZnO will have more crystal defects than the c-plane ZnO.

Overall, the crystal quality of both the c-plane and a-plane ZnO films in this study have been found to be of very high quality compared to other films reported in the literature.

Table 4.2: Summary of curve fitting results from PL spectra collected at 4.2 K for both c-plane ZnO (c-plane sapphire substrates) and a-plane ZnO (r-plane sapphire substrates) thin films, along with those of bulk single crystal ZnO [57]. Energy values are in eV and FWHM values are in meV.

			FX_A	D_5^0X	D_4^0X	D_3^0X	D_1^0X	D^0X	Defect	$e - A_0$
Bulk		Energy	3.3771	3.3664	3.3650	3.3618	3.3598	-	-	-
c-plane ZnO	100 nm	Energy	3.3776	3.3665	-	3.3620	-	-	3.3325	-
		FWHM	1.3	3.1	-	4.4	-	-	10.8	-
	50 nm	Energy	3.3794	-	3.3641	-	3.3565	-	3.3264	-
		FWHM	5.5	-	6.2	-	10.7	-	20.1	-
	30 nm	Energy	-	-	-	-	3.3562	-	3.3141	-
		FWHM	-	-	-	-	13.8	-	36.0	-
	15 nm	Energy	-	-	-	3.3624	-	-	-	-
		FWHM	-	-	-	13.7	-	-	-	-
a-plane ZnO	200 nm	Energy	3.3767	-	-	-	-	3.3408	-	3.3199
		FWHM	10.7	-	-	-	-	10.2	-	14.6
	100 nm	Energy	3.3702	-	-	-	-	3.3308	-	3.3042
		FWHM	17.5	-	-	-	-	13.1	-	36.4
	50 nm	Energy	3.3780	-	-	-	-	3.3535	-	3.3187
		FWHM	27.4	-	-	-	-	44.2	-	50.7

4.1.4 Debye Temperature

The temperature dependent behavior of the spectral center of the FX_A peak from the 100 nm thick film on c-plane sapphire in the second set of specimens was fit using the Manoogian-Woolley (MW) model [101]

$$E = E_0 + UT^S + V\Theta[\coth(\Theta/2T) - 1]$$

using a least squares routine in a commercial data analysis software (Origin). The first term, E_0, represents the T=0 K band-gap intercept, the second term, UT^S, represents the effect of lattice

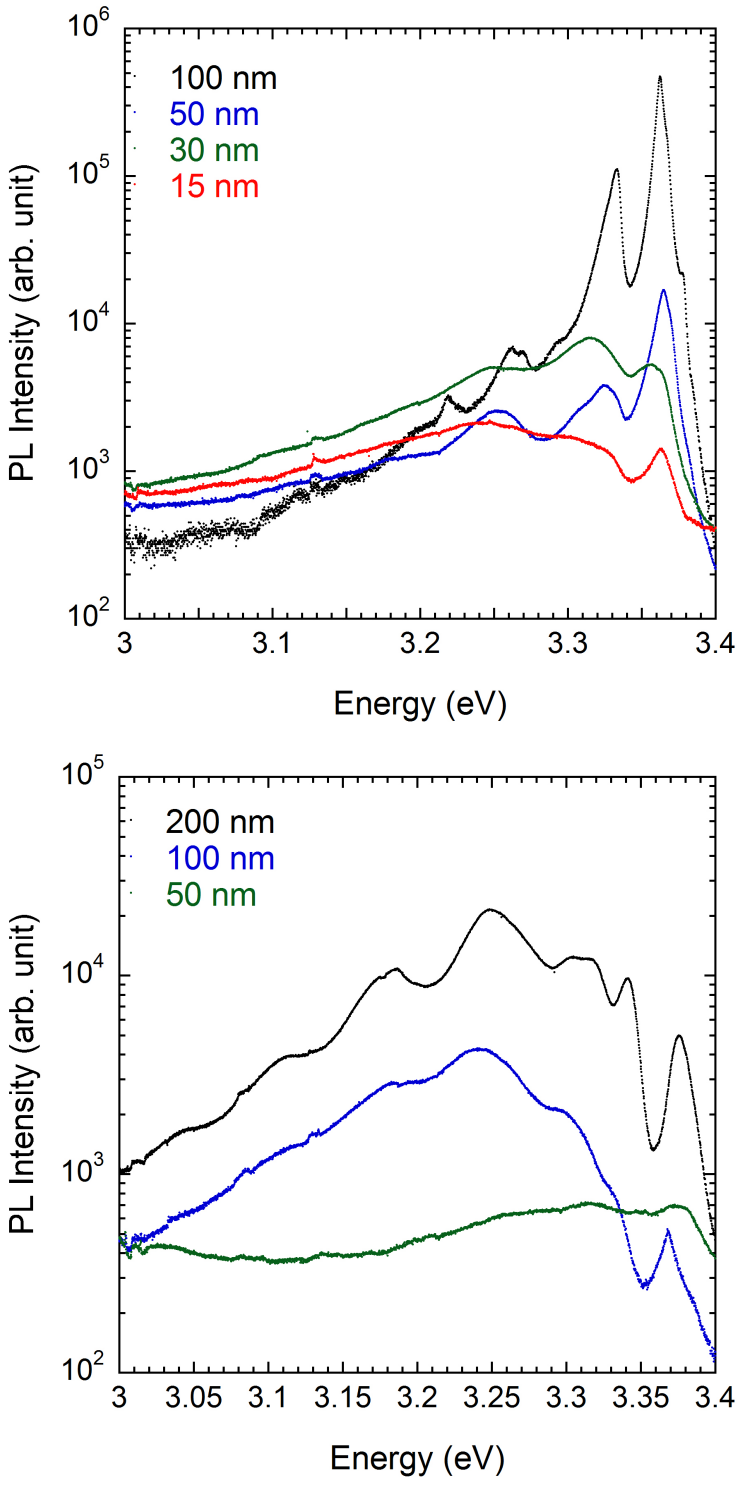

Figure 4.24: PL spectra for all the ZnO films on c-plane sapphire (top) and r-plane sapphire (bottom) collected at 4.2 K.

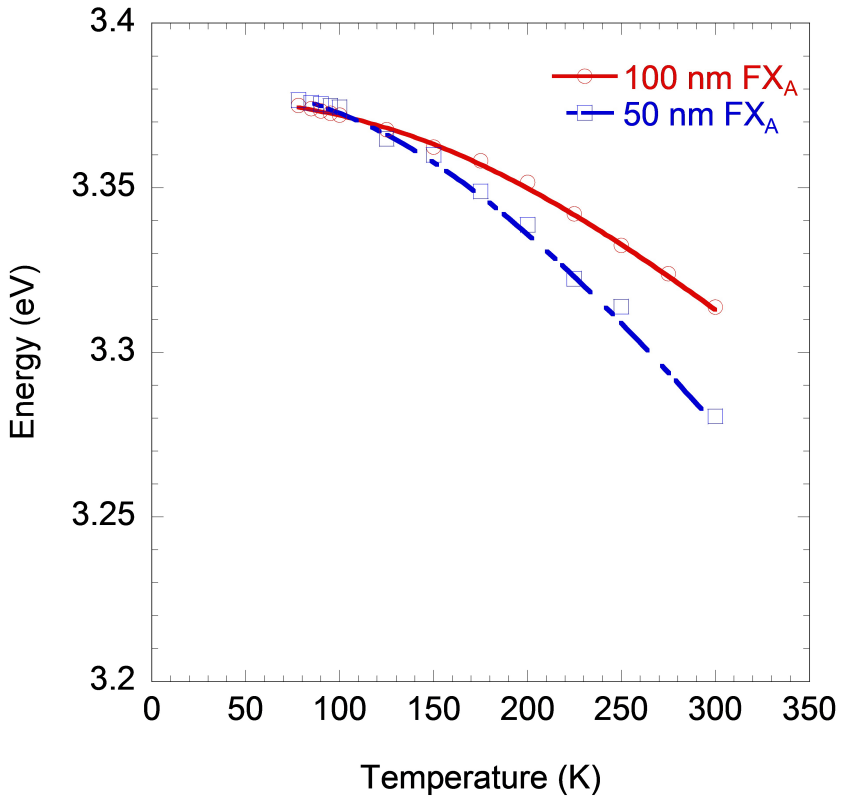

Figure 4.25: MW fittings of the temperature dependent free-exciton peak position for the 100 nm and 50 nm thick films.

dilatation on the band-gap, and the third term, $V\Theta[\coth(\Theta/2T)-1]$, represents the effect of electron-phonon interactions on the band-gap. The coefficients obtained from the fitting were E_0=3.3795 eV, U= 1.1×10^5 eV/K, S=1.41, V=-1.9×10^{-4} eV/K, and Θ=617.3 K. The Debye temperature, Θ_D, can be estimated from the average phonon temperature, Θ, by $\Theta_D = 4\Theta/3$. This gives a Debye temperature of approximately 820 K. This is closer to the reported value of 920 K for ZnO [102] than what Hildebrand observed from a 100 nm thick undoped ZnO thin film (766 K) [87] or Hamby et al. reported for bulk single crystal ZnO (531 K) [58]. The resulting fit of the data is shown in Fig. 4.25.

A fit of the temperature dependent PL data for the 50 nm thick film using the MW model resulted in coefficients of E_0=3.3852 eV, U=1.2×10^5 eV/K, S=1.48, V=-2.4×10^{-4} eV/K, and Θ = 565.7 K. The resulting fit is also shown in Fig. 4.25 and implies a Debye temperature of 754 K. This reduction in the Debye temperature with decreasing film thickness is consistent with what has been observed in polycrystalline Au thin films [103], Cu nanowires [104], and Pt nanowires [105]. Such a decrease has been attributed to phonon softening at the surface, grain boundaries, disorder,

defects, and impurities. A similar analysis was not possible for the 30 nm and 15 nm thick films since the FX_A and D^0X appear as a single peak for all temperatures considered (78 K to 300 K).

A review of the literature for reports of changes in the Debye temperature as a function of film thickness in ZnO indicated that there was no consensus on the Debye temperature of ZnO. Table 4.3 summarizes the most commonly reported values, which range from 305 K to 963 K. When compiling the data, one supposition was that early experimenters may not have been able to create as high quality ZnO as more recently has become available, and thus would tend to report lower Debye temperatures. However, there is not a clear chronological trend. Looking at the types of materials that were investigated (i.e., bulk, thin films, and various nanostructures), all have a wide range of values, suggesting that the physical dimensions of the specimens are not the primary source of the differences.

The exact source of the wide variation in reported Debye temperature is still unclear, but the misuse of the Varshni equation when analyzing the temperature dependence of the PL results may in part explain the variation. The Varshni equation is given by

$$E(T) = E_0 + \alpha T^2/(T + \beta)$$

and relates the band-gap at a given temperature to the the band-gap at 0 K, E_0, and two fitting parameters α and β [118]. The constant β is commonly assumed to be the Debye temperature, although Manoogian and Wooley showed that $\beta = (3/8)\Theta_D$. Good fits of experimental data have been achieved, as long as the material has a low Debye temperature relative to the temperature over which the PL measurements have been performed (commonly $\Theta_D < 300$ K). When the material has a large Debye temperature, poor overall fits of the data are common and β will frequently take on a negative value. Two examples of this are diamond ($\Theta_D = 2220$ K and $\beta = -1437$) and SiC($\Theta_D = 1150$ K and $\beta = -311$) [118]. Part of the reason for this is that the contribution of the lattice dilatation and phonon vibrations on the change in band-gap are lumped together and not accounted for separately. This is one advantage of the MW model, in that these two contributions are considered separately, and all the fitting parameters are independent of temperature.

The biggest disadvantage of the MW is the number of fitting parameters (5) that must be determined. As an example of this, the temperature dependent PL data from Hamby et al. using bulk single crystal ZnO is considered. Table 4.4 shows the fitting parameters and resulting Debye temperatures using several different methods. The theoretical value was found using fixed values of E_0, U, S, and V, with the only fitting parameter being Θ. The Debye temperature was calculated using $\Theta_D = (4/3)\Theta$. Hildebrand used a least square fitting routine that was written in VBA and

used for the analysis of Re doped ZnO thin films [87]. Two commercial data analysis programs were also used for fittings, specifically Origin and Matlab. The fitting of the same data with these different methods resulted in Debye temperatures ranging from 413.33 K to 1080 K, which is about the same variation observed in the literature. A much more extensive set of temperature dependent PL data may be one approach to get more consistent results with the MW model.

In the literature the quality of ZnO (bulk single crystal, thin films, and nanostructured) resulting from a particular synthesis method is regularly implied by the Debye temperature being in agreement with other studies [103–105]. Based on the differences presented here, it becomes clear that such values do not give any insight into the crystal quality between different studies. Other techniques that give an actual measure of crystal quality (e.g., TEM, channeling RBS, etc.) should be considered instead.

4.2 Doped ZnO Thin Films

A set of ReO_2 doped ZnO thin film specimens were created as part of an investigation that was taking place parallel to the initial thickness dependent study of undoped ZnO films. This set is what allowed for the comparison of the PL emission discussed in Section 4.1.2 to films that were created with a lower laser energy. Hildebrand performed both Raman spectroscopy and PL spectroscopy experiments on the films, which contained between 0 wt. % and 50 wt. % ReO_2. All had a nominal thickness of 100 nm [87]. Further analysis of data collected by Hildebrand and complementary characterizations (TEM, XRD, and Hall effect measurements) were subsequently performed and are reported here.

In preliminary investigations leading up to the work of Hildebrand, ZnO doped with Ru, Re, or Ir were created [119]. The overall goal of doping was to improve the electrical properties of ZnO, without having a negative impact on the optical properties. One potential advantage of the three elements that were chosen is that all of their oxides are conductive. This is in contrast to the more common approaches in the literature where Al, Mg, and Cr are used as dopants, all of which form oxides that are electrical insulators. Since PLD growth of ZnO is performed in an O atmosphere, oxidation of the doping elements is a possibility. In the case of doping with Ru, the ZnO took on a dark color and green defect luminescence increased. Doping with Re showed the most promise with carrier concentration relatively unchanged and carrier mobility slightly improved (a net increase in conductivity). The NBE to defect emission ratio also increased. These initial promising results eventually led to the work of Hildebrand and this study.

Cross sectional TEM and HR-TEM measurements performed at CINT showed that the films had a sharp interface with the substrates, as illustrated in Fig. 4.26. They were highly epitaxial with the sapphire substrate as evidenced by the selected area electron diffraction (SAED) patterns also shown in Fig. 4.26. The epitaxial relationship between the film and the c-plane sapphire substrate can be described as $(0001)_{ZnO}||(0001)_{sapphire}$ and $[10\bar{1}0]_{ZnO}||[2\bar{1}\bar{1}0]_{sapphire}$. The epitaxial relationship between the film and the r-plane sapphire substrate can be described as $(11\bar{2}0)_{ZnO}||(01\bar{1}2)_{sapphire}$ and $[0001]_{ZnO}||[0\bar{1}11]_{sapphire}$. Although the SAED patterns showed no evidence of a ReO_2 phase, the HR-TEM image clearly showed that the film with 20 wt. % ReO_2 on c-plane sapphire had alternating aligned columns of ZnO and ReO_2. The widths of the ZnO columns were larger than those of the ReO_2 columns. This columnar structure was not observed from films having concentrations of $ReO_2 < 20$ wt. %. The cross sectional TEM images of films on r-plane sapphire also showed signs of vertically aligned dislocations and grain boundaries. This observation is consistent with the PL spectroscopy results of undoped ZnO films on r-plane sapphire in Sec. 4.1.3 where an $e - A_0$ emission was observed that was attributed to an electron in the conduction band that recombines with a hole that is bound to an acceptor state created by basal plane stacking faults.

X-ray diffraction (XRD) was also performed on the doped ZnO films at CINT. The XRD patterns for the films on c-plane sapphire, shown in Fig. 4.27, consisted of a (002)ZnO peak near 2Θ=34.5°, as well as a $(006)Al_2O_3$ peak near 2Θ=41.8° resulting from the substrate. For the specimen that had 50 wt. % ReO_2 in the film, there was also a very weak $(002)ReO_2$ peak near 2Θ=31.9°. The full width at half maximum (FWHM) of the (002)ZnO rocking curve from the film containing 0 wt. % ReO_2 on c-plane sapphire was 0.45°. With the addition of 5 wt. % ReO_2 the FWHM of the rocking curve decreased to 0.33°, indicating a slight improvement in the overall crystal quality. Further increase in the ReO_2 concentration led to a monotonic increase in the FWHM. For the films on r-plane sapphire, the XRD patterns consisted of a (110)ZnO peak near 2Θ=56.7° and a $(024)Al_2O_3$ peak near 2Θ=52.6°. The FWHM of the ZnO peak for doped films on r-plane sapphire decreased with increasing ReO_2 concentration and reached a minimum at 10 wt. %. The FWHM values for films with 20 wt. % and 50 wt. % ReO_2 were larger than those with lower concentrations. Consistent with the PL spectroscopy results in Secs. 4.1.2 and 4.1.3 that indicated a poorer overall crystal quality in the films deposited on r-plane sapphire, FWHM values for the films on r-plane sapphire substrates were consistently larger than the films with the same ReO_2 concentration on c-plane sapphire.

A more thorough investigation of the PL response was reported by Hildebrand [87], but key observations of the PL response from experiments performed since Hildebrand follows. At 77 K the FX_A emission peak centered near 3.375 eV and FX_B emission peak centered at 3.383 eV were

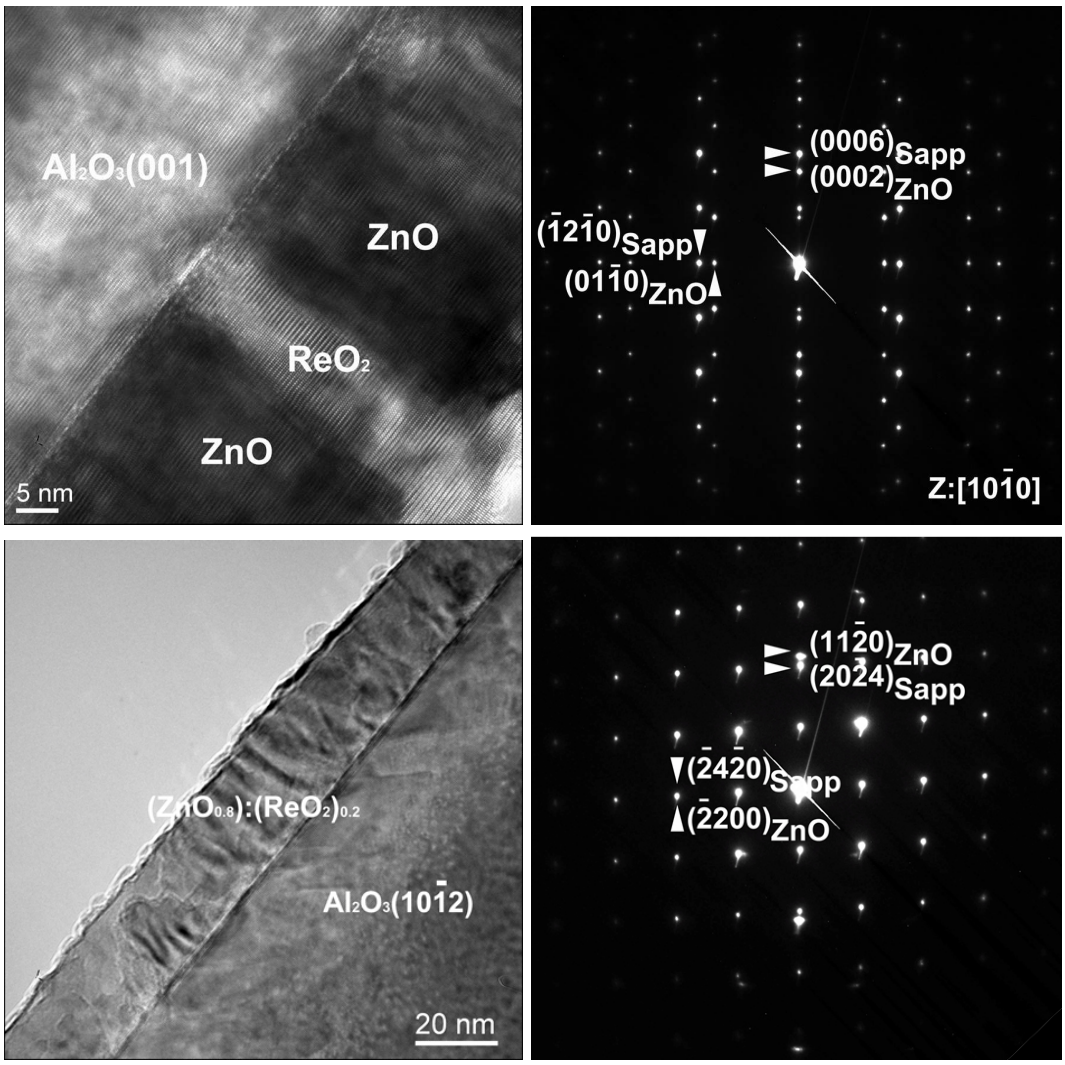

Figure 4.26: HR-TEM image and SAED pattern of the ZnO films with 20 wt. % ReO_2. The figures on top correspond to the film on c-plane sapphire and those on the bottom are from the film on r-plane sapphire.

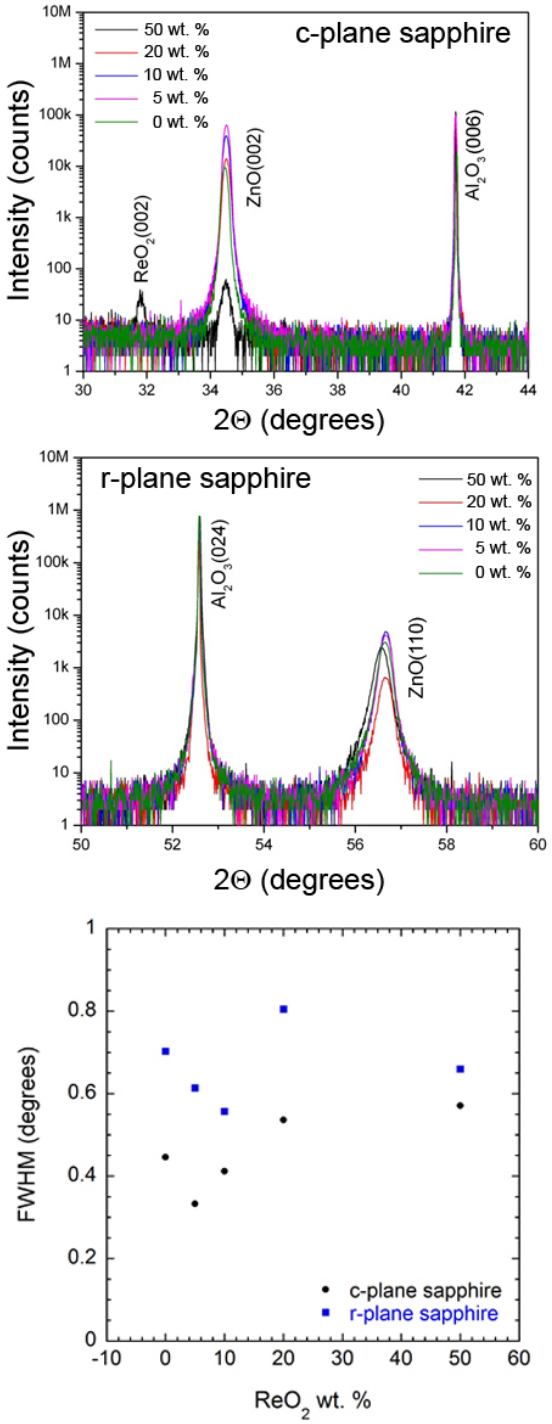

Figure 4.27: XRD patterns and FWHM of rocking curves for ZnO thin films on both c-plane and r-plane sapphire with various concentrations of ReO_2.

observed from all of the films on c-plane sapphire except that with 50 wt. % ReO_2. All the films exhibited a D^0X emission centered near 3.360 eV. With decreasing temperature the FX_B was no longer observed and the intensity of the D^0X emission increased relative to that of the FX_A. Consistent with the approach used by Hamby et al., the Manoogian-Wooley (MW) model was applied to the energy of the FX_A emission peak as a function of temperature in order to estimate the Debye temperature [58]. The Debye temperature of the undoped film was 766 K, which increased to 894 K for the film containing 5 wt. % ReO_2. With further increase in the doping concentration the Debye temperature monotonically decreased with the 10 wt. % and 20 wt. % films having values of 742 K and 557 K, respectively. A decrease in the Debye temperature of thin films has been associated with grain boundaries, defects and impurities, disorder, and surface effects [103–105]. The higher Debye temperature for the film with 5 wt. % ReO_2 may indicate it has higher crystal quality than the other films, which is consistent with what was observed from the FWHM of the (002)ZnO rocking curves in the XRD experiments. As pointed out in Sec. 4.1.4 there are many discrepancies in the literature with regard to the Debye temperature of ZnO and even fitting the same data set with different algorithms can result in a wide range of values. However, a comparison of the Debye temperature between different films that was calculated with the exact same analysis process can provide some insight into potential differences between the films.

At 4.2 K the PL spectra, shown in Fig. 4.28, were dominated by two peaks, an exciton bound to a neutral-donor (D^0X) centered near 3.363 eV and a peak centered near 3.333 eV that has been reported to be associated with the recombination of excitons bound to extended defects [85,86]. The PL spectra in Fig. 4.28 have been normalized with respect to the D^0X peak, so the intensity of the 3.333 eV peak defect can be considered as the intensity ratio of the two peaks. The intensity ratio of the D^0X to defect peak from the film with 5 wt. % ReO_2 was higher than that of the undoped film, implying a reduction in the amount of extended defects that are responsible for the 3.333 eV emission. Further increasing the ReO_2 concentration to 10 wt. % resulted in an increase in the intensity ratio of the D^0X to defect peak, implying the amount of extended defects was only slightly less than the undoped film. This is consistent with the trends that were observed in the XRD and Debye temperature results from these films. For the films with the highest ReO_2 concentrations little to no defect emission peak was observed, which is likely the result of the appearance of a separate ReO_2 in those films.

It is currently unknown how the Re is incorporated into the film at lower ReO_2 concentrations ($\leq$ 10 wt. %). For the film with 50 wt. % ReO_2, XRD experiments indicated the presence of a separate ReO_2 phase in the film. For films with 20 wt. % ReO_2, TEM experiments also suggested

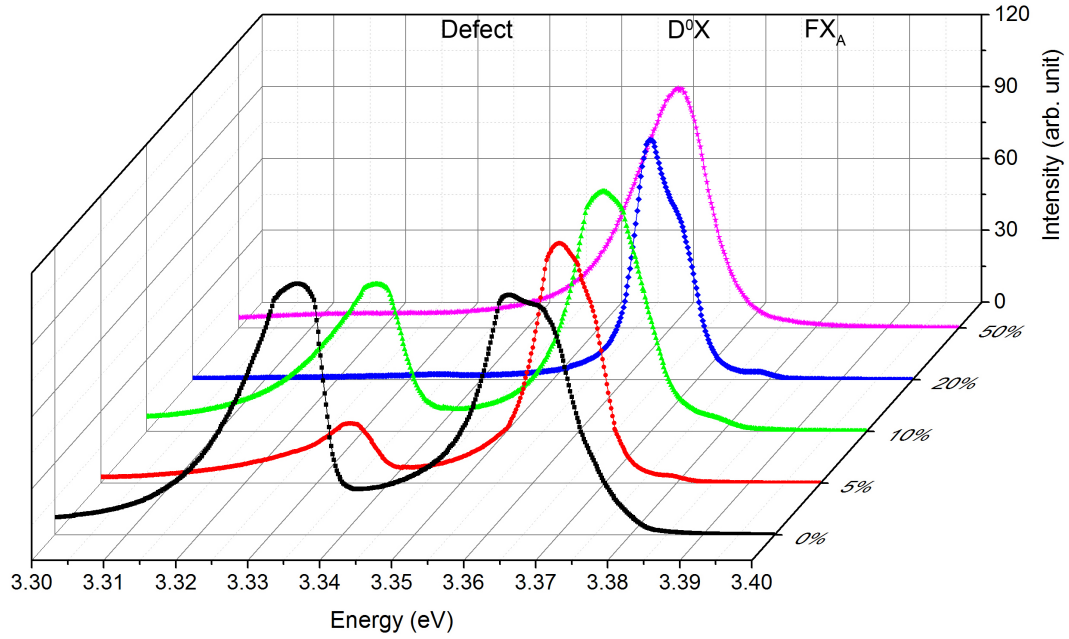

Figure 4.28: PL spectra for the ReO_2 doped ZnO films at 4.2 K.

the presence of a separate ReO_2 phase that appeared as columns. No clear evidence of a ReO_2 phase has been observed for films containing less than 20 wt. % ReO_2. There are several possible reasons for this. The amount and size of any ReO_2 phase may be below the detection limit of the characterization techniques used. Another possibility is that the Re is substituting at Zn sites and no separate ReO_2 phase is present. This would be consistent with the solubility limits of other transition metals (e.g., Ti, V, Cr, Mn, Fe, Co, Ni and Cu) reported by Jin et al. [31], which ranged between 2.5 and 20 mol % depending upon the element. The radius of Re has been reported to be anywhere from 0.52 Å to 0.77 Å depending upon the charge and coordination, which is on the order of or slightly smaller than the radius of tetrahedral Zn^{2+} which is 0.74 Å [120].

Although direct evidence is lacking, the combined results of XRD, Raman spectroscopy, and PL experiments all suggest that Re substitution at Zn sites is likely for ReO_2 concentrations up to 10 wt. %. With the addition of 5 wt. % ReO_2 there was a decrease in the FWHM of the XRD rocking curve compared to the undoped film. Further increasing the ReO_2 concentration to 10 wt. % resulted in FWHM of the XRD rocking curve that was very close to that of the undoped film. This suggests that 5 wt. % ReO_2 improved the overall crystal quality of the film and 10 wt. % ReO_2 did not result in much of a change to the overall crystal quality compared to the undoped

film. Raman spectroscopy experiments performed by Hildebrand indicated that the E_2^{high} ZnO Raman peak shifted to a slightly lower wavenumber for films with 5 wt. % ReO_2 compared to the undoped film, which he reported exhibited a slightly compressive residual stress. The shift of the E_2^{high} Raman peak to a lower wavenumber would indicate the magnitude of the compressive residual stress was slightly relieved. The film with 10 wt. % ReO_2 again shifted to a slightly lower wavenumber indicating a further decrease in the magnitude of the residual stress. The film with 20 wt. % ReO_2 had a E_2^{high} peak position that was shifted to a higher wavenumber than that of the undoped film indicating that the residual stress was more compressive than that of the undoped film. The Debye temperature as determined by the temperature dependent PL response of the films followed a similar trend to the XRD and Raman response. The Debye temperature increased for the film with 5 wt. % ReO_2 compared to the undoped film and the film with 10 wt. % ReO_2 had about the same Debye temperature as the undoped film. Increasing the ReO_2 concentration to 20 wt. % led to a considerable decrease in the Debye temperature. All of these results imply that adding 5 wt. % ReO_2 not only preserves the wurtzite crystal structure, but improves the overall quality of the ZnO films. A further increase of the ReO_2 concentration to 10 wt. % results in films with similar crystal quality as the undoped films. With ReO_2 concentration at or above 20 wt. % there is a pronounced decrease in ZnO crystal quality and the appearance of a distinct ReO_2 phase.

Hall effect measurements were performed at CINT on the ReO_2 doped films. Since conductivity is proportional to the product of the carrier concentration and carrier mobility, the results would provide evidence as to whether the motivation to increase electrical conductivity was achieved. All films were determined to be n-type and the measured carrier concentrations and carrier mobilities, shown in Fig. 4.29, would likely provide additional insight into the effect of ReO_2 concentration on the ZnO crystal quality. For films on c-plane sapphire the addition of 5 wt. % ReO_2 increases both the carrier concentration and mobility compared to the undoped film, which imply an increase in conductivity. The film on c-plane saphire with 10 wt. % ReO_2 showed an increase in carrier mobility but a decrease in carrier concentration. This resulted in a net decrease in the conductivity. With further increase in ReO_2 concentration, the conductivity decreased as a result of decreasing carrier concentration and/or decreasing carrier mobility. For films on r-plane sapphire the carrier concentration decreased for the film with 5 wt. % ReO_2 compared to the undoped film and then increased with increasing ReO_2 concentration. The carrier mobility increased for both the film with 5 wt. % and 10 wt. % ReO_2 and then decreased with increasing ReO_2 concentration. This implies that the film with 10 wt. % ReO_2 had the highest conductivity of the films on r-plane sapphire.

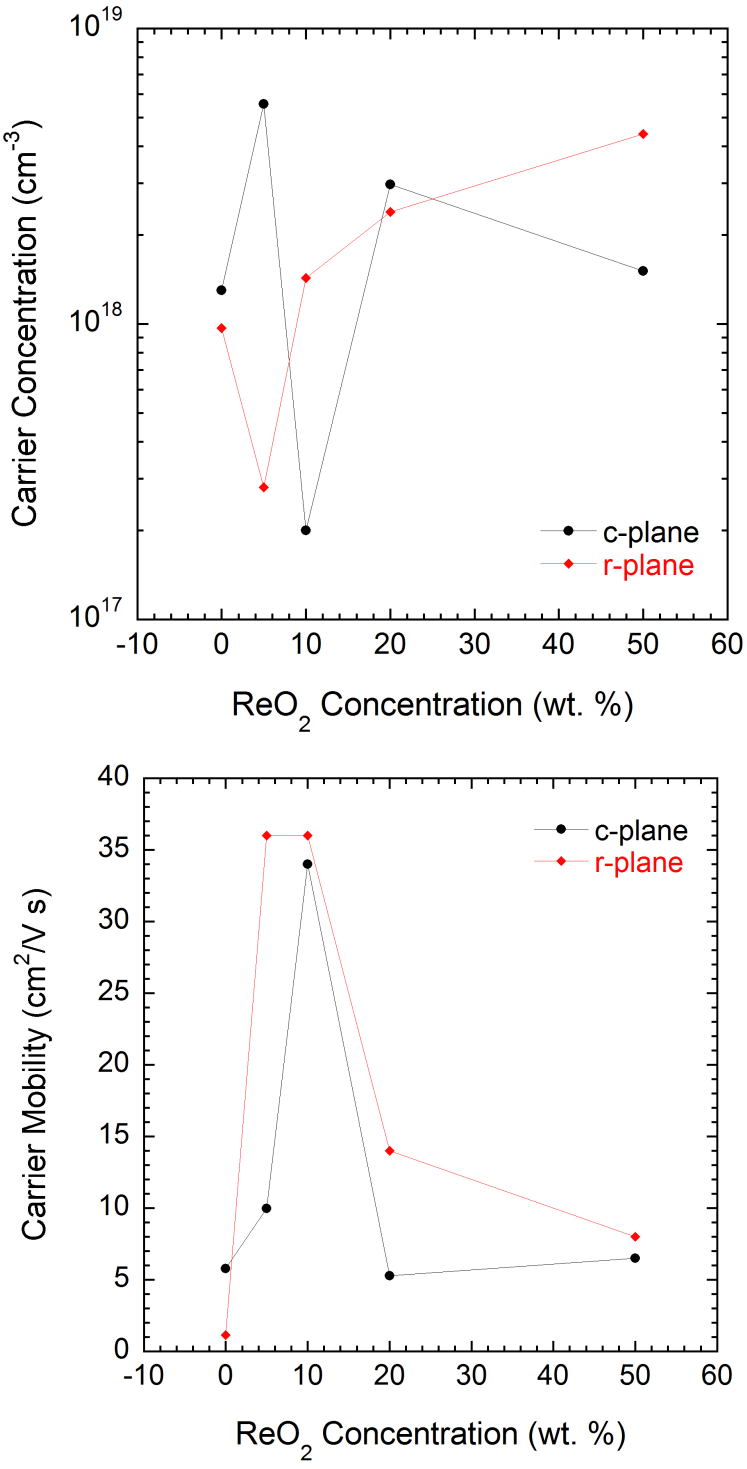

Figure 4.29: Carrier concentration and carrier mobility as measured by Hall effect experiments for ReO_2 doped ZnO films. The lines are guides for the eye.

The theoretical room temperature electron mobility of ZnO is 300 cm^2/V s [121], while experimental results on high quality bulk single crystals are as high as 205 cm^2/V s [122]. For thin films the electron mobility is much less than for single crystals (< 100 cm^2/V s) and is often dependent upon the specific deposition conditions [123]. Carrier concentrations are higher in ZnO films than in bulk single crystal (10^{17} cm^{-3} compared to 10^{15} cm^{-3}) as a result of crystal defects [123].

Table 4.3: Debye temperatures reported in the literature for different types of ZnO with a variety of methods.

Debye Temp.(K)	**Method**	**Material**	**Year**	**Source**
963	PL (Varshni)	Films 200 nm to 2.25 μm via ALD	2009	[106]
920	Hall mobility?	?	1959	[102]
> 800	EXAFS	?	1994	[107]
700	PL (Varshni)	Bulk single cyrstal from Eagle-Picher	2003	[108]
531	PL (MW)	Bulk single crystals	2003	[58]
505	PL (MW)	Nanorods with diameter of 300 to 1000 nm via PLD	2009	[109]
477	PL (Varshni)	Nanoblades/nanoflowers via ultrasonic pyrolysis	2005	[110]
420	PL (Varshni)	Bulk, hydrothermal growth, mechanical polish and HNO_3 etch	2004	[111]
416	Mean sound velocity	Velocity calculated from reported elastic constants	1966	[112]
377	PL (Varshni)	Films 2μm thick on sapphire via MOCVD	2006	[113]
370	XRD	Bulk	1969	[114]
355	Electron diffraction	Crystallites via a zinc arc	1935	[115]
355	Cited [115]	–	1940	[116]
305	PL (modified Varshni)	Bulk	2001	[117]

Table 4.4: Fitting PL data as a function of temperature from Hamby et al. [58] with the MW model using several different methods.

	Hamby [58]	**Theoretical**	**Hildebrand [87]**	**Origin**	**Matlab**
$\mathbf{E_0}$ **(eV)**	3.379	3.379	3.378	3.378	3.38
U (eV/K)	-5.04×10^{-5}	-5.50×10^{-5}	-1.04×10^{-5}	-2.57×10^{-6}	-6.35×10^{-5}
S	1.01	1.00	1.38	1.75	1.06
V (eV/K)	-1.84×10^{-4}	-8.00×10^{-4}	-2.02×10^{-4}	-1.07×10^{-4}	-2.22×10^{-4}
Θ (K)	398	310	575	810	578
$\mathbf{\Theta_D}$ **(K)**	530.67	413.33	766.67	1080	770.67
Sum of Squares Error ($\mathbf{meV^2}$)	5.56	56175	86634	5.27	15.33

Chapter 5

CONCLUSIONS AND FUTURE WORK

The optical response of undoped ZnO thin films deposited on c-plane and r-plane sapphire has been investigated by Raman spectroscopy and photoluminescence (PL) spectroscopy. By varying the film thickness and substrate used for the film deposition, the effects of residual stress, crystallographic orientation of the resulting film, and overall crystal quality were probed. Doped ZnO films were also investigated with a combination of transmission electron microscopy (TEM), x-ray diffraction (XRD), and Hall effect measurements to extend the previous work of Hildebrand [87]. These studies included the effects of ReO_2 concentrations from 0 wt. % to 50 wt. %.

5.1 Conclusions

1. XRD measurements indicated that for films < 100 nm in thickness deposited on c-plane sapphire with a laser energy of 3 J/cm^2, the resulting out-of-plane lattice constants were smaller than that of bulk ZnO. To estimate the residual stress, a biaxial state of stress was assumed and elastic stiffness constants reported in the literature were used. With increasing film thickness the compressive residual stress was relieved until the 100 nm thick film was nominally stress free. Raman spectra from the films exhibited an E_2^{high} peak that shifted to lower frequencies with increasing film thickness (decreasing magnitude of compressive stress). The stress and corresponding E_2^{high} peak shift were found to be related by $\sigma = -170.7\Delta\omega$, which is consistent with reported relationships for bulk ZnO under applied hydrostatic pressure. These results indicate that instead of using Raman spectroscopy to only qualitatively determine whether the

residual stress of ZnO thin films is compressive or tensile as previous studies have done, it can be used to provide a quantitative estimate for the magnitude of the biaxial residual stress of ZnO thin films.

2. All films were found to be highly epitaxial with the substrate. For c-plane sapphire substrates, the epitaxial relationship between the film and substrate can be described as $(0001)_{\mathrm{ZnO}}||(0001)_{\mathrm{sapphire}}$ and $[10\bar{1}0]_{\mathrm{ZnO}}||[2\bar{1}\bar{1}0]_{\mathrm{sapphire}}$. This resulted in c-plane ZnO films that are polar. For the r-plane sapphire substrates, the epitaxial relationship between the film and substrate can be described as $(11\bar{2}0)_{\mathrm{ZnO}}||(01\bar{1}2)_{\mathrm{sapphire}}$ and $[0001]_{\mathrm{ZnO}}||[0\bar{1}11]_{\mathrm{sapphire}}$. This resulted in a-plane ZnO films that are non-polar.

3. Temperature dependent PL experiments from 4.2 K to 300 K for undoped ZnO films deposited on c-plane sapphire with a laser energy of 3 J/cm^2 showed that they exhibited a very weak emission intensity and little to no fine structure in the PL spectra was observable. By reducing the deposition laser energy to 2 J/cm^2 (a lower deposition rate) the films deposited on c-plane showed strong NBE emission with fine structure including emission related to free-excitons, neutral-donor-bound-excitons, defects, a donor acceptor pair, and also phonon replicas of emissions.

4. Differences in the specific type of neutral-donor-bound-excitons were observed from the films on c-plane sapphire, but all had activation energies that were consistent with bulk single crystal ZnO. The variation in the specific type of neutral-donor-bound-exciton observed from each film could be explained by differences in the types of defects present within each film.

5. No consistent evidence of an increase in the ZnO band gap as a result of compressive stress in the films was observed from the PL spectra for films on c-plane sapphire. The lack of an observable free-exciton emission from the 30 nm and 15 nm thick films, where the stress was the highest magnitude and the expected blueshift would be largest, made a direct measurement of changes in the magnitude of the band gap as a function of residual stress not possible. With the absence of $\mathrm{FX_A}$ emission from several films, $\mathrm{D^0X}$ energies could be used to investigate the effect of residual stress on the band gap. The large number of $\mathrm{D^0X}$ related emissions reported for ZnO in a relatively small spectral region made it difficult to confirm if the observed change in energy of the $\mathrm{D^0X}$ emission as a function of film thickness was a result of a change in the band gap, or simply a difference in the type of defects within the films.

6. Temperature dependent PL experiments from 4.2 K to 300 K for undoped ZnO films deposited

on r-plane sapphire showed strong NBE emission with fine structure including emission related to free-excitons, neutral-donor-bound-excitons, free-electron to bound-acceptors, defects, and also phonon replicas of emissions. A less intense neutral-donor-bound-exciton emission and the appearance of the free-electron to bound-acceptor peak at 3.3199 eV and its first- and second-order LO-phonon replicas were the biggest difference between the films on r-plane sapphire compared to those on c-plane sapphire.

7. Cross-sectional TEM images of films on r-plane sapphire showed vertically aligned dislocations and/or grain boundaries. This observation is consistent with the PL spectroscopy results of undoped ZnO films on r-plane sapphire where a free-electron to bound-acceptor emission was observed that was attributed to an electron in the conduction band that recombines with a hole that is bound to an acceptor state created by basal plane stacking faults.

8. The energy of the FX_A of undoped ZnO films on c-plane sapphire as a function of temperature was fit using the Manoogian-Woolley model. The 100 nm thick film was estimated to have a Debye temperature of 820 K and the 50 nm thick film was estimated to have a Debye temperature of 754 K. A lower Debye temperature is consistent with phonon softening at the surface, grain boundaries, disorder, defects, or impurities. It was noted that a wide range of values have been reported in the literature for ZnO, ranging from 305 K to 963 K. Some of this variation may result from the misuse of the Varshni equation, which is only applicable to materials with a low Debye temperature ($\Theta_D < 300$ K). Another potential source of the variation was identified as the exact method in which the data is fit; it was shown that different commercial software packages can lead to very different fitting parameters for the exact same data set.

9. Selected area electron diffraction patterns from doped films showed no evidence of a ReO_2 phase, but HR-TEM imaging clearly showed that the film with 20 wt. % ReO_2 on c-plane sapphire had alternating aligned columns of ZnO and ReO_2. The widths of the ZnO columns were larger than those of the ReO_2 columns. This columnar structure was not observed from films having concentrations of $ReO_2 < 20$ wt. %.

10. X-ray diffraction (XRD) patterns for the doped films on c-plane sapphire consisted of a (002)ZnO peak near 2Θ=34.5°, as well as a (006)Al_2O_3 peak near 2Θ=41.8° resulting from the substrate. For the specimen that had 50 wt. % ReO_2 in the film, there was also a weak (002)ReO_2 peak near 2Θ=31.9°. For the doped films on r-plane sapphire, the XRD patterns

consisted of a (110)ZnO peak near 2Θ=56.7° and a (024)Al_2O_3 peak near 2Θ=52.6°. The full width at half maximum (FWHM) of the (002)ZnO rocking curve indicated that for films on c-plane substrates, the addition of 5 wt. % ReO_2 improved the overall crystal quality. Further increase in the ReO_2 concentration led to a monotonic decrease in the crystal quality. For doped films on r-plane sapphire the FWHM of the (110)ZnO rocking curve indicated that the crystal quality improved with increasing ReO_2 concentration and reached a maximum at 10 wt. %. Further increase in ReO_2 concentration led to a decrease in crystal quality.

11. Results from the Hall effect measurements on the doped films indicate that for films on c-plane sapphire, the highest conductivity observed for the film with 5 wt. % ReO_2. For films on r-plane sapphire, the film with a ReO_2 concentration of 10 wt. % had the highest conductivity.

5.2 Potential Future Work

- It remains unclear where the Re atoms are incorporated into the films with lower ReO_2 concentrations. The use of high resolution Rutherford backscattering spectrometry (HR-RBS) may help to identify where the Re resides within the lattice.

- If HR-RBS proves successful at identifying where the Re resides, depth dependent measurements could also be performed to see if the location varies as a function of distance from the film/substrate interface.

- Directly measure the band gap of undoped ZnO films by UV-Vis spectroscopy to investigate the band gap as a function of residual stress.

- Investigate the use of other substrates with cubic structures, such as strontium tin oxide (STO) or MgO, for the growth of both undoped and doped films.

- Aging of bulk single crystal ZnO has previously been shown to result in changes to the PL response. Similar investigation of the the effects of aging on thin films would be of interest.

Bibliography

[1] S. Major, A. Banerjee, and K.L. Chopra. Highly transparent and conducting indium-doped zinc oxide films by spray pyrolysis. *Thin Solid Films*, 108:333–340, 1983.

[2] G.L. Bir and G.E. Pikus. *Symmetry and Strain Induced Effects in Semiconductors*. Wiley, 1974.

[3] Y. Sun, S.E. Thompson, and T.Nishida. *Strain Effect in Semiconductors Theory and Device Applications*. Springer, 2010.

[4] H.L. Cotal, J.B. Maxson, S.W.S. McKeever, and G. Cantwell. Uniaxial stress dependence of exciton emission from seeded physical vapor transport ZnSe. *Applied Physics Letters*, 64:1532–1534, 1994.

[5] R. Kumar, N. Khare, V. Kumar, and G.L. Bhalla. Effect of intrinsic stress on the optical properties of nanostructured ZnO thin films grown by rf magnetron sputtering. *Applied Surface Science*, 254:6509–6513, 2008.

[6] Y.F. Li, B. Yao, Y.M. Lu, Y.Q. Gai, C.X. Cong, Z.Z. Zhang, D.X. Zhao, J.Y. Zhang, B.H. Li, D.Z. Shen, X.W. Fan, and Z.K. Tang. Biaxial stress-dependent optical band gap, crystalline, and electronic structure in wurtzite ZnO: Experimental and ab initio study. *Journal of Applied Physics*, 104:083516, 2008.

[7] M. Ghosh and A.K. Raychaudhuri. Structural and optical properties of $Zn_{1-x}Mg_xO$ nanocrystals obtained by low temperature method. *Journal of Applied Physics*, 100:034315, 2006.

[8] S. Li-Bin, L. Ming-Biao, R. Jun-Yuan, W. Li-Jin, and Z. Cui-Yan. A study on strain affecting electronic structures and optical properties of wurtzite $Mg_{0.25}Zn_{0.75}O$ by first-principles. *Chinese Physics B*, 18:726–733, 2009.

[9] H.P. He, F. Zhuge, Z.Z. Ye, L.P. Zhu, F.Z. Wang, B.H. Zhao, and J.Y. Huang. Strain and its effect on optical properties of Al-N codoped ZnO films. *Journal of Applied Physics*, 99:023503, 2006.

[10] Y.F. Li, B. Yao, Y.M. Lu, C.X. Cong, Z.Z. Zhang, Y.Q. Gai, C.J. Zheng, B.H. Li, Z.P. Wei, D.Z. Shen, X.W. Fan, L. Xiao, S.C. Xu, and Y. Liu. Characterization of biaxial stress and its effect on optical properties of ZnO thin films. *Applied Physics Letters*, 91:021915, 2007.

[11] J.H. Lim, C.K. Kang, K.K. Kim, I.K. Park, D.K. Hwang, and S.J. Park. UV electroluminescence emission from ZnO light-emitting diodes grown by high-temperature radiofrequency sputtering. *Advanced Materials*, 18:2720–2724, 2006.

[12] Ya.I. Alivov, U. Ozgur, S. Dogan, C. Liu, Y. Moon, X. Gu, V. Avrutin, and H. Murkoc. Forward-current electroluminescence from GaN/ZnO double heterostructure diode. *Solid State Electronics*, 49:1693–1696, 2005.

[13] I.-S. Jeong, J.H. Kim, and S. Im. Ultraviolet-enhanced photodiode employing n-ZnO/p-Si structure. *Applied Physics Letters*, 83:2946–2948, 2003.

[14] C.R. Gorla, N.W. Emanetoglu, S. Liang, W.E. Mayo, Y. Lu, M. Wraback, and H. Shen. Structural, optical, and surface acoustic wave properties of epitaxial ZnO films grown on $(01\bar{1}2)$ sapphire by metalorganic chemical vapor deposition. *Journal of Applied Physics*, 85:2595–2601, 1999.

[15] H. Gong, J.Q. Hu, J.H. Wang, C.H. Ong, and F.R. Zhu. Nano-crystalline Cu-doped ZnO thin film gas sensor for CO. *Sensors and Actuators B*, 115:247–251, 2006.

[16] M. Krunks and E. Mellikov. Zinc oxide thin films by the spray pyrolysis method. *Thin Solid Films*, 270:33–36, 1995.

[17] U. Ozgur, Ya.I. Alivov, C. Liu, A. Teke, M.A. Reshchikov, S. Dogan, V. Avrutin, S.-J. Cho, and H. Morkoc. A comprehensive review of ZnO materials and devices. *Journal of Applied Physics*, 98:041301, 2005.

[18] L.J. Brillson and Y. Lu. ZnO Schottky barriers and ohmic contacts. *Journal of Applied Physics*, 109:121301, 2011.

[19] V.L. Solozhenko, O.O. Kurakevych, P.S. Sokolov, and A.N. Baranov. Kinetics of the wurtzite-to-rock-salt phase transformation in ZnO at high pressure. *Journal of Physical Chemistry A*, 115:4354–4358, 2011.

[20] A. Ashrafi and C. Jagadish. Review of zincblende ZnO: Stability of metastable ZnO phases. *Journal of Applied Physics*, 102:071101, 2007.

[21] S. Desgreniers. High-density phases of ZnO: Structural and compressive parameters. *Physical Review B*, 58:14102–14105, 1998.

[22] H. Ibach. Thermal expansion of silicon and zinc oxide (II). *Physica Status Solidi B*, 33:257–265, 1969.

[23] E.M. Kaidashev, M. Lorenz, H. von Wenckstern, A. Rahm, H.-C. Semmelhack, K.-H. Han, G. Benndorf, C. Bundesmann, H. Hochmuth, and M. Grundmann. High electron mobility of epitaxial ZnO thin films on c-plane sapphire grown by multistep pulsed-laser deposition. *Applied Physics Letters*, 82:3901–3903, 2003.

[24] K. Maeda, M. Sato, I. Niikura, and T. Fukuda. Growth of 2 inch ZnO bulk single crystal by the hydrothermal method. *Semiconductor Science and Technology*, 20:S49–S54, 2005.

[25] K. Iwata, P. Fons, S. Niki, A. Yamada, K. Matsubara, K. Nakahara, and H. Takasu. Improvement of electrical properties in ZnO thin films grown by radical source(RS)-MBE. *Physica Status Solidi A*, 180:287–292, 2000.

[26] R.H. Lamoreaux, D.L. Hildenbrand, and L. Brewer. High-temperature vaporization behavior of oxides ii. oxides of Be, Mg, Ca, Sr, Ba, B, Al, Ga, In, Tl, Si, Ge, Sn, Pb, Zn, Cd, and Hg. *Journal of Physical and Chemical Reference Data*, 16:419–443, 1987.

[27] C.F. Cline and D.R. Stephens. Volume compressibility of BeO and other II-VI compounds. *Journal of Applied Physics*, 36:2869, 1965.

[28] Y.S. Park, C.W. Litton, T.C. Collins, and D.C. Reynolds. Exciton spectrum of ZnO. *Physical Review*, 143:512–519, 1966.

[29] C.H. Bates, W.B. White, and R. Roy. The solubility of transition metal oxides in zinc oxide and the reflectance spectra of Mn^{2+} and Fe^{2+} in tetrahedral fields. *Journal of Inorganic and Nuclear Chemistry*, 28:397–405, 1966.

[30] K. Ueda, H. Tabata, and T. Kawai. Magnetic and electrical properties of transition-metal-doped ZnO films. *Applied Physics Letters*, 79:988, 2001.

[31] Z. Jin, T. Fukumura, M. Kawasaki, K. Ando, H. Saito, T. Sekiguchi, Y.Z. Yoo, M. Murakami, Y. Matsumoto, T. Hasegawa, and H. Koinuma. High throughput fabrication of transition-metal-doped epitaxial ZnO thin films: A series of oxide-diluted magnetic semiconductors and their properties. *Applied Physics Letters*, 78:3824–3826, 2001.

[32] W. Prellier, A. Fouchet, B. Mercey, C. Simon, and B. Raveau. Laser ablation of Co:ZnO films deposited from Zn and Co metal targets on (0001)Al_2O_3 substrates. *Applied Physics Letters*, 82:3490, 2003.

[33] J.H. Park, M.G. Kim, H.M. Jang, S. Ryu, and Y.M. Kim. Co-metal clustering as the origin of ferromagnetism in Co-doped ZnO thin films. *Applied Physics Letters*, 84:1338, 2004.

[34] H.-J. Lee, S.-Y. Jeong, C.R. Cho, and C.H. Park. Study of diluted magnetic semiconductor: Co-doped ZnO. *Applied Physics Letters*, 81:4020, 2002.

[35] M. Venkatesan, C.B. Fitzgerald, J.G.. Lunney, and J.M.D. Coey. Anisotropic ferromagnetism in substituted zinc oxide. *Physical Review Letters*, 93:177206, 2004.

[36] L. Zhang, F. Yan, G. Han, and P. Kang. A study on the degredation of methamidophos in the presence of nano-TiO_2 catalyst doped with Re. *Russian Journal of Inorganic Chemistry*, 54:1210–1216, 2009.

[37] K.-K. Kim, J.-H. Song, H.-J. Jung, W.-K. Choi, S.-J. Park, and J.-H. Song. The grain size effects on the photoluminescence of ZnO/α-Al_2O_3 grown by radio-frequency magnetron sputtering. *Journal of Applied Physics*, 87:3573–3575, 2000.

[38] Y. Chen, D.M. Bagnall, H.-J. Koh, K.-T. Park, K. Hiraga, Z.-Q. Zhu, and T. Yao. Plasma assisted molecular beam epitaxy of ZnO on c-plane sapphire: Growth and characterization. *Journal of Applied Physics*, 84:3912–3918, 1998.

[39] T. Yasuda and Y. Segawa. Zinc oxide thin films synthesized by metal organic chemical reactions. *Physica Status Solidi B*, 241:676–679, 2004.

[40] S. Choopun, R.D. Vispute, W. Noch, A. Balsamo, R.P. Sharma, T. Venkatesan, A. Iliadis, and D.C. Look. Oxygen pressure-tuned epitaxy and optoelectronic properties of laser-deposited ZnO films on sapphire. *Applied Physics Letters*, 75:3947–3949, 1999.

[41] J.F. Muth, R.M. Kolbas, A.K. Sharma, S. Oktyabrsky, and J. Narayan. Excitonic structure and absorption coefficient measurements of ZnO single crystal epitaxial films deposited by pulsed laser deposition. *Journal of Applied Physics*, 85:7884–7887, 1999.

[42] S.I. Park, T.S. Cho, S.J. Doh, J.L. Lee, and J.H. Je. Structural evolution of ZnO/sapphire(001) heteroepitaxy studied by real time synchrotron x-ray scattering. *Applied Physics Letters*, 77:349–351, 2000.

[43] C.H. Jia, Y.H. Chen, G.H. Liu, X.L. Liu, S.Y. Yang, and Z.G. Wang. Structural and optical properties of ZnO films on $SrTiO_3$ substrates by MOCVD. *Journal of Physics D: Applied Physics*, 42:015415, 2009.

[44] B.S. Kang, L. Stan, I.O. Usov, J.-K. Lee, T.A. Harriman, D.A. Lucca, R.F. DePaula, P.N. Arendt, M. Nastasi, J.L. MacManus-Driscoll, B.H. Park, and Q. Jia. Strain mismatch induced tilted heteroepitaxial (000l) hexagonal ZnO films on (001) cubic substrates. *Advanced Engineering Materials*, 13:1142–1145, 2011.

[45] M. Strikovskia and J.H. Miller Jr. Pulsed laser deposition of oxides: Why the optimum rate is about 1 Å per pulse. *Applied Physics Letters*, 73:1733–1735, 1998.

[46] T.A. Harriman. *Effects of lanthanoid ion implantation on the photoluminescence of silicon nanocrystals embedded in silicon nitride films.* M.S. Thesis, Oklahoma State University, 2008.

[47] K. Vanheusden, C.H. Seager, W.L. Warren, D.R. Tallant, and J.A. Voigt. Correlation between photoluminescence and oxygen vacancies in ZnO phosphors. *Applied Physics Letters*, 68:403–405, 1996.

[48] Q.X. Zhao, P. Klason, M. Willander, H.M. Zhong, W. Lu, and J.H. Yang. Deep-level emissions influenced by O and Zn implantations in ZnO. *Applied Physics Letters*, 87:211912, 2005.

[49] B. Lin, Z.X. Fu, and Y.B. Jia. Green luminescent center in undoped zinc oxide films deposited on silicon substrates. *Applied Physics Letters*, 79:943–945, 2001.

[50] N.O. Korsunska, L.V. Borkovska, B.M. Bulakh, L.Y. Khomenkova, V.I. Kushnirenko, and I.V. Markevich. The influence of defect drift in external electric field on green luminescence of ZnO single crystals. *Journal of Luminescence*, 102:733–736, 2003.

[51] A.B. Djurisic, W.C.H. Choy, V.A.L. Roy, Y.H. Leung, C.Y. Kwong, K.W. Cheah, T.K.G. Rao, W.K. Chan, H.T. Lui, and C. Surya. Photoluminescence and electron paramagnetic resonance of ZnO tetrapod structure. *Advanced Functional Materials*, 14:856–864, 2004.

[52] I. Shalish, H. Temkin, and V. Narayanamurti. Size-dependent surface luminescence in ZnO nanowires. *Physical Review B*, 69:245401, 2004.

[53] A. Mang, K. Reimann, and St. Rubenacke. Band gaps, crystal-field splitting, spin-orbit coupling, and exciton binding energies in ZnO under hydrostatic pressure. *Solid State Communications*, 94:251–254, 1995.

[54] D.G. Thomas. The exciton spectrum of zinc oxide. *Journal of Physics and Chemistry of Solids*, 15:86–96, 1960.

[55] J.L. Birman. Polarization of fluorescence in CdS and ZnS single crystals. *Physical Review Letters*, 2:157–159, 1959.

[56] H.B. Bebb and E.W. Williams. *Transport and Optical Phenomena, Volume 8 of Semiconductors and Semimetals*, chapter Photoluminescence I: Theory. Academic Press, 1972.

[57] A. Teke, U. Ozgur, S. Dogan, X. Gu, H. Morko, B. Nemeth, J. Nause, and H.O. Everitt. Excitonic fine structure and recombination dynamics in single-crystalline ZnO. *Physical Review B*, 70:195207, 2004.

[58] D.W. Hamby, D.A. Lucca, M.J. Klopfstein, and G. Cantwell. Temperature dependent exciton photoluminescence of bulk ZnO. *Journal of Applied Physics*, 93:3214–3217, 2003.

[59] K. Thonke, T. Gruber, N. Teofilov, R. Schonfelder, A. Waag, and R. Sauer. Donor acceptor pair transitions in ZnO substrate materials. *Physica B*, 308-310:945–948, 2001.

[60] D.C. Reynolds, D.C. Look, B. Jogai, C.W. Litton, T.C. Collins, W. Harsch, and G. Cantwell. Neutral-donor bound-exciton complexes in ZnO crystals. *Physical Review B*, 57:12151, 1998.

[61] B.J. Skromme. Photoluminescence, magnetospectroscopy, and resonant electronic Raman studies of heteroepitaxial gallium nitride ZnO. *MRS Internet Journal of Nitride Semiconductor Research*, 4:1–12, 1999.

[62] C.V. Raman and K.S. Krishnan. A new type of secondary radiation. *Nature*, 121:501, 1928.

[63] B.J. Bulkin. *Analytical* Raman *Spectroscopy*, chapter The Raman Effect: An Introduction. John Wiley and Sons, 1991.

[64] C. Kittel. *Introduction to Solid State Physics*. John Wiley and Sons, 8th edition, 2005.

[65] B.J. Kip and R.J. Meier. Determination of the local temperatures at a sample during Raman experiments using Stokes and anti-Stokes Raman bands. *Applied Spectroscopy*, 44:707–711, 1990.

[66] D.B. Chase. *Analytical* Raman *Spectroscopy*, chapter Modern Raman Instrumentation and Techniques. John Wiley and Sons, 1991.

[67] T.C. Damen, S.P.S. Porto, and B. Bell. Raman effect in ZnO. *Physical Review*, 142:570–574, 1966.

[68] F. Decremps, J. Pellicer-Porres, A.M. Saitta, J.-C. Chevrin, and A. Polian. High-pressure raman spectroscopy study of wurtzite ZnO. *Physical Review B*, 65:092101, 2002.

[69] M. Minsky. *US Patent #3,013,467: Microscopy Apparatus.* 1957.

[70] M.J. Matthews, A.L. Harris, A.J. Bruce, and M.J. Cardillo. Characterization of phosphosilicate thin films using confocal Raman microscopy. *Review of Scientific Instruments*, 71:2117–2120, 2000.

[71] N.J. Everall. Confocal Raman microscopy: Why the depth resolution and spatial accuracy can be much worse than you think. *Applied Spectroscopy*, 54:1515–1520, 2000.

[72] D.W. Hamby. *Effects of surface damage on the photoluminescence of* ZnO. Ph.D. Dissertation, Oklahoma State University, 2003.

[73] J.W. Beletic. *Optics in Astrophysics*, chapter Optical and Infrared Detectors for Astronomy. Springer-Verlag, 2005.

[74] T.A. Harriman, Z. Bi, Q.X. Jia, and D.A. Lucca. Frequency shifts of the E_2^{high} Raman mode due to residual stress in epitaxial ZnO thin films. *Applied Physics Letters*, 103:121904, 2013.

[75] R. Cebulla, R. Wendt, and K. Ellmer. Al-doped zinc oxide films deposited by simultaneous rf and dc excitation of a magnetron plasma: Relationships between plasma parameters and structural and electrical film properties. *Journal of Applied Physics*, 83:1087–1095, 1998.

[76] B.L. Zhu, X.H. Sun, S.S. Guo, X.Z. Zhao, J. Wu, R. Wu, and J. Liu. Effect of thickness on the structure and properties of ZnO thin films prepared by pulsed laser deposition. *Japanese Journal of Applied Physics*, 45:7860–7865, 2006.

[77] S.S. Mitra, O. Brafman, W.B. Daniels, and R.K. Crawford. Pressure-induced phonon frequency shifts measured by raman scattering. *Physical Review*, 186:942–944, 1969.

[78] S.K. Sharma and G.J. Exarhos. Raman spectroscopic investigation of ZnO and doped ZnO films, nanoparticles and bulk material at ambient and high pressures. *Solid State Phenomena*, 55:32–37, 1997.

[79] H.J. Trodahl, F. Martin, P. Muralt, and N. Setter. Raman spectroscopy of sputtered AlN films: E_2(high) biaxial strain dependence. *Applied Physics Letters*, 89:061905, 2006.

[80] J. Narayan, K. Dovidenko, A.K. Sharma, and S. Oktyabrsky. Defects and interfaces in epitaxial ZnO/α-Al_2O_3 and AlN/ZnO/α-Al_2O_3 heterostructures. *Journal of Applied Physics*, 84:2597–2601, 1998.

[81] T.B. Bateman. Elastic moduli of single-crystal zinc oxide. *Journal of Applied Physics*, 33:3309–3312, 1962.

[82] G. Carlotti, G. Socino, A. Petri, and E. Verona. Acoustic investigation of the elastic properties of ZnO films. *Applied Physics Letters*, 51:1889–1891, 1987.

[83] D.W. Hamby, D.A. Lucca, and M.J. Klopfstein. Photoluminescence of mechanically polished ZnO. *Journal of Applied Physics*, 97:043504, 2005.

[84] N. Ashkeno, B.N. Mbenkum, C. Bundesmann, V. Riede, M. Lorenz, D. Spemann, E.M. Kaidashev, A. Kasic, M. Schubert, M. Grundmann, G. Wagner, H. Neumann, V. Darakchieva, H. Arwin, and B. Monemar. Infrared dielectric functions and phonon modes of high-quality ZnO films. *Journal of Applied Physics*, 93:126–133, 2003.

[85] M.R. Wagner, G. Callsen, J.S. Reparaz, J.-H. Schulze, R. Kirste, M. Cobet, I.A. Ostapenko, S. Rodt, C. Nenstiel, M. Kaiser, A. Hoffmann, A.V. Rodina, M.R. Phillips, S. Lautenschlager, S. Eisermann, and B.K. Meyer. Bound excitons in ZnO: Structural defect complexes versus shallow impurity centers. *Physical Review B*, 83:035313, 2011.

[86] S. Guillemin, V. Consonni, B. Masenelli, and G. Bremond. Extended-defect-related photoluminescence line at 3.33 eV in nanostructured ZnO thin films. *Applied Physics Express*, 6:111101, 2013.

[87] D.S. Hildebrand. *Optical response of doped zinc oxide films.* M.S. Thesis, Oklahoma State University, 2012.

[88] A. Schildknecht, R. Sauer, and K. Thonke. Donor-related defect states in ZnO substrate material. *Physica B*, 340-342:205–209, 2009.

[89] S.F. Chichibu, T. Onuma, M. Kubota, A. Uedono, T. Sota, A. Tsukazaki, A. Ohtomo, and M. Kawasaki. Improvements in quantum efficiency of excitonic emissions in ZnO epilayers by the elimination of point defects. *Journal of Applied Physics*, 99:093505, 2006.

[90] K. Johnston, M.O. Henry, D. McCabe, E. McGlynn, M. Dietrich, E. Alves, and M. Xia. Identification of donor-related impurities in ZnO using photoluminescence and radiotracer techniques. *Physical Review B*, 73:165212, 2006.

[91] H. Kato, M. Sano, K. Miyamoto, and T. Yao. Homoepitaxial growth of high-quality Zn-polar ZnO films by plasma-assisted molecular beam epitaxy. *Japanese Journal of Applied Physics*, 42:L1002, 2003.

[92] V.Sh. Yalishev, Y.S. Kim, X.L. Deng, B.H. Park, and Sh.U. Yuldashev. Study of the photoluminescence emission line at 3.33 eV in ZnO films. *Physical Review B*, 83:035313, 2012.

[93] R. Ghosh, D. Basak, and S. Fujihara. Effect of substrate-induced strain on the structural, electrical, and optical properties of polycrystalline ZnO thin films. *Journal of Applied Physics*, 96:2689–2692, 2004.

[94] T. Prasada Rao, M.C. Santhosh Kumar, S. Anbumozhi Angayarkanni, and M. Ashok. Effect of stress on optical band gap of ZnO thin films with substrate temperature by spray pyrolysis. *Journal of Alloys and Compounds*, 485:413–417, 2009.

[95] S. Li, Q. Jiang, and G.W. Yang. Uniaxial strain modulated band gap of ZnO nanostructures. *Applied Physics Letters*, 96:213101, 2010.

[96] Y. Hwang and Y. Um. Optical properties of non-polar a-plane ZnO single crystal. *Journal of the Korean Physical Society*, 67:763–766, 2015.

[97] X. Han, Y. Gao, J. Dai, C. Yu, Z. Wu, C. Chen, and G. Fang. Nonpolar a-plane ZnO films grown on gan/sapphire templates with SiN_x interlayer by pulsed laser deposition. *Journal of Physics D: Applied Physics*, 43:1079–1081, 2010.

[98] T. Koida, S.F. Chichibu, A. Uedono, T. Soto, A. Tsukazaki, and M. Kawasaki. Radiative and nonradiative excitonic transitions in nonpolar $(11\bar{2}0)$ and polar $(000\bar{1})$ and (0001) ZnO epilayers. *Applied Physics Letters*, 84:1079–1081, 2004.

[99] Y.S. Nam, S.W. Lee, K.S. Baek, S.K. Chang, J.-H. Song, J.-H. Song, S.K. Han, S.-K. Hong, and T. Yao. Anisotropic optical properties of free and bound excitons in highly strained a-plane ZnO investigated with polarized photoreflectance and photoluminescence spectroscopy. *Applied Physics Letters*, 92:201907, 2008.

[100] M. Schirra, R. Schneider, A. Reiser, G.M. Prinz, M. Feneberg, J. Biskupek, U. Kaiser, C.E. Krill, K. Thonke, and R. Sauer. Stacking fault related 3.31eV luminescence at 130meV acceptors in zinc oxide. *Physical Review B*, 77:125215, 2008.

[101] A. Manoogian and J.C. Woolley. Temperature dependence of the energy gap in semiconductors. *Canadian Journal of Physics*, 62:285–287, 1984.

[102] A.R. Hutson. Electronic properties of ZnO. *Journal of Physics and Chemistry of Solids*, 8:467–472, 1959.

[103] W. Ma, X. Zhang, and K. Takahashi. Electrical properties and reduced Debye temperature of polycrystalline thin gold films. *Journal of Physics D: Applied Physics*, 43:465301, 2010.

[104] A. Bid, A. Bora, and A.K. Raychaudhuri. Temperature dependence of the resistance of metallic nanowires of diameter $\geq$ 15 nm: Applicability of Bloch-Gruneisen theorem. *Physical Review B*, 74:035426, 2006.

[105] G. De Marzi, D. Iacopino, A.J. Quinn, and G. Redmond. Probing intrinsic transport properties of single metal nanowires: Direct-write contact formation using a focused ion beam. *Journal of Applied Physics*, 96:3458–3462, 2004.

[106] E. Przezdziecka, L. Wachnicki, W. Paszkowicz, E. Lusakowska, T. Krajewski, G. Luka, E. Guziewicz, and M. Godlewski. Photoluminescence, electrical and structural properties of ZnO films, grown by ALD at low temperature. *Semiconductor Science and Technology*, 24:105014, 2009.

[107] L. Troger, T. Yokoyama, D. Arvanitis, T. Lederer, M. Tischer, and K. Baberschke. Determination of bond lengths, atomic mean-square relative displacements, and local thermal expansion by means of soft-x-ray photoabsorption. *Physical Review B*, 49:888–904, 1994.

[108] L. Wang and N.C. Giles. Temperature dependence of the free-exciton transition energy in zinc oxide by photoluminescence excitation spectroscopy. *Journal of Applied Physics*, 94:973–978, 2003.

[109] K. Sakai, K. Noguchi, A. Fukuyama, T. Ikari, and T. Okada. Low-temperature photoluminescence of nanostructured ZnO crystal synthesized by pulsed-laser ablation. *Japanese Journal of Applied Physics*, 48:085001, 2009.

[110] H.-W. Suh, G.-Y. Kim, Y.-S. Jung, W.-K. Choi, and D. Byun. Growth and properties of ZnO nanoblades and nanoflowers prepared by ultrasonic pyrolysis. *Journal of Applied Physics*, 97:044305, 2005.

[111] C.J. Youn, T.S. Jeong, M.S. Han, and J.H. Kim. Optical properties of Zn-terminated ZnO bulk. *Journal of Crystal Growth*, 261:526–532, 2004.

[112] R.A. Robie and J.L. Edwards. Some debye temperatures from single-crystal elastic constant data. *Journal of Applied Physics*, 37:2659–2663, 1966.

[113] A. Zubiaga, J.A.Garcia, F. Plazaola, F. Tuomisto, K. Saarinen, J. Zuniga Perez, and V. Munoz-Sanjose. Correlation between Zn vacancies and photoluminescence emission in ZnO films. *Journal of Applied Physics*, 99:053516, 2006.

[114] S.C. Abrahams and J.L. Bernstein. Remeasurement of the structure of hexagonal ZnO. *Acta Crystallographica*, B25:1233–1236, 1969.

[115] H.J. Yearian. Intensity of diffraction of electrons by ZnO. *Physical Review*, 48:631–640, 1935.

[116] C.H. Ehrhardt and K. Lark-Horovitz. Intensity distribution in x-ray and electron diffraction patterns. x-ray atom factors of zinc in zinc oxide and chemical binding. *Physical Review*, 57:603–613, 1940.

[117] C. Boemare, T. Monteiro, M.J. Soares, J.G. Guilherme, and E. Alves. Photoluminescence studies in ZnO samples. *Physica B*, 308-310:985–988, 2001.

[118] Y.P. Varshni. Temperature dependence of the energy gap in semiconductors. *Physica*, 34:149–154, 1967.

[119] Q.X. Jia. Los Alamos National Laboratory. Personal Communication, October 2014.

[120] R.D. Shannon. Revised effective ionic radii and systematic studies of interatomic distances in halides and chalcogenides. *Acta Crystallographica Section A*, 78:751–767, 1976.

[121] J.D. Albrecht, P.P. Ruden, S. Limpijumnong, W.R.L. Lambrecht, and K.F. Brennan. High field electron transport properties of bulk ZnO. *Journal of Applied Physics*, 86:6864, 1991.

[122] D.C. Look, D.C. Reynolds, J.R. Sizelove, R.L. Jones, C.W. Litton, G. Cantwell, and W.C. Harsch. Electrical properties of bulk ZnO. *Solid State Communications*, 105:399–401, 1998.

[123] U. Ozgur, V. Avrutin, and H. Morkoc. *Molecular Beam Epitaxy: From Research to Mass Production*, chapter Zinc oxide materials and devices grown by MBE. Elsevier, 2012.

VITA

Tres Harriman

Candidate for the Degree of

Doctor of Philosophy

Thesis: OPTICAL RESPONSE OF UNDOPED AND DOPED ZINC OXIDE THIN FILMS

Major Field: Mechanical and Aerospace Engineering

Biographical:

Personal Data: Born in Elkhart, KS, USA on February 24, 1981, the son of Carman and Jan Harriman.

Education:

Graduated from David H. Hickman High School, Columbia, Missouri in June 1999. Received the Bachelor of Science degree in Mechanical Engineering from the University of Missouri, Columbia, Missouri in December 2003. Received the Master of Science in Mechanical Engineering at Oklahoma State University, Stillwater, Oklahoma in July 2008. Completed the requirements for the Doctor of Philosophy in Mechanical and Aerospace Engineering at Oklahoma State University, Stillwater, Oklahoma in July 2017.

Experience:

Student supervisor, University Bookstore, 1999 to 2004; Substitute teacher, Columbia Public Schools, 2004 to 2005; Graduate research/teaching assistant, Oklahoma State University, 2005 to present.

Professional Memberships:

Order of the Engineer.